THEORETICAL INVESTIGATION OF STRUCTURAL, VIBRATIONAL, ELECTRONIC, AND ELASTIC PROPERTIES OF ULTRA-THIN ANISOTROPIC MATERIALS

A Thesis Submitted to
the Graduate School of
İzmir Institute of Technology
in Partial Fulfillment of the Requirements for the Degree of

MASTER OF SCIENCE

in Physics

by
Kadir Can DOĞAN

July 2024
İZMİR

We approve the thesis of **Kadir Can DOĞAN**

Examining Committee Members:

Assoc. Prof. Mehmet YAĞMURCUKARDEŞ
Photonics Science and Engineering, İzmir Institute of Technology

---

Assoc. Prof. Serkan ATEŞ
Department of Physics, İzmir Institute of Technology

Prof. Dr. Hasan ŞAHİN
Photonics Science and Engineering, İzmir Institute of Technology

---

Assoc. Prof. Fatih ERSAN
Department of Physics, Adnan Menderes University

Assoc. Prof. Ümit AKINCI
Department of Physics, Dokuz Eylül University

02 July 2024

Assoc. Prof. Mehmet YAĞMURCUKARDEŞ
Supervisor, Photonics Science and Engineering
İzmir Institute of Technology

Assoc. Prof. Serkan ATEŞ
Co-supervisor, Department of Physics
İzmir Institute of Technology

Prof. Dr. Lütfi ÖZYÜZER
Head of the Department of
Physics

Prof. Dr. Mehtap EANES
Dean of the Graduate School

ACKNOWLEDGMENTS

First and foremost, I would like to express my deepest gratitude and utmost respect to Assoc. Prof. Mehmet YAĞMURCUKARDEŞ, who served as both an exceptional supervisor and a supportive mentor throughout research journey. His guidance and unwavering encouragement have been invaluable to me. Additionally, I extend my heartfelt appreciation to my co-advisor, Assoc. Prof. Serkan ATEŞ, for his insightful perspectives and invaluable advice, which have greatly enriched my research experience. It was truly an honor and a privilege to be supervised by them. Moreover, I am grateful to Prof. Dr. Hasan ŞAHİN for his transformative insights, which have significantly contributed to my development and research progress. His thoughtful reviews and guidance have truly shaped my perspective.

I owe a great deal of gratitude to the MYK and ŞAHİN research groups for their invaluable support and contributions to my academic endeavors, with special thanks to our Postdoctoral researcher, Zebih ÇETİN. Their guidance, assistance, and patience have been instrumental in making the completion of my thesis possible. I am deeply grateful to my parents, Nejla and Çetin DOĞAN, for instilling in me the values of hard work and morality. Their unwavering support and guidance have been essential throughout my journey. Foremost among my expressions of gratitude is reserved for Dilek TEPELİ whose unwavering support and encouragement have been invaluable to me throughout my academic journey. Her presence has been a constant source of comfort and inspiration.

This thesis is dedicated to all the professors and the scientists that touched my life and enlightened me.

ABSTRACT

THEORETICAL INVESTIGATION OF STRUCTURAL, VIBRATIONAL, ELECTRONIC, AND ELASTIC PROPERTIES OF ULTRA-THIN ANISOTROPIC MATERIALS

Dimensional reduction in materials leads to significant improvements and changes in various properties due to quantum phenomena and intense confinement of electrons. Since the separation of graphene from bulk graphite in 2004, many different materials with layered bulk structures have been experimentally introduced into the literature, including hexagonal boron nitride (BN), transition metal dichalcogenides (TMDs), and in-plane anisotropic monolayer black phosphorus (BP). Among ultra-thin materials, anisotropic materials have attracted attention due to their distinct orientation-dependent vibrational, electronic, optical, and mechanical features and have been shown to have high potential for special applications such as polarization-sensitive photodetectors, orientation-dependent optoelectronic devices, and orientation-sensitive sensors. The aim of this thesis is to predict the stable structures of ultra-thin anisotropic materials such as $HfTe_5$, TiX_5, TaX_3 (X:S, Se, Te), bismuthene and magnetic $MnPS_3$ nanoribbons and to understand their structural, magnetic, vibrational, electronic, optical and elastic properties on a physical basis by performing density functional theory (DFT)-based first-principles calculations. Preliminary data via STM images are presented for the potential experimental characterization of possible defects and oxidized structures of the single-layer $HfTe_5$, whose predicted stable structure. The existence of stable structures of titanium-based penta-calcogenides is predicted and the direction-dependent properties of the stable phases are investigated. The dynamic stability of Ta-based trichalcogens exhibiting anisotropy different from TiS_3 and ZrS_3 has been investigated and their crystal-orientation dependent elastic properties are analysed. In addition, in the tilted α-bismuth known as the α phase, the identification of the external strain direction through the Raman spectrum is examined. The reduction of in-plane anisotropy to 1 dimension is studied through the edge type- and width- dependent properties in magnetic $MnPS_3$ nanoribbons. Our findings are important for the prediction of novel anisotropic materials.

ÖZET

ULTRA-İNCE ANİZOTROPİK MALZEMELERİN YAPISAL, TİTREŞİMSEL, ELEKTRONİK VE ELASTİK ÖZELLİKLERİNİN TEORİK İNCELENMESİ

Malzemelerde boyutsal azalma, kuantum fenomenleri ve elektronların yoğun sıkışması nedeniyle çeşitli özelliklerde önemli iyileştirmelere ve değişikliklere yol açar. 2004 yılında grafenin yığın durumdaki grafitten ayrıştırılmasından bu yana, altıgen bor nitrür (BN), geçiş metali dikalkojenitleri (TMD'ler) ve düzlem içi anizotropik tek katmanlı siyah fosfor (BP) dahil olmak üzere katmanlı yığın yapısına sahip bir çok farklı malzeme deneysel olarak literatüre kazandırılmıştır. Ultra ince malzemeler arasında anizotropik malzemeler, farklı yönelimlere bağlı titreşimsel, elektronik, optik ve mekanik özellikleri nedeniyle ilgi çekmiş ve polarizasyona duyarlı fotodedektörler, yöne bağlı optoelektronik cihazlar ve yönelime duyarlı sensörler gibi özel uygulamalar için yüksek potansiyele sahip oldukları gösterilmiştir. Bu tezin amacı, yoğunluk fonksiyonel teorisi (YFT) tabanlı ilk prensip hesaplamaları yaparak $HfTe_5$, TiX_5, TaX_3 (X:S, Se, Te), bizmuten ve manyetik $MnPS_3$ nanoşeritler gibi ultra-ince anizotropik malzemelerin kararlı yapılarını öngörmek ve yapısal, manyetik, titreşimsel, elektronik, optik ve elastik özelliklerini fiziksel temelde anlamaktır. Kararlı yapısı öngörülen tek katmanlı $HfTe_5$'in olası kusurlarının ve bu kusurların oksitli yapılarının olası deneysel karakterizasyonu için STM görüntüleri üzerinden ön veriler sunulmuştur. Titanyum bazlı pentakalkojenitlerin kararlı yapılarının varlığı öngörülmüş ve kararlı fazların yön bağımlı özellikleri incelenmiştir. TiS_3 ve ZrS_3 malzemelerinden farklı yapıda anizotropi sergileyen Ta-bazlı trikalkojenlerin dinamik kararlılıkları incelenmiş ve kristal yönelimine bağımlı elastik özellikleri irdelenmiştir. Bunun yanında, bizmutenin α-fazı olarak bilinen eğimli yapısında, dış gerinim yönünün Raman spektrumu üzerinden anlaşılması çalışılmıştır. Düzlem içi anizotropinin 1 boyuta indirgenmesi, manyetik $MnPS_3$ nanoşeritlerinin kenar tipi ve şerit genişliğine bağımlı özellikleri üzerinden incelenmiştir. Bulgularımız, yeni anizotropik malzemelerin öngörülmesi açısından önem arz etmektedir.

TABLE OF CONTENTS

LIST OF FIGURES viii

LIST OF TABLES xiii

CHAPTER 1. INTRODUCTION 1

CHAPTER 2. THEORETICAL BACKGROUND AND COMPUTATIONAL METHODOLOGY 1

2.1. The Many Body Problem 1

2.1.1. Born-Oppenheimer Approximation 2

2.1.2. Thomas-Fermi Model 4

2.1.3. Density Functional Theory 6

2.1.4. Hohenberg-Khon Theorems 7

2.1.5. Kohn-Sham Equations 8

2.1.6. Exchange-Correlation Functionals 11

2.1.7. Heyd-Scuseria-Ernzerhof (HSE) Functional 13

2.1.8. Hellman-Feynman Theorem 14

2.2. Theory of Phonons 15

2.3. Raman Spectroscopy 18

2.4. Mechanical Properties of Materials 24

2.4.1. Elastic Constants 25

2.4.1.1. Young Modulus 26

2.4.1.2. Poisson Ratio 27

2.4.2. Elastic Constants in 2D Limit 28

2.4.2.1. In-plane Stiffness 28

2.5. Computational Parameters 32

CHAPTER 3. NOVEL HIGHLY ANISOTROPIC SINGLE-LAYER TRANSITION METAL PENTACHALCOGENIDES 34

3.1. Hafnium Pentatelluride 34

3.2. Titanium Pentachalcogenides 49

CHAPTER 4. NOVEL HIGHLY ANISOTROPIC SINGLE-LAYER TANTALUM TRICHALCOGENIDES 54
4.1. Structural and Vibrational Properties 54
4.2. Electronic and Optical Properties 57
4.3. Elastic Properties 59

CHAPTER 5. ANISOTROPIC SINGLE-LAYER TILTED α-BISMUTHENE 62
5.1. Structural and Vibrational Properties 62
5.2. Electronic Properties 66
5.3. Elastic Properties 67
5.4. Strain Characterization via Vibrational Spectrum 69

CHAPTER 6. EDGE- AND WIDTH-DEPENDENT ANISOTROPY IN ULTRA-NARROW 1D MAGNETIC MANGANESE PHOSPHORUS TRI-SULFIDE ($MNPS_3$) NANORIBBONS 73
6.1. 2D Single-layer of $MnPS_3$ 73
6.2. Single-layer 1D Nanoribbons of $MnPS_3$ 77
6.2.1. Mn-Edged ANRs of $MnPS_3$ 78
6.2.2. P-Edged Armchair Nanoribbons of $MnPS_3$ 82
6.2.3. Mn-P Edged Armchair Nanoribbons of $MnPS_3$ 84
6.2.4. Zigzag Nanoribbons of $MnPS_3$ 87

CHAPTER 7. CONCLUSION 91

REFERENCES 95

LIST OF FIGURES

Figure		Page
Figure 2.1	The figure illustrating the fundamental concept of the local density approximation and Thomas-Fermi theory depicts a radial slab, dr, where the local charge density n(r) corresponds to the density of a uniform homogeneous electron gas.	4
Figure 2.2	DFT approach to a many-body system.	6
Figure 2.3	Depiction of the first Hohenberg-Kohn theorem.	7
Figure 2.4	Illustration of the real system of electrons that interact with each other and the Kohn-Sham fictitious system of non-interacting electrons with each other.	9
Figure 2.5	Representation of the local density approximation involves substituting the precise exchange-correlation energy density at each point r with that of a uniform, homogeneous electron gas having a density equivalent to n(r).	12
Figure 2.6	Illustration of three types of scattering process that can occur when light interacts with a material, and the energy level diagram shows the origin of Rayleigh, Stokes, and Anti-Stokes Raman scatter. The energy level diagram depicts the states involved in Raman spectroscopy.	19
Figure 2.7	Induced dipole illustration under the influence of an electric field.	20
Figure 2.8	An illustrative configuration for the Raman scattering process. The symbols $\hat{e}_i$ and $\hat{e}_s$ denote the polarization vectors of the incident and the scattered light, respectively.	23
Figure 3.1	For the single-layer $HfTe_5$ structures, (a) top and side views of the structure. (b) The phonon band dispersions (left panel) with the corresponding Raman spectrum (right panel) and (c) atomic vibrations of each Raman-active phonon mode.	35
Figure 3.2	(a) Local potential profile of $HfTe_5$ plane averaged along the out-of-plane direction and (b) work functions of Hf-based single-layer structures. The Fermi energy (E_F) and the work function (Φ) are ilustrated as insets in (a).	36

Figure **Page**

Figure 3.3 For the Quantum Molecular Dynamics simulations of $HfTe_5$ (a) total energy fluctuations, (b) final structure at 300K, and (c) variation in bond lengths of $d_{Hf-Te_{ch}}$, $d_{Hf-Te_{out}}$, $d_{Te_{out}-Te_{out}}$, and $d_{Te_{ch}-Te_{in}}$ as a function of the temperature. 37

Figure 3.4 Cleavage energy of single-layer $HfTe_5$ crystal structure as a function of seperation distance. 38

Figure 3.5 (a) The calculated electronic band dispersions of $HfTe_5$ with (b) corresponding partial density of states. (c) The atomic orbital contributions to charge densities of the VBM and the CBM states. (d) Effective masses of electrons and holes in single-layer $HfTe_5$ for different orientation angles. 39

Figure 3.6 For single-layer $HfTe_5$ structure, calculated in- and out-of-plane (a) component of the imaginary parts of the dielectric function, (b) absorption, (c) reflectance, and (d) transmittance spectra, as a function of photon energy. 41

Figure 3.7 (a) Schematic representation of the orientation angle (θ). (b) The angle-dependent in-plane stiffness (C) and (c) that of Poisson ratio (υ). a and c in $HfTe_5$ structures represent the directions perpendicular and parallel to the Hf chains, respectively. 44

Figure 3.8 (a) Top views and simulated STM images of defected $HfTe_5$ and (b) those for the oxidized defect structures. The dashed red circles indicate the vacant atom in the structure and the blue dashed circles stand for the O atoms. Turquoise lines represent the line profile of STM images of defected and oxidized defected structures. 46

Figure 3.9 For the single-layer ultra-thin TiX_5 (X=S, Se, and Te) structures, (a) top views of the crystal structures, (b) simulated STM images, and (c) side views of the lattice structures. 50

Figure 3.10 Phonon band dispersions of single-layers (a) TiS_5, (b) $TiSe_5$, and (c) $TiTe_5$, respectively. 51

Figure 3.11 (a) The calculated electronic band dispersions (SOC) of single-layer TiX_5 structures. The Fermi energy (E_F) level is set to the top of valence states and (b) corresponding partial density of states of single-layer TiX_5 crystals. 52

Figure		**Page**

Figure 3.12 (a) Schematic representation of the orientation angle (θ). (b) The angle-dependent in-plane stiffness (C) and (c) that of Poisson ratio (υ). a and b in TiX_5 structures represent the directions perpendicular and parallel to the Ti chains, respectively. 53

Figure 4.1 For single-layer TaX_3 structures (a) top and (b) side view of the optimized atomic structures. (c) Simulated STM images of TaS_3, $TaSe_3$ and $TaTe_3$ crystals. 55

Figure 4.2 The phonon band dispersions of single-layer TaS_3, $TaSe_3$ and $TaTe_3$ crystals. 56

Figure 4.3 (a) The calculated electronic band structures of TaS_3, $TaSe_3$ and $TaTe_3$ single-layers with (b) corresponding partial density of states. 58

Figure 4.4 Calculated in- and out-of-plane component of the imaginary parts of the dielectric function, absorption, reflectance, and transmittance spectra as a function of photon energy for single-layers (a) TaS_3 (b) $TaSe_3$ and (c) $TaTe_3$ crystal structure. 59

Figure 4.5 (a) Schematic representation of the orientation angle (θ). (b) The angle-dependent in-plane stiffness (C) and (c) that of Poisson ratio (υ) of TaX_3 layers. 60

Figure 5.1 For the single-layer α-Bi structure, (a) top and side views of the crystal structure, and (b) simulated STM image. Corresponding electron localization function contour map for the plane containing directly connected top Bi atoms is shown in (a). 63

Figure 5.2 (a) The phonon band dispersions, (b) Raman activity of zone-centered vibrations, and the corresponding (c) atomic vibrations of Raman active phonon modes in single-layer α-Bi. 64

Figure 5.3 For the QMD simulations of α-Bi structure, (a) total energy fluctuations, (b) the crystal structure at 300K, and (c) variation in bond lengths of d^{out}_{A-B} and d^{in}_{A-B} as a function of total simulation time at room temperature. 65

Figure **Page**

Figure 5.4 (a) The calculated electronic band dispersions (GGA and HSE06) of single-layer α-Bi structure. The Fermi energy (E_F) level is set to the top of valence states. The blue dashed line and red solid lines represent the band structures calculated within HSE06 and GGA, respectively. (b) Corresponding partial density of state of α-Bi and (c) atomic orbitals contributing to the VBM and CBM states. Isosurface value for the atomic orbitals in (c) is taken to be $2.5x10^{-5}e^{-}/^{3}$. (d) Effective masses of electrons and holes for different orientation angles. 66

Figure 5.5 (a) Schematic representation of the orientation angle θ, (b) the angle-dependent in-plane stiffness (C) and (c) that of Poisson ratio (υ). 69

Figure 5.6 The phonon band dispersions under $\pm5\%$ strains along the (a) ZZ and (b) AC directions. 70

Figure 5.7 Raman spectra of single-layer α-Bi under the effect of (a) ZZ and (b) AC strains. 71

Figure 6.1 Spin arrangements of (a) FM, (b) Néel, (c) zigzag, and (d) stripy AFM. The yellow, and blue colors represent the spin-up and spin-down state Mn atoms, respectively. 74

Figure 6.2 (a) The phonon band dispersions, and (b) electronic band structure and partial density of states (PDOS) of single-layer $MnPS_3$. 76

Figure 6.3 Structural illustrations of $MnPS_3$ nanoribbons (a) Mn-Mn, Mn-P, and P-P edged armchair nanoribbons, (b) Mn-P line zigzag nanoribbons. Numbers show the maximum width of the corresponding nanoribbons for this study. 77

Figure 6.4 (a) Structural illustrations of Mn-Mn edged armchair nanoribbons with varying widths of two, three, four, five, and six layer, and (b) corresponding simulated STM images of Mn-Mn edged armchair nanoribbons. 78

Figure 6.5 For Mn-edged armchair nanoribbons with varying widths, (a) lattice parameters, (b) total magnetizations, (c) cohesive energies, and (d) work functions. 79

Figure 6.6 The calculated electronic band structures of Mn-edged armchair nanoribbons with varying widths of two, three, four, five, six, and seven layer. . 80

Figure		Page
Figure 6.7	(a) Structural depictions of P-P edged armchair nanoribbons with varying widths of P-2, P-3, P-4, and P-5, and (b) corresponding simulated STM images of P-P edged armchair nanoribbons.	81
Figure 6.8	(a) The lattice parameters, (b) cohesive energies, (c) work functions and (d) band gap variations of P-edged armchair nanoribbons with different widths.	82
Figure 6.9	Electronic band structures of P-2, P-3, P-4, P-5, P-6 and P-7 armchair nanoribbons.	83
Figure 6.10	(a) Structural illustration of Mn-P edged ANRs with different widths of 1-1, 2-1, 3-2, 4-2, 5-3, and 6-3. The labels indicate the number of Mn, and P layers, respectively in each configuration. (b) Corresponding simulated STM images of Mn-P terminated armchair nanoribbons.	84
Figure 6.11	(a) The calculated lattice parameters, (b) total magnetizations, (c) cohesive energies, and (d) work functions of Mn-P edged armchair nanoribbons with different widths.	85
Figure 6.12	The calculated electronic band structure of Mn-P terminated armchair nanoribbons with varying widths of 1-1, 2-1, 3-2, 4-2, 5-3, 6-3, 7-4, and 8-4. The chart below the band structures present the relationship between the width of the ribbon and the variation in band gap values for Mn-P edged ANRs.	86
Figure 6.13	(a) Optimized structures of ZZ nanoribbons with varying widths of 1, 2, 3, 4, 5, and 6. The labels indicate the number of layer, and (b) corresponding simulated STM images of ZNRs.	88
Figure 6.14	For the zigzag nanoribbons, (a) total energy difference between AFM and FM magnetic ground states, (b) the calculated lattice parameters, (c) total magnetizations, (d) cohesive energies, (e) work functions, and (f) band gap variations.	89
Figure 6.15	The calculated electronic band structures of zigzag nanoribbons with different widths ranging from 1 to 6.	90

LIST OF TABLES

Table **Page**

Table 3.1 For the single-layer $HfTe_5$; the optimized in-plane lattice parameters, *a and c*; the atomic bond lengths between individual atoms, $d_{Hf-Te_{ch}}$, $d_{Hf-Te_{out}}$, $d_{Te_{out}-Te_{out}}$, $d_{Te_{ch}-Te_{in}}$; vertical distance between uppermost and lowermost Te atoms (thickness), t; the cohesive energy per atom, E_{coh}; the work function, Φ; and electronic band gap energy E_g^{SOC}. 34

Table 3.2 For the single-layer $HfTe_5$; deformation energy, E_1; the effective mass m^*; elastic moduli, C_{2D}; and the carrier mobilities, μ. 40

Table 3.3 For single-layer $HfTe_5$, the relaxed ion elastic coefficients C_{ij}; the corresponding in-plane stiffness C, and Poisson ratio υ, along $Hf_{ch}^{\parallel}$ and $Hf_{ch}^{\perp}$ directions. 43

Table 3.4 For various defects in $HfTe_5$, the type of the defect; the expansion rate of the lattice parameters ($-$ and $+$ stand for compression and expansion, respectively), a and c; the defect formation energy E_{for}; and the net magnetic moment of the defect domain, μ. For comparability, formation energies of Te-Hf vacancies are given in eV/(Te-Hf). 45

Table 3.5 For the oxygen substituted in defected single-layer $HfTe_5$, we present the different types of oxidation; the expansion rate of the lattice parameter (- and + stand for compression and expansion, respectively), a and c; the defect formation energy E_{for}; the net magnetic moment of the defect domain, μ; the electronic ground state; and the energy band gap of defected structure. For comparability, binding energy for oxygen atom adsorbed on the Te-Hf vacancies are given in eV/Te-Hf. 47

Table 3.6 For the single-layer TiX_5; the optimized in-plane lattice parameters, *a and c*; the atomic bond lengths between individual atoms, $d_{Ti-X_{ch}}$, $d_{Ti-X_{out}}$, $d_{X_{out}-X_{out}}$; vertical distance between uppermost and lowermost Te atoms (thickness), t; the cohesive energy per atom, E_{coh}; the work function, Φ; and electronic band gap energy E_g^{SOC}. 49

Table 3.7 For single-layer TiX_5, the relaxed ion elastic coefficients C_{ij}; the corresponding in-plane stiffness C, and Poisson ratio υ, along $Ti_{ch}^{\parallel}$ and $Ti_{ch}^{\perp}$ directions. 53

Table **Page**

Table 4.1 For the single-layer 2D TaX_3: the optimized in-plane lattice parameters (*a and b*), vertical distance between uppermost and lowermost S atoms (t), the cohesive energy per atom (E_{coh}), and the work function, (Φ). 54

Table 4.2 For single-layer TaS_3, $TaSe_3$ and $TaTe_3$ structures, the relaxed ion elastic coefficients C_{ij} the corresponding in-plane stiffness C, and Poisson ratio υ, along a and b direction. 60

Table 5.1 For the optimized free-standing structure of single-layer α-Bi; the in-plane lattice parameters (*a* and *b*), tilting between Bi_A and Bi_B atoms (Δh); the atomic bond lengths between A and B type Bi atoms, d^{in}_{A-B}, d^{out}_{A-B}; vertical distance between uppermost and lowermost Bi, t; the cohesive energy per atom, E_{coh}; the work function, Φ; and electronic band gap calculated within HSE06 (E_g^{HSE06}). 62

Table 5.2 The relaxed-ion elastic coefficients, C_{ij}; and the corresponding in-plane stiffness, C; and Poisson ratio, υ; along ZZ and AC directions in single-layer α-Bi. 68

Table 6.1 For the single-layer 2D and bulk $MnPS_3$: the optimized in-plane lattice parameters (*a and b*), the atomic bond lengths between individual atoms (d_{Mn-S}, d_{P-S}), vertical distance between uppermost and lowermost S atoms (t), the amount of donated electron for manganese (ρ_{Mn}), and phosphor (ρ_P), the amount of received electron for sulfur (ρ_S), the cohesive energy per atom (E_{coh}), electronic band gap energy (E_g), and the work function, (ϕ). 75

CHAPTER 1

INTRODUCTION

The identification of novel materials, or novel characteristics of existing materials, to fulfill particular industrial or scientific needs, is a stimulating intellectual endeavor of paramount significance for our technology, environment, economy, and future. After establishing the importance of identifying novel materials, particularly in the context of industrial and scientific needs, a significant advancement has been witnessed with the emergence of low-dimensional systems. These systems, which include zero-dimensional quantum dots, one-dimensional nanoribbons, nanotubes, and nanowires, as well as two-dimensional single-atom-thick materials,[1] represent a frontier in material science. Understanding the dimensionality of these structures is crucial as it dictates their atomic arrangement and distinctive properties.[2] Remarkably, the same material can exhibit vastly different characteristics when manipulated into different dimensions, as illustrated by the striking differences between graphene and bulk graphite. The atomically thin structures hold immense promise for both scientific inquiry and technological innovation, offering unprecedented opportunities for advancement across various domains.[3,4,5,6]

Philip Russell Wallace predicted the atomic structure of graphene in 1947,[7] but it was considered unstable and unfeasible until its discovery in 2004 by Novoselov et al. using the scotch tape technique for mechanical exfoliation.[8] This technique produced stable, single atomic layers of carbon, known as graphene, which has a 2D honeycomb structure and is a semimetal. Graphene exhibits exceptional properties such as high electron mobility (2.5x10^{-5} cm^{2}V^{-1}s^{-1}),[8,9] high thermal conductivity (3000 WmK^{-1}),[10] low absorption ratio ($A = n\alpha = \%2.3$), flexibility, and significant mechanical strength with its high Young modulus (1 TPa) and intrinsic strength of 130 GPa.[11] Graphene has the highest elastic modulus and tensile strength of all known materials, owing to the sp$_2$ hybridization between the C atoms that form the hexagonal lattice in the atomic structure. All of these exceptional properties of graphene has opened up the fabricate smaller and more sophisticated devices for a wide range of technological applications such as energy storage,[12,13,14] sensors,[15,16,17] drug delivery,[18,19] solar cells,[20] photodetector,[21,22] and transparent conductors, potentially replacing indium tin oxide (ITO) in displays.[23,24,25] The discovery of graphene marked a significant milestone in the field of low-dimensional materials, sparking extensive research into other 2D semiconducting materials due to graphene's lack of

a band gap.[26]

As excellent properties in the 2D limit were identified with graphene, the focus of interest shifted towards 2D structures. Since 2004, research on graphene-like new dozens of 2D materials have grown increasing rapidly and the discovery of new materials continues such as transition metal dichalcogenides (TMDs),[27,28,29] mono-chalcogenides,[30] transition metal carbides, nitrides,[31,32] transition metal dihalides,[33,34] layered double hydroxides,[35] and mono-elemental materials like silicene, and germanene.[36,37,38] 2D materials offer exceptional dynamical, thermal, and mechanical stability at high temperatures,[10,39] expanding their potential applications across various fields. Their remarkable electrical, optical, and mechanical properties make them invaluable for devices such as transistors, photodetectors, and electroluminescent devices.[40] They find utility in both charge-based and non-charge-based technologies, spanning electronics, photonics, and biomedical fields.[41,42,43,44,45,46] Integrating 2D materials into technology enables the development of planar electronic devices with enhanced performance, lower power consumption, and added flexibility and transparency.[47] Overall, the multifaceted functionality of 2D materials serves as a significant source of inspiration for future technological advancements.

While graphene, hBN, and TMDs have been studied for their exceptional isotropic in-plane physical features, the discovery of single-layer black phosphorus (phosphorene or BP) in 2014 led to a significant shift in research focus towards anisotropic 2D materials.[48] The early fascination surrounding BP stems from its unique property of having a layer-dependent direct band gap, unlike graphene, and it demonstrates a carrier mobility that surpasses that of MoS_2. The first synthesis of bulk BP dates back a century ago. In the early stages of 1914, it was synthesized from red phosphorus through the application of high hydrostatic pressure at a temperature below the threshold where transformation occurs rapidly under normal atmospheric pressure.[49] Phosphorus manifests in three distinct allotropes: white, red, and black phosphorus. BP emerges as a rare and highly stable allotrope compared to white and red phosphorus. Structurally, bulk black phosphorus exhibits a layered crystal structure similar to graphite, but its puckered double layers distinguish it from atomically flat graphite-like materials.[50] Electronically, it is a direct gap semiconductor with 0.33 eV band gap energy and mobilities of up to 20 000 $cm^2V^{-1}s^{-1}$ at room temperature.[51,52,53] In addition, Tao et al. demonstrated the Young modulus of few layer BP was found to be 58.6$\pm$11.7 and 27.2$\pm$4.1 GPa for two main orientation, namely, zigzag (ZZ) and armchair (AC), respectively, exhibiting soft nature of the structure (Tao et al., 2015). In addition, its puckered honeycomb lattice led to distinct in-plane structural, electronic, optical, and mechanical anisotropy.[54,55,56] The synthe-

sis of single-layer 2D BP involves stripping ordered phosphorus atoms from bulk black phosphorus, resulting in each phosphorus atom being covalently bonded to three adjacent atoms through sp^3 hybridization. 2D BP has attracted tremendous attention since 2014 due to its remarkable properties, including exceptional carrier mobility (up to 10^3 $cm^2V^{-1}s^{-1}$), thickness-dependent direct band gap (2 eV in single-layer to 0.33 eV in bulk form), and distinctive in-plane anisotropic physical characteristics which makes it superior semiconducting material. The hole effective masses were reported to be 1.140 and 0.182 m_0 while the electron effective masses were shown to be 0.846 and 0.166 m_0 for the single-layer BP, indicating the highly anisotropic behavior of the structure.[57] Moreover, the reported angle-dependent stiffness values for 2D BP are 39 and 92 N/m for the AC and ZZ orientations, respectively.[58] Due to highly anisotropic nature of its buckled structure, high carrier mobility, and tunable band-gap, 2D BP holds significant promise for applications in next-generation nanoscale devices, and optoelectronics.[59,54] Therefore, it is increasingly utilized in various electronic materials, including transistors, alongside other 2D materials such as graphene, boron nitride, and transition metal chalcogenides. However, the utilization of BP encountered obstacles due to its instability and degradation under ambient conditions, as well as the lack of techniques for producing extensive and high-quality structures. Recent studies have discovered that structures similar to BP, known as BP-analogues, show potential as effective solutions to address the limitations of BP. Therefore, they have garnered growing attention, especially mono-elemental 2D group V (pnictogens), owing to their distinctive and stable structures, alongside their exceptional physical and chemical characteristics.

Since the discovery of anisotropic BP in 2014, anisotropic 2D materials have drawn increasing attention, and significant efforts have been focused on demonstrating novel highly anisotropic structures in the 2D limit. Due to their characteristics and uses that depend on orientation, in-plane anisotropic materials have recently become an exciting area of investigation in the scientific community.[60,61] The presence of reduced in-plane symmetry in 2D structures can result in intriguing anisotropic features, hence enhancing their roles and expanding their applications. Specifically, the use of anisotropic 2D materials would be attractive for producing passive optical polarizers and high mobility transistors that can take advantage of decreased back-scattering caused by hot electrons.[62] Utilizing the anisotropic properties of low-symmetry materials has paved the way for applications such as integrated digital inverters[63] and linear dichroic photodetectors.[64] Investigating alternative layered materials that possess enhanced structural in-plane anisotropy would provide the possibility of combining the benefits of 2D materials (such as flexi-

bility, transparency, and a high surface to volume ratio) with fully quasi-one dimensional (1D) characteristics.

Recently, allotropes of single-layer bismuthene have been receiving increasing attention due to their non-radioactive nature, non-toxicity, strong diamagnetism, high stability, low cost, high surface area, strong intrinsic spin-orbit coupling (SOC), thermoelectric properties, and similarity in structure to BP.[65,66,67,68,69,70] Bismuthene, the 2D form of bismuth (Bi), exhibits several structural phases including α, β, γ, p-monoclinic, f-, and b-hexagonal.[71,72] Sing et al. observed that the α and γ phases exhibit metallic and semimetallic character, respectively, while the p-mono, b-hexa, f-hexa, and β structures display semiconducting behavior.[71] In addition, Gou et al. reported the identification of a ferroelectric state in the tilted α phase of bismuthene, which resembles black phosphorus.[72] Moreover, bismuthene displays topological insulator properties owing to its strong SOC.[73,74] Additionally, the semi-metal to semiconductor and trivial to topological transitions were demonstrated under the strain.[75] Through manipulation of strain and SOC strength, the topological phases of the single-layer bismuthene can be adjusted to exhibit many properties, including being a zero band gap metal, a topological semimetal, a null-gap Dirac semimetal, direct and indirect band gap semiconductors, and conventional insulators.[76] Overall, bismuthene has been announced as a promising 2D anisotropic material for various technological applications such as nonlinear optics including as a broadband detector, ultrafast photonics, as a phase modulator, and as an all-optical switcher with a direct band-gap.[77,78,79]

In recent years, transition metal tri- and penta-chalcogenides (MX_3-MX_5; M=Ti, Zr, Hf and X=S, Se, Te)[80,81] have emerged as the most outstanding anisotropic families, attributed to their highly asymmetric geometries and their orientation-dependent vibrational, thermal, electronic, optical, and mechanical properties. Manipulating crystal orientation is crucial for controlling the diversity and uniformity of device performance. Research on TMTCs dates back to the early 1960s, primarily concentrating on bulk crystal structures. 2D single-layer TMTCs, rather than bulk or layered MX_3, are the focus of significant attention in both experimental and theoretical studies. Since 2015, numerous transition metal tri-chalcogenides (TMTCs) have been identified, generally referred to as MX_3 compounds (metal atom, M=Ti, Zr, Hf, V, Nb, and Ta, and chalcogen atom, X=S, Se, and Te), exhibiting quasi-1D van der Waals (vdW) structures.[82,83,84] TMTCs are connected by robust covalent connections in the one-dimensional chain direction, while weak covalent bonds exist between neighboring chains. The presence of such extra bonds strengthens the arrangement of the one-dimensional chains, resulting in the formation of

two-dimensional sheets. 2D sheets of TMTCs, like other 2D structures, stack to form 3D bulk crystals using weak van der Waals forces, giving TMTCs the benefits of both 2D materials and quasi-1D features simultaneously.[85,86,87,88,89] The prismatic MX_6 chains of MX_3 structures are elongated along the *b*-axis to enhance their anisotropic properties. TMDC families are considered crucial materials for advancing the development of future nano-electronics and have wide-ranging potential applications. Low-symmetric structures of TMTCs enable innovative concepts and design flexibility for logic devices and integrated circuits.[88,90] From the TMTCs families, TaS_3, $TaSe_3$, and $NbSe_3$ exhibit metallic behavior at high temperatures, while other sulfides and selenides of Ti, Zr, Hf, and Nb display semiconducting characteristics. Compared to conventional TMDs such as MoS_2, 2D MX_3 structures contain additional X-X bands that introduce states far below the Fermi level, thereby altering the electronic properties of TMTCs.[81] In addition, when subjected to in-plane strain, MX_3 structures demonstrate exceptional transport capabilities and can be utilized as a high-performance thermoelectric material.[91] TMTC members find diverse applications in fields including field emission transistors,[92] solar cells, fuel cells,[93] photodetectors, sensors,[82] and lithium-ion batteries.[94] Manipulating pressure, temperature, and tensile strain can adjust the electrical characteristics of TMTCs. The transit of charge density waves is crucial in making these materials highly significant in the fields of nanoscience and materials science. Particularly among the TMTCs, TaX_3 structures are fascinating 2D materials with highly conductive and lamellar crystal structure whose unit cell is composed of X-Ta-X sandwich layers.[95,96] Tantalum tri-sulfide exhibit two phases, which is monoclinic and orthorhombic.[97,98] Both crystal structures of TaS_3 undergo a phase transition to a charge density wave (CDW) phase at different temperatures. Earlier studies have revealed fascinating physical phenomena in TaS_3, including the emergence and spread of CDW and the shift from a metallic to a semiconducting state.[98,99,100] The orthorhombic phase of TaS_3 exhibits a superconducting phase with a maximum transition temperature of 3.1 K.[101] Monoclinic crystal phase of TaS_3 is the most extensively researched 2D metal due to the display exciting physics related to its CDW instabilities. The electrical transport properties of TaS_3 along the chain axis are quite good and the presence of nearly isolated chains is the most intriguing aspect of the TaS_3 structure.[102]

Another highly anisotropic 2D family is transition metal penta-chalcogenides, known as MX_5 compounds (M= Zr or Hf; X is a chalcogen element S, Se, or Te). The lattice structure of MX_5 family typically exhibits a needle-like or ribbon-like growth pattern, with its longest dimension aligned along the chain direction. Layered MTe_5 structures are very special members of topological insulators. The topological insulators (TI) are a

novel kind of materials that behave as an insulator in its bulk but contains conducting states on its edge or surface, which are topologically protected and robust against perturbations. Such gapless boundary states exist within a bulk insulating gap and are shielded by time-reversal symmetry.[103,104] In addition, 2D topological insulator structures are often referred to as quantum spin Hall insulators (QSH).[105,106] Among the several types of topological quantum materials, semimetals are particularly fascinating due to their ability to approach the Fermi energy, which has a direct impact on their physical properties. The topology is categorized based on the level of band degeneracy in momentum space.[107] MX_5 family has garnered broad attention in the literature as promising candidates for topological insulator materials, primarily owing to their distinctive electronic properties. Among the MX_5 structures, the bulk forms of zirconium and hafnium pentatelluride ($ZrTe_5$ and $HfTe_5$) have been the focus of research for over forty years due to their significant thermo-electric power and fascinating resistivity anomaly.[108,109] They have been found to display a substantial positive magnetoresistance.[110] In addition, there is significant interest in MTe_5 due to its proximity to the phase boundary between a robust TI and a weak TI. $ZrTe_5$ has emerged as an interesting topological material with semimetallic and anisotropic nature.[111,112] The phenomena of chiral magnetic effect,[113] anomalous Hall effect,[114] pressure-driven superconductivity,[115] and extraordinary thermoelectric properties[116] have garnered significant interest in the $ZrTe_5$ structure. Topological insulating behavior is attributed to band inversion between p orbitals of two distinct Te sites at the Γ high symmetry point, a phenomenon highly sensitive to minor changes in atomic positions. The interlayer coupling of the $ZrTe_5$ crystal has a van der Waals nature and is significantly weaker in comparison to the intralayer bonding strength. The $ZrTe_5$ material has an orthorhombic layered structure, which is defined by the Cmcm space group. The $ZrTe_3$ crystal structure consists of triple prisms arranged in chains along the a-direction. These chains are connected to each other through parallel zigzag chains of Te atoms, resulting in a 2D form of $ZrTe_5$ in the a-c direction. The lattice constants of $ZrTe_5$ structure are a=3.987 Å and c=13.727 Å. The $ZrTe_5$ sheets arrange themselves in a layered structure, stacking along the b-direction with a spacing of 7.251 Å.[80] The crystal structure of MX_5 generally grow with a needlelike or ribbonlike morphology, with the longest dimension along the chain direction. The material has a semimetallic electronic nature characterized by ellipsoidal Fermi surfaces that are both tiny and light. These surfaces are centered at the Γ high symmetry point, which is located at the center of the bulk Brillouin zone (BZ).[117,118,119] Bulk $ZrTe_5$ was shown to demonstrate topological edge states at the surface step edge with a bulk band gap of 80 meV predicted to be 3D TI.[80] In addition,

the $ZrTe_5$ single crystal is a layered material, and its 2D form is also predicted to exhibit excellent topological insulating properties with an energy gap of 100 meV. It is classified as a weak topological insulator, lacking any topological surface states on its terminating surface. Various experiments have offered evidence spanning from Dirac semimetal (DSM)[113] to topological insulators (TIs)[120] to Weyl semimetals (WSM).[114] In 2014, Weng et al. made a prediction that 2D $ZrTe_5$ has the potential to be a significant candidate for a topological insulator with a substantial band gap energy. Scanning tunneling microscopy or spectroscopy (STM and STS) investigations and angle-resolved photoemission spectroscopy (ARPES) measurements also reveal the presence of topologically protected states at step edges in 2D form of $ZrTe_5$ structure.[121,122] Shahi et al. observed that variations in characteristics of $ZrTe_5$ can be attributed to varying defect concentrations resulting from different growth procedures. Moreover, the anomalous Hall conductivity of $ZrTe_5$ structure was explained by the presence of Weyl points (WPs) that are generated when time-reversal symmetry (TRS) is disrupted in a strong magnetic field.[123] Moreover, a magnetotransport test on $ZrTe_5$ material revealed the presence of a chiral magnetic effect that arises from the transition between a Dirac and Weyl semimetal.[113] Electronically, single-layer $ZrTe_5$ stands out as one of the most promising candidates for large-gap topological insulators, boasting a direct (indirect) band gap of 0.4 eV (0.1 eV). Single-layer $ZrTe_5$ has attracted significant attention due to its unique properties in topological phase transitions and potential uses in electronic devices.[124] $ZrTe_5$ is resistant to lattice distortions caused by external strains and exhibits behavior characteristic of stacked parallel 2D conduction channels.[125,121] Furthermore, $HfTe_5$ has the same orthorhombic lattice structure as $ZrTe_5$ with space group of Cmcm, but its atomic mass is significantly greater.[126] Tellurides are particularly significant due to their high atomic weight and strong spin-orbit interactions. Given the outstanding properties observed in $ZrTe_5$, the study of anisotropic characteristics and topological features in $HfTe_5$ has emerged as an intriguing area of research. $HfTe_5$ emerges as an alternative 2D topological insulator, showcasing analogous traits to $ZrTe_5$, including strong thermoelectric properties, intriguing resistivity anomalies, and distinctive topological features. The anisotropic electrical-transport characteristics of $HfTe_5$ structure have made it a subject of study as a possible topological insulator in recent years.[110,127,128] Additionally, $HfTe_5$ material exhibits chiral magnetic effect and 3D quantum Hall effect.[129,130,131] The anisotropic nature and topological insulating behavior of $HfTe_5$ makes it a prime candidate for future experiments exploring the quantum spin Hall effect and applications in anisotropic devices, positioning it as a leading contender for 2D topological insulator research.

2D materials have been demonstrated significant promise in nanoelectronics, owing to their remarkable structural, vibrational, electronic, mechanical, and optoelectronic properties. However, the nonmagnetic nature inherent in most 2D structures imposes considerable limitations on their potential applications in spintronic devices. Despite the identification of their exceptional properties resulting from dimensional reduction, the presence of intrinsic magnetism remained elusive during the early stages of research on 2D materials. Therefore, considerable efforts have been directed towards either modifying existing 2D materials to incorporate magnetic features or discovering naturally magnetic 2D materials to overcome this limitation and unlock new possibilities in spintronics. While it is possible to generate localized magnetic moments through defects and/or vacancy,[132,133,134] strain engineering,[135] and ribbon structures,[136,137,138] the challenge persists in achieving long-range ferromagnetic alignment in non-magnetic 2D materials. Thus, researchers have devoted substantial efforts to the demonstration of 2D materials with inherent long-range magnetism. By the successful synthesis of single layers of CrI_3,[139] and $Cr_2Ge_2Te_6$ (CGT),[140] well-known 2D long-range ferromagnets, magnetism at the atomic limit started to become the focus interest. The researchers demonstrated that both single-layer CrI_3 and CGT structures possess a notable perpendicular magnetic anisotropy (PMA), which offers benefits such as decreased energy usage and improved thermal stability for storing high-density information.[141,142,143] However, the practical application of CrI_3 (with a Curie temperature of 45 K) and $Cr_2Ge_2Te_6$ (with a Curie temperature of 30 K) is limited in spintronic applications due to their comparatively low Curie temperatures. Over the past decade, there has been a growing interest in studying new 2D magnetic materials that have higher Curie temperatures for nanoscale spintronic devices. Numerous 2D magnetic structures have been demonstrated, such as $MnSe_2$,[144] VSe_2,[145] Fe_3GeTe_2 (FGT),[146] and CrSBr (CSB).[147] Antiferromagnetic structures have attracted more attention than ferromagnetic ones among magnetic ultra-thin materials.[148] This is because they offer several advantages, including spin superfluidity,[149] minimal spin-dipole interaction,[150] lack of net magnetization, and absence of stray fields.[151] In addition, antiferromagnets are more resistant to small disrupting fields and demonstrate exceptional performance in the high-frequency range with incredibly rapid dynamics.[152,153,154] Manganese phosphorus tri-sulfide ($MnPS_3$), a new type of magnetic ultra-thin material, has recently attracted significant attention. It is highly sought after due to its non-toxic properties,[155] cost-effectiveness, and remarkable stability.[156] $MnPS_3$ is a van der Waals (vdW) antiferromagnet on a honeycomb lattice in its bulk form and its fundamental structural and magnetic properties have been studied since the 1980s.[157] It exhibits a Néel temperature

(T_N) of around 78 K[158] and a magnetic propagation vector of $\vec{k} = (0, 0, 0)$. It possesses monoclinic crystal structure (space group C2/m), with lattice parameters a, b, and c 6,07, 10.52, and 6.80 Å, respectively and shows localized magnetic moment. Inelastic neutron diffraction and magnetic susceptibility investigations demonstrate that the Mn atoms in $MnPS_3$ are in a high spin state, characterized by a spin value of $S = 5/2$, and possess a $3d$ shell that is half filled.[159] Easy magnetization axis of the bulk structure is oriented along the out-of-plane anisotropy.[160] The experimental band-gap of the bulk form of the material is 3.0 eV with direct band-gap which is a wide-gap antiferromagnetic semiconductor. The relatively weak van der Waals (vdW) binding strength, characterized by an energy density of 0.25 J/m^2, enables the easy production of a 2D ultra-thin form of $MnPS_3$ using an easier exfoliation approach instead of the more difficult molecular beam epitaxy (MBE) method.[161,162] Near-field infrared spectroscopy measurements reveal a transition in symmetry from C2/m to P$\overline{3}$1m in single-layer structures.[163] 2D $MnPS_3$ shows a direct band gap antiferromagnetic (AFM) semiconducting behavior similar to its bulk form.[161] Single-layer $MnPS_3$ was reported to display ultrafast domain-wall dynamics and the spin photogalvanic effect.[164,165] Shiomi et al. showcased the management of AFM domains within $MnPS_3$ crystals using magnetoelectric cooling techniques, while also observing the phenomenon known as the magnon Nernst effect.[164] Moreover, Li et al. demonstrated that 2D $MnPS_3$ shows antiferromagnetism-valley coupling, valley-dependent optical properties and topological domain wall states.[166] Additionally, the nonreciprocal spin Seebeck effect and spin transport features of $MnPS_3$ structure were showed.[167]

In this thesis, we focus on the structural, magnetic, vibrational, electronic, optical and elastic properties of low-dimensional, ultra-thin anisotropic structures using DFT-based first principles ab-initio calculations. Anisotropic materials are of significant interest in scientific research and technological applications due to their unique orientation-dependent properties, which vary based on the axis along which they are measured. The anisotropy of the structure allows their structural, magnetic, thermal, electronic, optical, and mechanical characteristics to differ significantly along different axes, enabling their use in advanced device applications where specific directional properties are beneficial. For instance, ultra-thin anisotropic structures can be used to create field-effect transistors (FETs) with tailored electronic properties by exploiting the directional dependence of charge carrier mobility to enhance device performance. Their unique optical properties, such as direction-dependent absorption and emission, make them ideal for sensitive photodetectors and various types of sensors. In addition, anisotropic thermal conductivity can improve thermal management in electronic devices, as materials that conduct heat well in

one direction but poorly in another can efficiently dissipate heat, enhancing device reliability and performance. Additionally, their anisotropic magnetic properties are particularly intriguing; these properties can lead to direction-dependent magnetic behavior, such as varying magnetic anisotropy energy, which is crucial for applications in spintronics and magnetic storage devices. The mechanical anisotropy of these materials can be tailored for applications requiring high strength in one direction and flexibility in another, which is particularly useful in flexible electronics and nanocomposites. Directional mechanical properties also allow for strain engineering, where applying mechanical strain can modify the material's electronic and optical properties, enabling tunable device characteristics. Moreover, low-dimensional anisotropic materials exhibit novel quantum phenomena due to their reduced dimensionality and directional properties. These phenomena include anisotropic superconductivity, magnetoresistance, and quantum Hall effects, which are of great interest for fundamental physics research and potential quantum computing applications. Furthermore, their direction-dependent electronic properties can be optimized for improved light absorption and charge carrier separation, enhancing the efficiency of solar cells. Anisotropic materials can also provide high ion mobility along specific directions, leading to better performance in energy storage devices. The study of low-dimensional anisotropic materials are essential due to their unique directional properties that offer advantages in various applications, from electronics and opto-electronics to energy devices and beyond. Their ability to exhibit different properties along different axes allows for the design of highly specialized materials and devices with superior performance, paving the way for advancements in technology, and fundamental science. In this context, we first investigate 2D anisotropy in novel highly anisotropic single-layer transition metal pentachalcogenides in Chapter 3 and transition metal trichalcogenides in Chapter 4. Then, we study black phosphorus-like anisotropic tilted α-bismuthene structure in Chapter 5. Finally, we focus on edge- and width-dependent 1D anisotropy in magnetic ultra-narrow manganese phosphorus trisulfide ($MnPS_3$) nanoribbon structures in Chapter 6.

CHAPTER 2

THEORETICAL BACKGROUND AND COMPUTATIONAL METHODOLOGY

Understanding and solving the complex behaviors of systems comprising multiple interacting electrons present a formidable challenge within the realm of quantum mechanics. Density Functional Theory (DFT) has emerged as a valuable approach in light of the complexities involved in solving such systems. Widely embraced and highly effective, DFT serves as a key quantum mechanical method for exploring the fundamental characteristics of these interacting many-electron systems, encompassing solids and molecules alike. Its application spans across diverse domains including physics, chemistry, and materials science, facilitating investigations into a numeorous of properties such as ground state analysis, magnetic behavior, vibrational dynamics, electronic structure, optical, and mechanical properties. This section of the thesis delves into the fundamental principles of computational many-body theory and the associated approximate functionals crucial for understanding this domain.

2.1. The Many Body Problem

The Schrödinger equation stands as a cornerstone in contemporary research and applications, especially concerning the description of quantum particles and their interactions. Significance of the schrödinger equation lies in its ability to accurately predict the behavior of particles in diverse systems. In particular, when dealing with multiple particles, the solution to the Schrödinger equation manifests as the many-body wavefunction, providing invaluable insights into the collective behavior of the quantum particles that interact with each other and enabling the analysis of complex quantum phenomena. The quantum mechanical wave function includes all the information regarding the attributes of a given system. The wave function, denoted as Ψ, has a crucial significance in the field of quantum mechanics. The mathematically expression of the wave function of any system in the non-relativistic regime can be derived by solving the time-independent Schrödinger equation,

$$\hat{H}\Psi = E\Psi \tag{2.1}$$

where the operator $\hat{H}$ is the energy operator known as the Hamiltonian operator, E is the energy eigenvalue of that quantum state, and Ψ represents the wave function associated with each energy eigenvalue. In the conventional framework of matter modeling, the Schrödinger equation is typically formulated to describe the behavior of a system containing multiple electrons. When dealing with an N-body system that involves interactions between particles beyond electrons, the Hamiltonian has a wider range of scope. This comprehensive approach allows for considering various particles and their complex interactions within the system. When considering an many-body system, the Hamiltonian can be expressed as follows:

$$\begin{aligned}\hat{H} = &-\frac{\hbar^2}{2m_e}\sum_i \nabla_i^2 - \sum_A \frac{\hbar^2}{2M_A}\nabla_A^2 - \frac{1}{4\pi\varepsilon_0}\sum_{i,A}\frac{Z_A e^2}{\mid \vec{r_i} - \vec{R_A} \mid} \\ &+ \frac{1}{2}\sum_{i\neq j}\frac{1}{4\pi\varepsilon_0}\frac{e^2}{\mid \vec{r_i} - \vec{r_j} \mid} + \frac{1}{2}\sum_{A\neq B}\frac{1}{4\pi\varepsilon_0}\frac{Z_A Z_B e^2}{\mid \vec{R_A} - \vec{R_B} \mid}\end{aligned} \tag{2.2}$$

The Hamiltonian operator encompasses all the terms that describe all possible interaction within a quantum mechanical system consisting of N electrons. where $\hbar$ is the Planck constant, $1/4\pi\epsilon_0$ is the Coulomb constant, the indices i and j denote the electrons, e is the electron charge, m_e is the electron mass, M_A is the mass of nuclei, Z_A and Z_B are the nuclear charges, and r and R represent the spatial coordinate of corresponding electron or atom, respectively. The first and second terms represent the kinetic energy of the system with respect to the electrons and nuclei. Due to the mass of nuclei is significantly larger than the mass of electrons, as implied by the Born-Oppenheimer Approximation (Born and Oppenheimer, 1927), the second term can be neglected. The third term is the Coulombic interactions between electrons and nuclei (electron-nucleus attraction). Lastly, the fourth (electron-electron repulsion) and fifth (nucleus-nucleus repulsion) terms account for the Coulomb repulsion between electrons and nuclei, respectively. Solving the Schrödinger equation offers valuable insights into the energy states of simple quantum systems like the hydrogen atom or a confined electron. However, when dealing with more complex systems with multiple interacting particles or intricate geometries, the Schrödinger equation becomes more complicated, making it increasingly challenging and nearly impossible to solve without any approximation. Therefore, many approximations have been proposed to simplify the solution process for Schrödinger equation of a many-body systems.

2.1.1. Born-Oppenheimer Approximation

The Born-Oppenheimer approximation is a fundamental simplification in comprehending complex quantum systems. It was formulated in 1927 by Max Born and J. Robert Oppenheimer, and is a method that involves the separation of the electron and nuclei degrees of freedom. The Born-Oppenheimer approximation is based on the fundamental assumption that nuclei possess significantly greater mass in comparison to the electrons, enabling researchers to focus primarily on the electronic behavior while treating the nuclei as stationary. Hence, the contribution of the kinetic energy of the nuclei in Equation 2.2 can be neglected, given its insignificance compared to the kinetic energy of electrons. Furthermore, the fifth term, representing the repulsion between nuclei, remains constant due to the fixed arrangement of nuclei. With these considerations, the Hamiltonian, focusing on the remaining three terms, adopts the structure commonly referred to as the electronic Hamiltonian.

$$\hat{H} = -\frac{\hbar^2}{2m_e}\sum_i \nabla_i^2 - \frac{1}{4\pi\varepsilon_0}\sum_{i,A}\frac{Z_A e^2}{\mid \vec{r_i} - \vec{R_A} \mid} + \frac{1}{2}\sum_{i\neq j}\frac{1}{4\pi\varepsilon_0}\frac{e^2}{\mid \vec{r_i} - \vec{r_j} \mid} \tag{2.3}$$

Electronic Hamiltonian captures the essential interactions among electrons within the system, facilitating a focused analysis of electronic properties and behaviors. With this approximation, the solution to the Hamiltonian, which is the wavefunction, becomes dependent on the electronic coordinates ($\vec{r_i}$), as the nuclear motion is considered to be relatively slow and can be treated as fixed. Consequently, the corresponding Schrödinger equation can be represented as follows,

$$\hat{H}_e \Psi_e(\{r_i\}) = E_e \Psi_e(\{r_i\}) \tag{2.4}$$

The solution to Schrödinger equation under the Born-Oppenheimer approximation (Eq. 2.4), appears to be more straightforward compared to its most general form. However, despite its apparent simplicity, the electron-electron interaction term in Eq. 2.3 poses a challenge due to the correlated motion of electrons. Therefore, it is necessary to consider the instantaneous coordinates of each electron, which effectively entails the utilization of 3^N variables for an N-electron system. Various approximations were suggested to solve the Schrödinger equation for N-interacting electrons. The primary objective of these approximations is to transform the N-electron Schrödinger equation into an effective one-electron Schrödinger equation. One such approach is Thomas-Fermi Model and Density

Functional Theory (DFT) , both of which consider electron density as a fundamental quantity.

2.1.2. Thomas-Fermi Model

The concept of expressing electronic energy in relation to electron density was initially proposed by Llewellyn Thomas and Enrico Fermi in the 1927. The Thomas-Fermi (TF) theory assumes that electron-electron and electron-nucleus interactions are treated within classical frameworks. The TF model was groundbreaking in its proposal to utilize

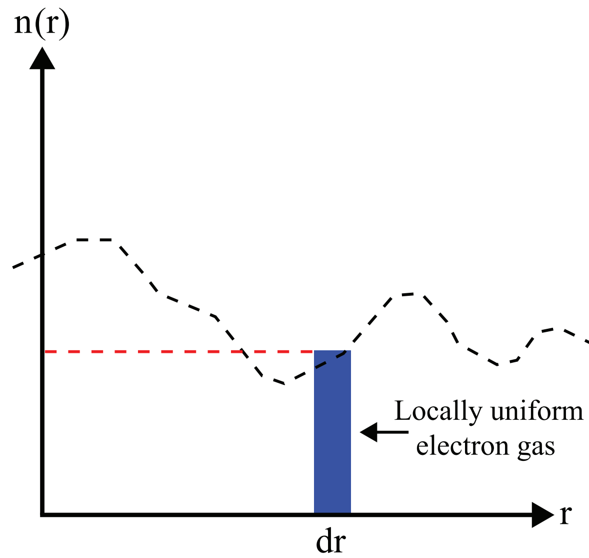

Figure 2.1. The figure illustrating the fundamental concept of the local density approximation and Thomas-Fermi theory depicts a radial slab, dr, where the local charge density n(r) corresponds to the density of a uniform homogeneous electron gas.

electronic charge density as the fundamental variable instead of the wavefunction, making it the earliest manifestation of density functional theory. The concept can be readily grasped with the assistance of Fig. 2.1. Even though the charge density corresponds to a non-uniform electron gas, the number of electrons within a given element, dr, can be represented as n(r)dr, where n(r) denotes the charge density for a uniform electron gas at that specific point. The TF model demonstrates that the overall kinetic energy of the electrons can be exclusively described in relation to the electron density n(r) that varies over space, expressed as:

$$T[n] = C_F \int n^{5/3}(r)dr \tag{2.5}$$

where C_F (Fermi coefficient) is equal to 2.81 in atomic units and $n(r)$ is the electron

density. The total energy of the system, in terms of electron density, can be obtained by including interaction terms for electron-electron and electron-nucleus interactions, as follow:

$$E[n] = C_F \int n^{5/3}(r)dr + \frac{1}{2}\int\int \frac{n(r_1)n(r_2)}{\mid r_1 - r_2 \mid}dr_1dr_2 - Z\int \frac{n(r)}{r}dr \tag{2.6}$$

The second and third terms correspond to electron-electron and electron-nucleus interactions, respectively. After identifying the total energy functional, the ground state energy of the system can be computed by minimizing the functional, E[n], with respect to all possible electron densities, n(r), which must adhere to the following condition:

$$N = \int n(r)d^3r \tag{2.7}$$

The precision of the TF equation is constrained due to the approximate nature of the derived expression for the kinetic energy. Additionally, the approach neglected to account for the exchange and correlation effects between electrons a consequence of the Pauli exclusion principle. Dirac developed a local approximation method to describe the electron exchange, yielding an electron energy functional within an external potential V_{ext}, as follows:

$$\begin{aligned} E[n] = C_1 \int n^{5/3}(r)dr + \int drV_{ext}(r)n(r) + \\ C_2 \int n^{4/3}(r)dr + \frac{1}{2}\int\int \frac{n(r_1)n(r_2)}{\mid r_1 - r_2 \mid}dr_1dr_2 \end{aligned} \tag{2.8}$$

where $\int n^{5/3}(r)$ is the local density approximation of the kinetic energy, $C_1 = 2.81 = 3/10(3\pi^2)^{2/3}$ Hatree, $\int n^{4/3}(r)$ represents the exchange with $C_2 = -3/4(3/\pi)^{1/3} = -0.739$ Hatree and $\frac{1}{2}\int\int \frac{n(r_1)n(r_2)}{|r_1 - r_2|}dr_1dr_2$ is the classical electrostatic Hartree energy.

The main goal of the TF model is not only centered on precisely ascertaining the energy of the lowest possible condition. However, its primary objective is to illustrate that the overall energy of the system can be efficiently examined and comprehended by utilizing the concept of electron density. The TF model has found application in determining the equation of state for elements. However, the approach starts with a simplistic approximation, overlooking crucial aspects such as the chemistry and physics underlying the shell structure of atoms and the binding energy of molecules. It fails to offer an accurate depiction of electrons within substances. The TF approximation is inadequate for modern electronic structure calculations. Nonetheless, despite its shortcomings, the TF model has been instrumental in advancing the development of more precise quantum mechanical

models and continues to hold significance as a fundamental concept in condensed matter physics.

2.1.3. Density Functional Theory

In order to comprehend how a specific system behaves, obtain information about the density of the system, and predict its response to external perturbation, it is essential to solve the Schrödinger equation for that system. The precise solution of the equation is only achievable for a limited number of small systems, such as a particle confined in a box, a hydrogen atom, and a simple harmonic oscillator. The equation is unsolvable exactly for many many-electron systems. Understanding and solving the complex behavior of interacting many-electron systems poses a major challenge in quantum mechanics. Among various methodologies, Density Functional Theory (DFT) stands out as one of the most common quantum mechanical methodologies used to approximate solutions to the Schrödinger equation in many-body systems. Renowned for its success, DFT serves

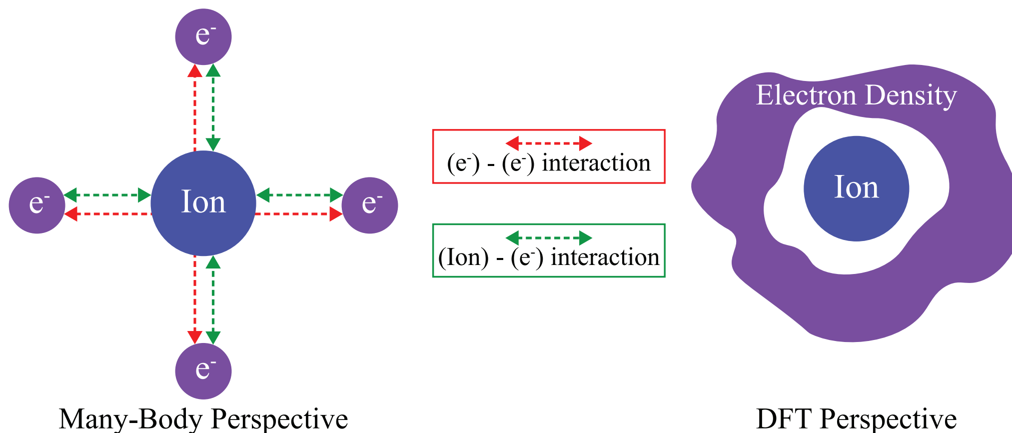

Figure 2.2. DFT approach to a many-body system.

as a highly powerful approach for modeling and describing the ground state properties, structural magnetic, vibrational, electronic, and optical properties of metals, semiconductors, and insulators. It reduces computational cost and its applications span multiple disciplines including physics, chemistry, biology, and materials science. DFT has proven its effectiveness not only in analyzing conventional bulk and low-dimensional materials but also in elucidating the properties of intricate molecules. The term "density functional theory" originates from the utilization of functionals grounded in electron density. By employing the functionals, which are based on electron density $[n(r)]$, it effectively analyzes the properties of many-electron systems. It is a theoretical framework that focuses

mainly on the charge density as the fundamental physical feature in the ground state. The primary concept behind DFT is to represent the lowest energy state of a system of interacting fermions through a functional of the electronic density, rather than directly using the many-body wavefunction. Preferring electron density over the wavefunction simplifies the dimensional complexity of the problem. Such a system, governed by the conservation principle of electron number, confines the behavior of the entire many-body system purely from $3N$ dimensions to three spatial coordinates, owing to the fact that $n(r)$ inherently possesses three degrees of freedom. Reducing the number of degrees of freedom facilitates the application of DFT to complex structures and improves the manageability of calculations. The electron density is defined as:

$$n(r) = N \int ... \int \mid \Psi(r_1, r_2, ..., r_N) \mid^2 dr_1 dr_2 ... dr_{N-1} \tag{2.9}$$

The function $n(r)$ quantifies the probability of locating any of the N electrons, assuming that the remaining N-1 electrons are positioned randomly. $\Psi(r_1, r_2, ..., r_N)$ is the solution to the Schrödinger equation, representing the quantum state of N electrons, where each r_i denotes the position of an electron. In summary, the use of DFT has garnered

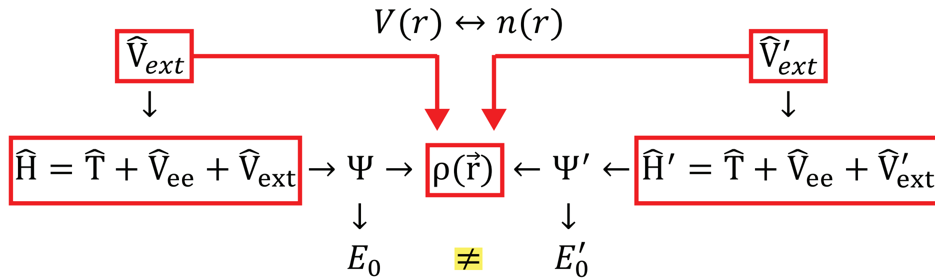

Figure 2.3. Depiction of the first Hohenberg-Kohn theorem.

attention across several disciplines for several reasons: its simplicity in working with a 3-dimensional density, n(r), compared to a 3N-dimensional wave function, (Ψ); its computational efficiency; and its capability to analyze infinite periodic systems.

2.1.4. Hohenberg-Khon Theorems

Following the introduction of the Thomas-Fermi model, Hohenberg and Kohn in 1964 developed Density Functional Theory (DFT) as a precise framework for many-body systems. Hohenberg-Khon theorems enable the representation of the electronic Hamiltonian in terms of the electron density, denoted as n(r). The Hohenberg-Khon model

consists of two fundamental theorems. The first theorem of the Hohenberg-Kohn approach establishes a unique relationship between an external potential $V_{ext}(r)$ (such as the Coulomb potential stem from nuclei) and the electron density n(r). It asserts that there cannot be two different external potentials leading to the same electron density as seen in Fig. 2.3. According to the theorem, the ground and excited-state properties of a quantum mechanical system can be determined solely by its ground state electron density functional.

The second theorem posits that the electron density functional achieving the minimum total energy, denoted as $E_{[n]}$, corresponds to the precise ground-state density of the system.The global minimum of this functional can be obtained by variational derivation, by initially selecting a trial function that embodies both its Hamiltonian and wave function. Thus, employing the trial wave function enables the determination of the ground state energy for a system governed by a Hamiltonian derived from an external potential, V_{ext}. Consequently, the total energy functional for a specific external potential can be expressed as follows:

$$E = \frac{< \Psi_0 \mid H \mid \Psi_0 >}{< \Psi_0 \mid \Psi_0 >} =< H >= T[n] + V_{int}[n] + E_{II} \int d^3 r V_{ext}(r) n(r) \qquad (2.10)$$

T$[n]$ represents the kinetic energy of electrons, V_{int} is the energy of electron-electron interactions, and E_{II} refers to the interaction energy between nuclei. F_{HK}[n] is a constant which indicates to the total kinetic energy of electrons.

$$T[n] + V_{int}[n] = F_{HK}[n] \qquad (2.11)$$

Hohenberg-Kohn theorems offer an approach to compute the ground state energy of many-body systems using an electron density functional. However, no specific information is provided regarding the type of energy functional employed. Therefore, the energy functional is unknown.

2.1.5. Kohn-Sham Equations

Kohn and Sham developed a model building upon the Hohenberg-Kohn theorem, allowing for the minimization of the energy functional by adjusting the charge density across all possible densities containing N electrons (a many-body particle system) in 1965. They propose a conceptual framework where the many-body particle problem is viewed

as a system of non-interacting electrons navigating within an effective potential. The

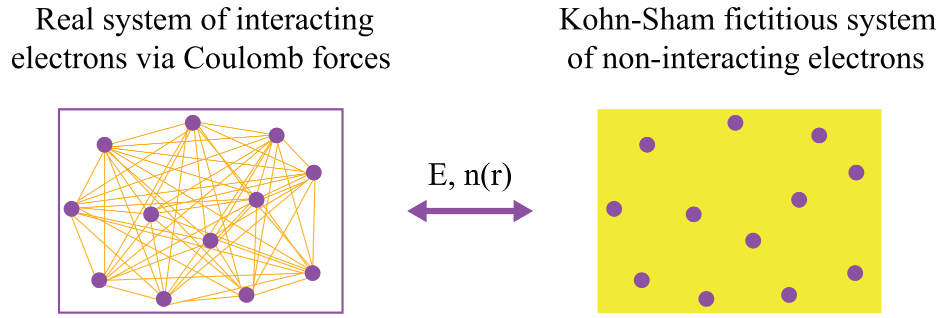

Figure 2.4. Illustration of the real system of electrons that interact with each other and the Kohn-Sham fictitious system of non-interacting electrons with each other.

purpose of Kohn-Sham is to determine the electron density in the lowest energy state of a system of interacting electrons by solving the Schrödinger equation for non-interacting electrons. Kohn and Sham facilitated practical implementations of DFT by introducing the following hypothesis: i- A system of interacting electrons can be mapped onto an auxiliary system of non-interacting electrons, sharing the same ground state charge density $n(r)$ as the interacting system, ii- The auxiliary Hamiltonian is selected to include the conventional kinetic operator and an effective potential, $V_{eff}(r)$, exerted on an electron at a given point r as shown in Fig. 2.4. The Hamiltonian incorporates the effects of electron-electron interactions, often known as many-body effects, by including an additional factor termed the exchange-correlation functional, $\mathrm{E}_{xc}[n]$. The expression for the ground-state energy functional under the Kohn-Sham principles can be formulated as:

$$E_{KS} = \int n(r)V_{ext}(r)d^3r + F_{HK}[n] = \int n(r)V_{ext}(r)d^3r + T[n] + E_H[n] + E_{xc}[n] \quad (2.12)$$

where E_{exc} is exchange and correlation energy, and $E_H[n]$ represents the Hartree energy and can be written as:

$$E_H[n] = \frac{e^2}{2} \int d^3r d^3r' \frac{n(r)n(r')}{\mid r - r' \mid} \quad (2.13)$$

An essential step involves defining an effective potential, which is formulated as:

$$V_{\text{eff}} = \frac{\delta \left[\int n(\mathbf{r})V_{\text{ext}}(\mathbf{r})\, d\mathbf{r} + E^{\text{Hartree}}[n] + E^{\text{xc}}[n] \right]}{\delta n(\mathbf{r})} \quad (2.14)$$

The effective potential can be expressed in the following form:

$$V_{\text{eff}} = V_{\text{ext}}(\mathbf{r}) + \int \frac{n(\mathbf{r}')}{|\mathbf{r} - \mathbf{r}'|} d\mathbf{r}' + V_{\text{xc}}(\mathbf{r}) \tag{2.15}$$

Here, $V_{xc}(r)$ represents the exchange-correlation potential obtained from the exchange-correlation energy. The accuracy of findings derived from the Kohn-Sham equations is notably impacted by the selection of the exchange-correlation functional, which serves as an approximation to the true exchange-correlation potential. In addition, the ground state density for the Kohn-Sham system of non-interacting electrons can be expressed as:

$$n(r) = 2 \sum_i |\psi_i(r)|^2 \tag{2.16}$$

By utilizing the formulation for the effective potential, the Schrödinger equation in Kohn-Sham Density Functional Theory (DFT) can be restated as an equation resembling that of a single-electron system:

$$\hat{H}_{KS} \phi_i(r) = E_i \phi_i(r) \tag{2.17}$$

The parameters H_{KS} and E_i represent the effective Kohn-Sham Hamiltonian and energy eigenvalues, respectively.

$$\left[-\frac{1}{2} \nabla^2 + V_{\text{eff}} \right] \phi_i = E_i \phi_i \tag{2.18}$$

where ϕ_i indicates the eigenfunctions, specifically referred to as the Kohn-Sham one-electron orbitals, that govern the electron density. The relationship between Kohn-Sham orbitals and the ground-state electron density functional is expressed as follows:

$$n(r) = \sum_{i=1}^{N} \mid \phi_i \mid^2 \tag{2.19}$$

Since the effective potential V_{eff} is dependent on the density n(r), solving the Kohn-Sham equation requires a specific procedure: (1) start with an initial estimation of the electron density (assume a trial density function), (2) derive the effective potential based on this density, (3) calculate corresponding Kohn-Sham orbitals, ϕ_i, and (4) evaluate the updated electron density corresponding to these orbitals and compare it with the initial approximation. The iterative process continues until successive outputs converge to a consistent energy level.

The self-consistent approach is a basic method in various scientific domains, especially in quantum mechanics, electromagnetism, fluid dynamics, material science, com-

putational physics, and chemistry. The capacity of the approach to handle complex relationships and develop solutions renders it an essential instrument for comprehending and investigating diverse scientific domains. This effective approach entails solving a series of equations repeatedly until a dependable solution is achieved. The self-consistent method incorporates feedback between the solution and the problem, taking into consideration the mutual dependency of variables. It leads to a more precise characterisation of sophisticated systems. During iterative process, the solution is continuously refined until it reaches a self-consistent state that fulfills all constraints and equations. Within the framework of density functional theory, a notable application of self-consistent approach is embodied in the Kohn-Sham equations. These equations provide a solid basis for solving the many-body Schrödinger equation and examining electronic structure and characteristics in various systems. By mapping interacting electron systems onto non-interacting electrons governed by an effective potential, Kohn-Sham equations enable precise characterization of materials and molecules at atomic and molecular scales. Thus, despite their approximations, they stand as an indispensable tool in the interdisciplinary fields of physics, chemistry, material science, and biology for investigating complex systems.

2.1.6. Exchange-Correlation Functionals

Exchange-correlation functionals are crucial in DFT for investigating the electronic structure of atoms, molecules, and solids using computational methods. Within a system including many-electrons, the exchange-correlation functionals ($E_{xc}[n]$) approximately depict the exchange and correlation effects arising from their interactions. An accurate approximation of the exchange-correlation can provide a realistic electron density and the ground state energy. Hence, it is crucial to employ the accurate approximation of exchange-correlation energy for a given material. Although DFT offers a reliable explanation of the ground state properties in theory, the precise nature of the exchange-correlation potential that may effectively account for all interactions between electrons is still unidentified. Hence, the impacts of the Pauli exclusion principle and the Coulomb potential on electron-electron interactions need to be approximated by suitable functionals based on electron density. Nevertheless, there are widely accepted approximations to the exchange-correlation potential that enable accurate calculation of certain physical quantities. The Local Density Approximation (LDA) and the Generalized Gradient Approximation (GGA) are two methods used in computational physics and chemistry to approximate the electron density in a system.

Local Densiy Approximation (LDA): The Local Density Approximation (LDA), introduced by Kohn and Sham in 1965, a basic approximation applicable to systems with gradually varying density. It is one of the most commonly employed approximations for the exchange-correlation potential. According to LDA, the exchange-correlation energy is presumed to be equivalent to that of a uniformly distributed electron gas at the same coordinates, with the functional being dependent on coordinates as seen in Fig. 2.5.

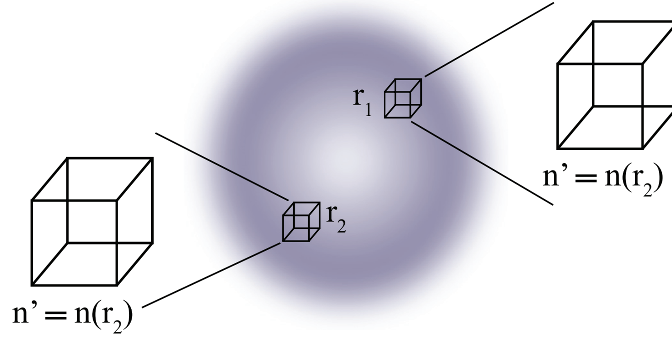

Figure 2.5. Representation of the local density approximation involves substituting the precise exchange-correlation energy density at each point r with that of a uniform, homogeneous electron gas having a density equivalent to n(r).

Therefore, the inhomogeneous system of a molecular or crystalline structure is approximated by utilizing the local density of the homogeneous electron gas. Despite its fundamental approximation, LDA yields highly highly accurate results, particularly for bulk materials, and forms the foundation of DFT codes. It performs effectively even in systems with rapidly varying charge densities and is particularly works for metallic systems. However, it tends to underestimate atomic ground-state energies and ionization energies, while overestimating binding energies. The system is divided into volumes with uniform electron densities, following the local density approximation. The exchange-correlation energy of an inhomogeneous system can be written as (Ceperley and Alder, 1980):

$$E_{xc}^{LDA}[n] = \int n(r)\varepsilon_{xc}^{hom}[n(r)]d^3r \tag{2.20}$$

Here, ε_{xc}^{hom} represents the exchange-correlation energy density of a homogeneous electron gas with an electron density, $n(r)$. The LDA method provides accurate approximations for several ground state parameters such as lattice constant, density of states, band structure, stiffness, Poisson ratio, and bulk moduli. Although the decay of potentials in finite systems is exponential when using LDA, this decay is significantly slower and follows a Coulombic pattern in real systems.

Generalized Gradient Approximation (GGA): In systems characterized by rapidly vary-

ing charge densities, the exchange-correlation energy significantly departs from the uniform result, potentially making the LDA approximation inadequate. Beyond LDA, the Generalized Gradient Approximation (GGA) incorporates gradient and higher-order spatial derivatives of the electron density to rectify this deviation. In GGA, the electron concentrations exhibit spatial variation, rather than remaining constant throughout divisions, and fluctuate in a gradient manner. The exchange-correlation functional can be expressed using the Generalized Gradient Approximation as follows:

$$E_{xc}^{GGA}[n] = \int f^{GGA}(n(r), \nabla n(r)) d^3r \tag{2.21}$$

where $n(r)$ represents the possible electron density, and $\nabla n(r)$ is the gradient of the electron density. Because GGA rely on the gradient of the electron density, GGA functionals are referred to as semi-local functionals. Some often employed and effective types of Generalized Gradient Approximation (GGA) are Perdew, Burke, and Ernzerhof (PBE) (Perdew et al., 1996), Perdew and Wang (PW91) (Perdew and Wang, 1992), and Becke (B88) (Becke, 1988).

2.1.7. Heyd-Scuseria-Ernzerhof (HSE) Functional

Hybrid-GGAs introduced by Becke try to overcome the difficulties encountered by GGAs by including exchange energy from Hatree-Fock expression into local/semi-local GGA/LDA exchange and correlation functions. It is possible to estimate the precise electronic band dispersions of materials through DFT calculations utilizing LDA and GGA functionals. However, both approaches tend to underestimate the band gap of the structures due to their limited precision and efficiency in calculating the true exchange-correlation energy of the systems. Consequently, the experimentally observed electronic band gap may not be accurately approximated. Heyd-Scuseria-Ernzerhof (HSE) functional has emerged as a promising solution to address the limitations of traditional exchange-correlation functionals. The hybrid-functionals combine the strengths of both Hartree-Fock and DFT methods, offering improved accuracy in predicting electronic properties. HSE functional employs a sophisticated approach that combines a fraction of exact exchange obtained from Hartree-Fock (HF) theory with the exchange computed from traditional density functionals (GGA or LDA). In this approach, the correlation component is solely derived from the standard density functionals, resulting in a balanced treatment

of electronic interactions within the system. As an example, HSE functional incorporates 25% of the exact exchange derived from Hartree-Fock theory with 75% of the exchange derived from the Perdew-Burke-Ernzerhof (PBE) functional, a common form of generalized gradient approximation (GGA) exchange. HSE functional has gained popularity for their ability to significantly reduce computational costs while offering enhanced accuracy. They achieve this by decomposing exchange interactions into short-range (SR) and long-range (LR) terms and defining the Coulomb operator accordingly. This decomposition enables a more efficient treatment of electronic interactions, leading to improved computational efficiency without sacrificing accuracy. For the HSE functional, exchange-correlation energy of the material can be expressed as follows:

$$E_{xc}^{HSE} = aE_x^{HF,SR}(\omega) + (1-a)E_x^{PBE,SR}(\omega) + E_x^{PBE,LR}(\omega) + E_c^{PBE} \tag{2.22}$$

Here, $E^{HF,SR}x$ denotes the contribution from short-range Hartree-Fock (HF) exchange, $E^{PBE,SR}x$ and $E^{PBE,LR}x$ represent the short- and long-range components of the Perdew-Burke-Ernzerhof (PBE) exchange energy, and Ec signifies the PBE correlation energy. The parameter a determines the weight of HF exchange in the hybrid functional. By blending exact exchange from HF theory with exchange from traditional density functionals, HSE-type functionals strike a balance between accuracy and computational efficiency. This approach significantly improves the prediction of electronic band gaps and other properties, making it a valuable tool in material sciences, condensed matter physics, and computational chemistry alike.

2.1.8. Hellman-Feynman Theorem

The Hellmann-Feynman theorem (1939), attributed to Henry C. Hellmann and Richard P. Feynman, correlates the derivative of a system's total energy concerning an external parameter with the expected value of the derivative of the Hamiltonian. The theorem states that the force acting on a nucleus may be expressed solely in terms of the charge density, $n(r)$, without considering the effects of electron exchange, correlation, and kinetic energy. One of the primary advantages of the Hellmann-Feynman theorem lies in its computational efficiency. The theorem offers a straightforward method to compute the derivative of energy directly from the eigenstates and eigenvalues of the Hamiltonian, eliminating the requirement to solve the Schrödinger equation for different parameter values. It defines a mathematical relationship between the energy of system and

the associated forces. In addition, the Hellmann-Feynman theorem plays a crucial role in DFT-based calculations as it enables the determination of optimal structural parameters, including lattice constants, bond lengths, and bond angles. The Hellmann-Feynman theorem states that for any parameter that affects the energy eigenvalue and corresponding eigenstate of a Hamiltonian, the derivative of the energy eigenvalue with respect to that parameter is equal to the expectation value of the derivative of the Hamiltonian with respect to the same parameter. Assuming the parameter represents the spatial position of an atom located at R, for a Hamiltonian that is a function of the parameter R with eigenfunction $\phi(R)$ and eigenvalue $E(R)$, the derivative of the energy with respect to R equals the expectation value of the derivative of the Hamiltonian with respect to R. Moreover, the minimum energy corresponds to zero force. Therefore, the corresponding relationship is given by:

$$\frac{\partial E}{\partial \mathbf{R}} = \left\langle \Psi_0 \left| \frac{\partial \hat{\mathbf{H}}}{\partial \mathbf{R}} \right| \Psi_0 \right\rangle \tag{2.23}$$

The theorem is particularly useful for finding the force associated with any parameter in the Hamiltonian of a system, such as the position of a nucleus R. The force can be derived by taking the negative derivative of the energy eigenfunction.

$$F_I = -\frac{\partial E}{\partial R_I} \tag{2.24}$$

Moreover, the minimum energy corresponds to zero force. The force is solely determined by the electron density, $n(r)$, and the nuclei.

2.2. Theory of Phonons

DFT offers a powerful framework not only for determining ground state properties but also for computing various excited state properties of materials. Analyzing phonon band dispersion spectra is particularly crucial for characterizing newly predicted materials, as it provides insights into their dynamic behavior and stability. Through DFT, nearly flawless vibrational spectra can be calculated, serving as valuable benchmarks for experimental validation and refinement of theoretical predictions. The Hellmann-Feynman theorem serves as a fundamental tool in phonon calculations within DFT, establishing a relationship between the derivatives of total energy and Hamiltonian through a simple parameter. Given that the ground state undergoes changes with the ionic motions, the

total energy of a structure can be viewed as a function of atomic positions. By selecting the partial coordinate of the nuclei as the parameter in the Hellmann-Feynman theorem, it becomes feasible to compute all the forces acting within the structure. The essential quantities such as the energy ($E = E_{tot}(R_i)$, force acting on a nucleus located at position (R_i), and the force constants ($C_{ij} = dF/dR_j$) can be expressed accordingly. The straightforward formulation outlined above also enables the calculation of various other properties, including dielectric constants, effective charges, electron-phonon interactions, Helmholtz free energy, internal energy, specific heat, and entropy of the materials, using the obtained vibrational features. The quantum mechanical portrayal of lattice vibrations is commonly known as a "phonon". The phonon band dispersion of a material is a plot that represents its vibrational characteristics over the Brillouin zone. The small displacement method (SDM) serves as a valuable tool for determining the frequencies of phonons at any arbitrary q-vector across the Brillouin zone. It treats the crystalline and molecular structures as a system of interconnected balls, allowing for straightforward calculations. The propagation of lattice vibration waves, triggered by initial disturbances applied to the atoms and facilitated by the electrons, illustrates the dynamic nature of atomic motion. The atomic vibrations of a crystal or molecule can be described by analyzing the potential energy term expanded around the places where the atoms are in equilibrium. The energy of the system can be accurately characterized using the harmonic approximation as long as the atoms remain in close proximity to their equilibrium locations. Specifically, atomic displacements generate restorative forces that restore the system to its equilibrium state, corresponding to the behavior governed by Hooke's law in simple harmonic motion:

$$F = -kx \tag{2.25}$$

where k denotes the spring constant, and x represents the distance between atoms and their equilibrium position. Within the framework of DFT, calculations are carried out at the absolute zero temperature (0 K). Consequently, the resulting solution inherently lacks any information regarding vibrations. However, as previously mentioned, when an atom is moved from its equilibrium position, it creates a force that tries to bring it back, which can be determined. This methodology is widely recognized as the small displacement method. The force constant matrix is derived by perturbing the location of an atom by a tiny increment within a sufficiently large supercell. The number of atoms moved depends on the symmetry of the system. The Hellman-Feynman forces are computed for each displacement, and a force matrix is then generated. The potential energy of a system can be mathematically described by using the harmonic approximation as follows:

$$U_{harm} = E_{ground} + \frac{1}{2} \sum_{ls\alpha, l't\beta} \phi_{ls\alpha, l't\beta} R_{ls\alpha} R_{l't\beta} \tag{2.26}$$

where E_{harm} denotes the total energy of the crystal at equilibrium positions, R_{ls} denotes the displacement of s atom in unit cell, *l*, α, and β are the direction of the displacement in cartesian coordinates, and $\phi_{ls\alpha,l't\beta}$ represents the force constant matrix. The force constant matrix, denoted as $F_{ls\alpha}$, emerges from the differentiation of the harmonic energy relation with respect to forces and displacements. It serves to establish the connection between the force acting on each atomic site and the displacements of neighboring sites, represented as $R_{l't\beta}$. The relationship can be mathematically described as follows:

$$F_{ls\alpha} = \frac{dU_{harm}}{dR_{ls\alpha}} = -\sum_{l't\beta} \phi_{ls\alpha, l't\beta} R_{l't\beta} \tag{2.27}$$

and the force constant matrix can be straightforwardly expressed as:

$$\phi_{ls\alpha, l't\beta} = \frac{d^2 U_{harm}}{dR_{ls\alpha} dR_{l't\beta}} \tag{2.28}$$

Force and displacements exhibit linear dependence on each other, provided that the atomic displacements remain sufficiently small.From a computational perspective, maintaining atomic displacements within the range of 0.01-0.04 Åleads to satisfactory outcomes. Consequently, determining the vibrational properties at each atomic site involves identifying the eigenvalues of the dynamical matrix, where the elements correspond to $F_{ls\alpha}$.

$$D = \frac{1}{\sqrt{m_s m_t}} \sum_{ls\alpha, l't\beta} \phi_{ls\alpha, l't\beta} R_{l't\beta e^{iq.T}} \tag{2.29}$$

The force constant matrix can be also utilized to determine the elements of the dynamical matrix for any q-vector in the Brillouin zone. To ensure accurate calculations, supercells are utilized with periodic boundary conditions. Choosing adequately large supercells is crucial in order to minimize the impact of forces near the boundary of the cell. Significantly, for numerous metals, the electron screening effect facilitates convergence even with smaller supercells. In the context of the SDM, the phonon frequencies of a material can be determined by generating the force constant matrix following the application of small displacements to the atoms within periodically repeating supercells. The total number of phonon branches in the phonon band dispersion is determined by the total degrees of freedom in the material, which is 3N for a system comprising N atoms in the primitive

cell. These phonon branches can be further classified into two categories: acoustic and optical. The initial 3 phonon branches, termed as acoustic phonon frequencies, correspond to collective movements of atoms with lower frequencies. They characterize the overall lattice dynamics and are associated with the translational motion of the entire crystal lattice. In contrast, the remaining (3N-3) branches, referred to as optical phonon branches, represent vibrations characterized by higher frequencies. The optical vibrations are often linked to specific atomic motions, such as stretching or bending of bonds within the crystal lattice (out-of-phase motions of atoms). They provide valuable insights into the local atomic interactions and structural properties of the material.

2.3. Raman Spectroscopy

Quantum mechanics has been crucial in understanding how electromagnetic radiation interacts with matter, giving rise to optical phenomena such as photon absorption, scattering, emission, reflection, and transmission. Classical wave theory faced challenges in describing certain light scattering phenomena, leading to the discovery of Raman scattering. Influenced by Einstein and Smoluchowski's light-quantum framework, C.V. Raman aimed to correlate a medium's scattering ability with its molecular structure. Adolf Smekal laid the theoretical groundwork for the Raman effect in 1923, and C.V. Raman along with K.S. Krishnan experimentally discovered it in 1928. This discovery revolutionized vibrational spectroscopy and molecular physics. Raman spectroscopy examines atomic vibrations within a material, facilitating the identification of its chemical structure, phase, and crystallinity. Its versatility is evident in various applications, such as chemical identification and quantification, characterization of molecular structures, analysis of bonding effects, identification of vibrational, rotational, and electronic transitions, crystallographic orientation analysis, detection of counterfeit drugs, and analysis of the chemical composition of historical documents.

In this technique, a monochromatic light beam emitted by a laser within the visible, near infrared, or near UV range (350-1000 nm) is directed onto a sample, interacting with the phonons (quantized vibrational modes) within the material. During this interaction, both elastic (Rayleigh) and inelastic (Raman) scattering are detected as seen in Fig. 2.6. If the change in momentum and energy are zero ($\Delta\vec{p} = 0, \Delta E = 0$), elastic scattered photons are detected. If the change in energy is not zero ($\Delta\vec{p} = 0, \Delta E \neq 0$), inelastic scattered photons are observed, forming the basis of Raman spectroscopy. According to quantum mechanics, when electromagnetic radiation interacts with a material, it becomes

excited and transitions to a short-lived virtual energy level. In Rayleigh scattering, the

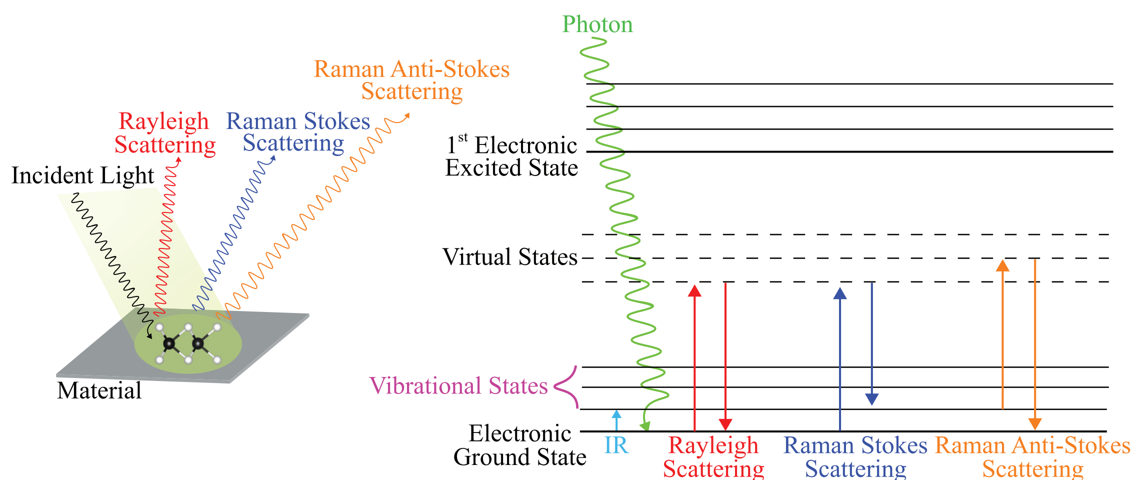

Figure 2.6. Illustration of three types of scattering process that can occur when light interacts with a material, and the energy level diagram shows the origin of Rayleigh, Stokes, and Anti-Stokes Raman scatter. The energy level diagram depicts the states involved in Raman spectroscopy.

molecule returns to its lowest energy state without losing energy due to the instability of the virtual state. This scattering is much more intense than Raman scattering, which occurs roughly once in every 10 million photons. In the Raman spectrum, Rayleigh intensities are observed at a frequency difference of zero since the scattered light matches the incident light's frequency. Raman scattering involves the material shifting to a higher energy state (Stokes Raman scattering) or a lower energy state (Anti-Stokes Raman scattering). Stokes scattering is generally more intense and is usually analyzed as it corresponds to positive energies in the Raman spectrum. The Raman shift provides information on the phonons of the examined material, typically ranging between 50 and 8000 cm^{-1} in wavenumber, reflecting the characteristic molecular vibrations of the sample. When a material encounters an electromagnetic wave, the wave's electric field interacts with the molecules' electric characteristics. Even materials lacking an electric dipole moment can develop induced dipole moments due to the wave's influence. This interaction creates or alters a dipole moment, leading to Raman bands formed by the oscillating induced dipole caused by the interaction between light waves and the polarizability of a vibrating molecule.

In order to determine the Raman activity of a vibrational modes, it is necessary to begin with a fundamental formulation of the intensity. The intensity of an output from a physical source can be defined as the ratio of the average power to the area over which the scattering rate is recorded. In Raman spectroscopy, this intensity is directly related to the amplitude of the scattered light, which is influenced by factors such as the number of

scattering centers and their polarizability. Thus, analyzing the intensity of Raman scattering provides valuable insights into the vibrational activity of molecules and materials under investigation. The intensity can be expressed as follows:

$$I = \frac{P}{A} \tag{2.30}$$

where P represents the mean power emitted by the source, while A represents the surface area. As previously described, in a Raman spectroscopy experiment, incoming light interacts with vibrating atoms in the sample, leading to inelastic scattering due to the Raman effect. According to classical electrodynamics, an oscillating dipole emits radiation with an average power denoted by P (measured in watts).

$$P = \frac{4\pi^3 \upsilon_0^4 |\mu|^2}{3\varepsilon_0 c^3} \tag{2.31}$$

Quantum mechanically, the intensity of a transition from state $|\upsilon > to < \upsilon^{'}|$ can be

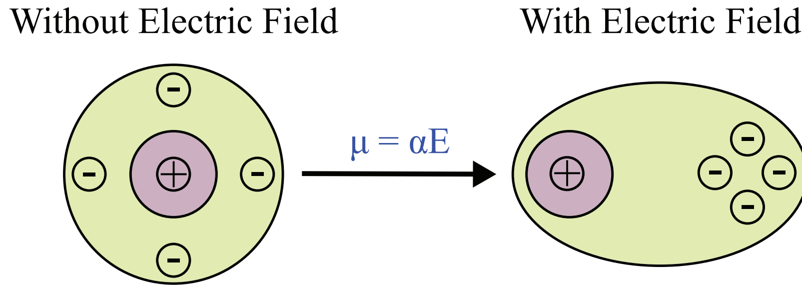

Figure 2.7. Induced dipole illustration under the influence of an electric field.

described as follows:

$$I = \frac{4\pi^3 \upsilon_0^4}{3A\varepsilon_0 c^3} < \upsilon^{'}|\mu^2|\upsilon > \tag{2.32}$$

here, υ_0 represents the frequency of the incident light, c is the velocity of light, and μ signifies the electric dipole moment of the oscillating dipole. The electric dipole moment is connected to the incident electric field through the given relationship:

$$\begin{aligned} \mu_{ind} &= \alpha E \\ \alpha &= \alpha_0 cos(2\pi\upsilon_0 t) \end{aligned} \tag{2.33}$$

here, the oscillating electric field E produces an induced dipole moment in the oscillating matter as shown in Fig. 2.7 and α represents its ability to polarize under the influence of an electric field. Polarizability is a fundamental physical property that describes how the

distribution of electrons within a molecule or atom responds to an external electric field. It indicates the extent to which the electron cloud surrounding the atom or molecule can be deformed by the electric field. Essentially, polarizability quantifies the susceptibility of this temporary charge distribution, determining its strength and configuration. Additionally, polarizability is affected by variations in bond length; for example, when the bond length increases, the polarizability also tends to increase. In addition, from a classical perspective, light can be defined as a transverse wave consisting of an oscillating electromagnetic field that is perpendicular to the direction of wave propagation. The magnitude of the oscillating electric field for a light wave with vibrational frequency of a molecule or atom υ_0 is given by:

$$E = E_0 cos(2\pi\upsilon_0) \tag{2.34}$$

where E_0 denotes the amplitude of the oscillating electric field. As the molecule or a atom undergoes continual rotational and vibrational movements, its electronic distribution undergoes constant fluctuations. Therefore, in order to describe the motion of individual atoms in a vibrational mode of a material, the polarizability, α, should be expanded into a Taylor series in terms of the normal mode (Q_k) of the nuclear displacements. If $Q_k = r - r_0$, the polarizability is expressed up to first order term as follows:

$$\alpha = \alpha_0 + \left(\frac{\partial\alpha}{\partial Q_k}\right)_0 Q_k \tag{2.35}$$

where α_0 denotes the polarizability of the molecule at its equilibrium position ($Q_k = 0$) and the Q_k represents the normal mode (vibrational coordinate) that describes the collective movement of individual atoms involved in the kth vibrational mode. For polyatomic molecules, Q_k is 3N-6, and for linear molecules, it is 3N-5. Given that the motion of the atoms in the vibrational mode is being analyzed using the harmonic approximation, where all atoms are assumed to behave as harmonic oscillators, the solution for the normal mode Q_k can be expressed as:

$$Q_k = Q_0 cos(2\pi\upsilon_k) \tag{2.36}$$

here υ_k represents the frequency of the kth normal mode. The induced electric dipole can be characterized by three scattering terms.

By utilizing the E and α, μ can expressed as follows:

$$\mu = \alpha_0 E_0 cos(2\pi\upsilon_0 + E_0 Q_0 \left(\frac{\partial\alpha}{\partial Q_k}\right)_0 \{cos[2\pi(\upsilon_0 - \upsilon_k)] + cos[2\pi(\upsilon_0 + \upsilon_k)]\} \tag{2.37}$$

where $cos(2\pi\upsilon_0)$ denotes the elastic or Rayleigh scattering term, corresponding to the unshifted frequency of the incident light, resulting in elastic dispersion. $cos[2\pi(\upsilon_0 - \upsilon_k)]$ represents the Stokes Raman scattering term and last term is the Anti-Stokes Raman scattering term containing $cos[2\pi(\upsilon_0 + \upsilon_k)]$. As apparent from the relationship, the dipole moment fluctuates not only with the oscillation of the molecule but also in accordance with the frequency of the electromagnetic wave. These processes collectively lead to the phenomenon known as Raman scattering, which involves a net energy transfer between the incident light and the system. However, since the analysis of the Raman spectrum relies on experimental data obtained from the Stokes Raman intensity, we will focus solely on this term in our simulations. By employing the Stokes Raman scattering term of the induced dipole moment, we can calculate its intensity as follows:

$$I_{SR} = \frac{4\pi^3 \upsilon_0^4 E_0^2}{3A\varepsilon_0 c^3} < \upsilon^{'} | \left(\frac{\partial \alpha}{\partial Q_k} \right)_0^2 cos^2[2\pi(\upsilon_0 - \upsilon_k) Q_0^2] | \upsilon > \tag{2.38}$$

After expressing $I_0 = 1/2 E_0^2 \varepsilon_0 c$ as the intensity of the incident light, and taking the time average of the cosine term (which equals 1/2), we obtain the Stokes Raman scattering intensity as follows:

$$I_{SR} = \frac{4\pi^3 \upsilon_0^4 E_0^2}{3A\varepsilon_0 c^3} | < \upsilon^{'} | \left(\frac{\partial \alpha}{\partial Q_k} \right)_0 | \upsilon > |^2 \tag{2.39}$$

here, the initial and final states can be conceptualized of as the polarization vectors of the incident light and scattered radiation. The intensity of Stokes Raman scattering is directly proportional to the rate of change in polarizability in relation to the normal mode of a vibration. This term is referred to as the Raman activity, which is expressed as $| < \upsilon^{'} | \left(\frac{\partial \alpha}{\partial Q_k} \right)_0 | \upsilon > |^2$ and the term $\left(\frac{\partial \alpha}{\partial Q_k} \right)_0$ is a 3×3 Raman tensor for the kth vibrational mode, written by:

$$R = \begin{bmatrix} \frac{\partial \alpha_{11}}{\partial Q_k} & \frac{\partial \alpha_{12}}{\partial Q_k} & \frac{\partial \alpha_{13}}{\partial Q_k} \\ \frac{\partial \alpha_{21}}{\partial Q_k} & \frac{\partial \alpha_{22}}{\partial Q_k} & \frac{\partial \alpha_{23}}{\partial Q_k} \\ \frac{\theta \alpha_{31}}{\partial Q_k} & \frac{\theta \alpha_{32}}{\partial Q_k} & \frac{\partial \alpha_{33}}{\partial Q_k} \end{bmatrix} \tag{2.40}$$

Since the Raman tensor includes the alteration of the polarizability with respect to the normal mode, it is a vibrational mode-dependent feature. Generally, it can be mathematically represented using group theory for every vibrational mode. Direct calculation of the polarizability or its variation with respect to the normal mode is not feasible utilizing the VASP in our DFT computation approach. Alternatively, we can compute the dielectric tensor for the material, and calculate how it changes in response to vibrations using

the VASP program. Therefore, the alteration in the dielectric tensor can be linked to the change in polarizability using the following equation:

$$\frac{\partial \alpha_{ij}}{\partial Q_k} = \left(\frac{V}{4\pi}\right) \frac{\partial \varepsilon_{ij}}{\partial Q_k} \tag{2.41}$$

To qualify for a vibrational mode to be considered Raman active, the Raman tensor must be a non-zero tensor, resulting in a non-zero intensity. In addition, if the Raman tensor for a vibrational mode is not zero, the direction-dependent activity of the mode can be determined by modifying the experimental system. Alterations in the polarization state

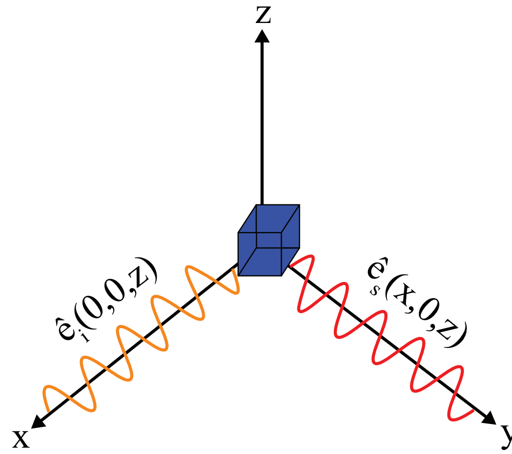

Figure 2.8. An illustrative configuration for the Raman scattering process. The symbols $\hat{e}_i$ and $\hat{e}_s$ denote the polarization vectors of the incident and the scattered light, respectively.

of the incoming light impact the characteristics and informational aspects of the scattered radiation. However, this applies only to the expression $\hat{e}_s \left(\frac{\partial \alpha}{\partial Q_k}\right) \hat{e}_i$, where $\hat{e}_s$ and $\hat{e}_i$ represent the polarization vectors of the scattered radiation and incident light, respectively. When employing the braket notation, it represents the process of averaging over all angles of orientation of the sample in relation to the experimental framework. Therefore, the Raman activity term can be represented using Raman constants, which are unaffected by the experimental configuration. Angular averaging is necessary to determine the intensity of Raman scattering, especially in systems with randomly oriented molecules. Assuming that the incident light is polarized in the z-direction and propagating along the z-axis, as illustrated in Fig. 2.8. The scattered radiation is detected along the y-direction and may be polarized in the x- and z-directions, as indicated by the relationship provided in following formulas:

$$\begin{aligned} \mu_z &= \alpha_{zz} E_{0z} \\ \mu_x &= \alpha_{xz} E_{0z} \end{aligned} \tag{2.42}$$

Therefore, two prospective terms will manifest as the scattered intensity: $<\tilde{\alpha}_{zz}^2>$ and $<\tilde{\alpha}_{xz}^2>$. The symbol $\tilde{\alpha}$ represents the derivative of the polarizability with regard to the normal mode (Q_k). The presence of these two terms indicates that their combination enables the computation of either the overall intensity of the scattered radiation or the individual intensities aligned with and perpendicular to the incoming light. The final average for these terms will be expressed in relation to the Raman invariants.

$$\begin{aligned}\tilde{\alpha}_s &\equiv \frac{1}{3}(\tilde{\alpha}_{xx} + \tilde{\alpha}_{yy} + \tilde{\alpha}_{zz}) \\ \beta &\equiv \frac{1}{2}\{(\tilde{\alpha}_{xx} - \tilde{\alpha}_{yy})^2 + (\tilde{\alpha}_{yy} - \tilde{\alpha}_{zz})^2 + (\tilde{\alpha}_{zz} - \tilde{\alpha}_{xx})^2 \\ &+ 6[(\tilde{\alpha}_{xy})^2 + (\tilde{\alpha}_{yz})^2 + (\tilde{\alpha}_{xz})^2]\}\end{aligned} \tag{2.43}$$

The terms $\tilde{\alpha}_s$ and β denote the components of the polarizability tensor that correspond to isotropic and anisotropic derivatives, respectively. Expressing the intensity using these two variables is crucial because they remain unchanged regardless of alterations in the sample orientation. Therefore, employing these identities enables us to describe the scattered intensity consistently across different experimental setups. Ultimately, by employing isotropic and anisotropic polarizability derivative tensors, the Raman activity can be formulated as:

$$R_A = 45\tilde{\alpha}^2 + 7\beta^2 \tag{2.44}$$

Upon conducting a comprehensive mathematical analysis, it becomes evident that while the experimental setup depicted in Fig. 2.8 may vary, the total averaged Raman activity remains constant. However, the only parameter that changes when modifying the experimental setup is the proportion of perpendicular Raman activity to parallel Raman activity, commonly referred to as the depolarization ratio, as expressed below:

$$\rho = \frac{I_{\perp}}{I_{\parallel}} \tag{2.45}$$

The total intensity of Raman scattering in the two main polarization orientations (perpendicular and parallel) remains constant when the sample under experimental investigation is averaged for orientation, thus ensuring consistency across different experimental setups.

2.4. Mechanical Properties of Materials

The mechanical characteristics of materials are highly significant and key properties that must be thoroughly investigated to facilitate the proper integration of that material into emerging technologies across a wide range of applications, from the construction of buildings and bridges to the development of advanced technologies. These properties provide crucial insights into how materials respond to external forces and strains, ultimately determining their structural integrity and performance under different conditions. The mechanical characteristics of a material are intricately linked to the interatomic forces within the material, which resist structural changes and determine its behavior. Experimental investigations into mechanical characteristics involve testing their response to applied forces per unit area (stress), and the resulting deformation per unit length (strain). Particularly within experimental environments, materials may experience strain or deformation. Understanding the mechanical features of materials allow us to tailor materials to meet specific requirements, such as strength, flexibility, and durability. These features not only elucidates the behavior of material under various conditions but also informs the design and development of robust materials for diverse applications. Furthermore, mechanical properties encompass a range of characteristics, each serving a distinct purpose. For instance, hardness refers to a material's resistance to scratching, while ductility describes its capacity to undergo plastic deformation without fracturing. Meanwhile, toughness is associated with a material's ability to absorb energy before fracturing. Additionally, it is crucial that the strain energy of a given crystal remains consistently positive for all possible values of applied external strain. Otherwise, the crystal structure would indicate mechanical instability within the crystal. The quadratic form ($1/2C_{ij}e_ie_j$) of the strain energy is positive definite for all real values of strains unless all the strains are zero. The positivity of the energy imposes further restrictions on the elastic constants, C_{ij}, depending on the crystal structure. Elastic constants characterize the ability of a material to deform under small stresses and then returning to its original shape after stress ceases.

2.4.1. Elastic Constants

Elastic constants are fundamental physical characteristics that define the elastic behavior of materials. They provide insights into how materials respond to applied stress and deformation. The elastic constants constants are derived by analyzing the correlation

between the stress exerted on a material and the resulting strain, offering crucial insights about the material's mechanical properties and its capacity to withstand external forces while maintaining its original shape. The tension test stands as one of the primary methods for evaluating a material's mechanical response to applied stress. It plays a crucial role in predicting and analyzing the behavior of materials under various loading conditions. By subjecting a material to tension, key properties of a material such as strength, ductility, and mechanical characteristics, including elastic constants like Young's modulus, Poisson's ratio, and bulk modulus, can be evaluated. Elastic constants are determined by analyzing stress-strain measurements obtained within the material's linear elastic range. When a material is subjected to loading within this elastic region, it retains the ability to completely restore its original shape once the applied load is removed, highlighting the reversible nature of its deformation process. The elastic properties of materials play a crucial role in laying the groundwork for innovative solutions in future engineering applications. When a material is subjected to tensile stress, a linear relationship emerges between the applied loads and the resulting stress and strain, particularly noticeable for low values of the applied loads. The region of low load, exhibited by metals and fragile materials, is referred to as the elastic region. However, for ductile materials like rubber, the stress-strain relation may not display linear behavior, or it may exist only for extremely small applied loads. Despite these differences, most materials display elastic behavior, with stress and strain related linearly through Hooke's Law, which serves as the foundation for understanding the linear relationship between stress and strain in elastic materials.

2.4.1.1. Young Modulus

The concept of Young's modulus was initially proposed by Thomas Young and subsequently named in his honor. Young's modulus, commonly referred to as the modulus of elasticity, is a fundamental mechanical property that provides insight into the inherent tensile or compressive stiffness of a material, especially along its axial direction or its resistance to elastic deformation. It serves as a quantitative measure, expressing the relationship between the stress applied to the material and the resulting strain experienced along this particular axis. On the atomic scale, the elastic modulus refers to the minor changes in interatomic spacing and the stretching of interatomic bonds that can be considered as strain. Following that, the modulus of elasticity quantifies the material's ability to withstand the separation of neighboring atoms. The values of the Young Modu-

lus varies among different material due to the different types of atomic bonding character in materials. Young's modulus (E) is mathematically defined as the ratio of the stress (σ) applied to a material to the resulting strain (ε. By quantifying the amount of deformation a material undergoes in response to applied forces, Young's modulus plays an essential role in comprehending and predicting the mechanical behavior of materials, thereby facilitating their appropriate utilization in various engineering and structural applications. The relationship between the applied load (stress) and strain in the elastic region can be described by:

$$\sigma = E\varepsilon \tag{2.46}$$

where σ represents the applied load, ε denotes the change in the dimension of the material along the direction of the applied load, and E represents the constant of proportionality, referred to as 'Young's Modulus' of a material. Young's modulus is a constant, known as the modulus of elasticity, which can take on various forms depending on the direction and nature of the applied load. In the SI unit system, its unit is gigapascals (GPa), and the slope of a linear segment of the stress-strain relation corresponds to E.

2.4.1.2. Poisson Ratio

The Poisson ratio is a significant elastic constant that characterizes how a material responds to an applied load in directions perpendicular to the unloaded directions. It defined as the lateral strain to longitudinal strain ratio, offers valuable information into a material's behavior under stress. The Poisson ratio was introduced by the French physicist and mathematician Simeon Poisson in the early 19th century. It refers to the negative ratio of the lateral strain ($\varepsilon_{lateral}$) to the longitudinal strain (ε_{axial}). The Posisson ratio is a dimensionless parameter that indicates the degree of lateral contraction or expansion relative to longitudinal deformation when a material is under stress, and it can be expressed as follows:

$$\upsilon = -\frac{\varepsilon_{lateral}}{\varepsilon_{long.}} \tag{2.47}$$

The strains along unloaded directions typically exhibit opposite signs compared to the loaded direction in most crystal structures. Hence, including the minus sign in the formula ensures a positive value for the Poisson ratio. In general, when subjected to uniaxial stretching, the most of the crystal tend to narrow. The primary factor is that the majority of crystals exhibit greater resistance to changes in volume, a natural consequence of their bulk modulus, compared to their resistance to changes in shape, influenced by their shear

modulus. The positive Poisson ratio is a result of the reorientation of interatomic bonds that occurs during deformation. Most of the crystal structure exhibit a Poisson ratio value ranging from 0 to 0.5 indicates that when a material undergoes axial tensile strain, it will contract laterally. Conversely, when the material experiences compressive strain, it will expand laterally. However, it is worth noting that although the majority of materials have a Poisson ratio that is positive, there are specific materials, whether they arise naturally or are hand-made, that demonstrate a negative Poisson ratio ranging between -1 and 0. Unlike materials with positive Poisson ratios, those with negative Poisson ratios tend to elongate in one direction when stretched along perpendicular directions which are known as auxetic materials. Compared to materials with positive Poisson ratios, auxetic materials can exhibit superior physical properties. The Poisson ratios of materials are determined by their atomic or molecular geometries. Metals exhibit a highly ordered structure, leading to Poisson ratios typically around 0.3 whereas polymers, with their non-uniform structures, tend to have ratios closer to 0.5. Moreover, materials exhibiting a greater Poisson ratio tend to possess greater ductility, while materials with a lower ratio tend to be more brittle. Understanding the Poisson ratio is essential for evaluating the shrinkage and expansion properties of materials under applied stress. It helps determine the compressive or tensile strains along unloaded directions when the material experiences uniaxial stretching or compression, which is crucial for various engineering applications.

2.4.2. Elastic Constants in 2D Limit

In previous sections, we introduced the definitions of two fundamental elastic properties, namely Young's modulus and Poisson's ratio, for materials in bulk form. However, it is necessary to revise those elastic constants when analyzing 2D materials due to dimensional reduction and confinement in the 2D limit. While there has been notable advancement in experimental investigations into the mechanical properties of 2D materials, conducting experimental study on the fundamental mechanical properties of ultrathin 2D materials remains difficult. Hence, theoretical calculations emerge as highly efficient tools for predicting the mechanical behaviors of such structures. In addition, due to their atom-scale thickness, 2D materials exhibit predominantly in-plane characteristics. In order to apply the principles of mechanical parameters from 3D systems to 2D systems, all the parameters from the 3D systems are adjusted by dividing them by the thicknesses of the 2D materials. This section presents a concise explanation of two fundamental elastic constants and describes our methodology for computing them at the atomic level.

2.4.2.1. In-plane Stiffness

The in-plane stiffness serves as a quantitative measure of a material's rigidity or flexibility. It is determined by the geometry of the structure and the strength of the atomic bonds between the individual atoms under consideration. In the framework of the 2D limit, the modulus of elasticity is referred to as in-plane stiffness, C. In the case of two-dimensional systems, it is important to note that materials lack periodic boundary conditions in the direction perpendicular to the plane (out-of-plane). As a result, the modulus of elasticity, which represents the stiffness within the plane, is directly influenced by the stress and strain experienced within the plane. Therefore, the σ should be reformulated in the form of condition as:

$$\begin{aligned} \sigma_{xx} &= C_{xx}\varepsilon_{xx} \\ \sigma_{yy} &= C_{yy}\varepsilon_{yy} \end{aligned} \tag{2.48}$$

The directions xx and yy represent certain orientations inside the 2D crystal structure. Within a hexagonal crystal symmetry, the xx and yy directions are often referred to as the zigzag (ZZ) and armchair (AC) orientations. Isotropic materials exhibit identical stiffness in all directions due to the crystal symmetry of their interatomic bonding within the structure. On the other hand, anisotropic materials demonstrate varying stiffness values depending on their orientation relative to the crystal structure. Direction-dependency implies that a material's ability to withstand external forces will not be consistent in all directions, which can be beneficial when utilizing the material in nanoscale applications. The determination of in-plane stiffness in the atomic level can be achieved by relating the strain energy to the applied strain. Strain energy in a material is the alteration in the overall energy of the crystal due to the application of strain. The strain energy must adhere to the following expression as the elastic constants are evaluated within the linear elastic range:

$$E_S = c_1\varepsilon_{xx}^2 + c_2\varepsilon_{yy}^2 + c_3\varepsilon_{xy}^2 \tag{2.49}$$

here, E_S represents the strain energy, which is the overall energy variation between deformed and unstrained configurations. After calculating the coefficients c_i, the in-plane stiffness along any specific direction can be determined using the following formula:

$$\begin{aligned} C_x &= \frac{1}{A_0}\left(2c_2 - \frac{c_3^2}{2c_1}\right) \\ C_y &= \frac{1}{A_0}\left(2c_1 - \frac{c_3^2}{2c_2}\right) \end{aligned} \tag{2.50}$$

where A_0 represents the area of the structure that is not subject to strain.

The in-plane stiffness can be determined by utilizing the elastic parameters obtained through the calculation of the elasticity tensor. As previously mentioned, in-plane stiffness refers to the correlation between stress and strain within the linear elastic range. The elasticity tensor, which establishes the relationship between the applied load (stress) and the strain tensor, has a dimension of 6×6 and is defined by the provided form:

$$\begin{bmatrix} C_{1111} & C_{1122} & C_{1133} & C_{1123} & C_{1131} & C_{1112} \\ C_{2211} & C_{2222} & C_{2233} & C_{2223} & C_{2231} & C_{2212} \\ C_{3311} & C_{3322} & C_{3333} & C_{3323} & C_{3331} & C_{3312} \\ C_{2311} & C_{2322} & C_{2333} & C_{2323} & C_{2331} & C_{2312} \\ C_{3111} & C_{3122} & C_{3133} & C_{3123} & C_{3131} & C_{3112} \\ C_{1211} & C_{1222} & C_{1233} & C_{1223} & C_{1231} & C_{1212} \end{bmatrix}$$

The elastic constants, denoted as C_{ijkl}, exhibit certain symmetry characteristics, namely C_{ijkl} = C_{jikl}, C_{ijkl} = C_{ijlk}, and C_{ijkl} = C_{klij}. By considering all the symmetry aspects of the structure, the number of independent constants in this 36-element tensor is reduced to 21. However, the number 21 signifies the highest possible quantity of independent components. The range of the crystal structure's symmetry may differ from 3 to 21, depending on its configuration. The expression for the elasticity tensor of isotropic materials is given by Voight notation as follows due to symmetry of the crystal:

$$\begin{bmatrix} C_{11} & C_{12} & C_{12} & 0 & 0 & 0 \\ C_{12} & C_{11} & C_{12} & 0 & 0 & 0 \\ C_{12} & C_{12} & C_{11} & 0 & 0 & 0 \\ 0 & 0 & 0 & C_{33} & 0 & 0 \\ 0 & 0 & 0 & 0 & C_{33} & 0 \\ 0 & 0 & 0 & 0 & 0 & C_{33} \end{bmatrix}$$

The relationship between C_{33} and C_{11} and C_{12} can be expressed by the equation: $C_{33} = (C_{11} - C_{12})/2$. The Voight notation enables the establishment of relationships between mechanical constants by means of these elastic constants. When the tensor elements C_{ij} are known, the Young modulus and Poisson ratio can be interconnected using the following formula:

$$C_{11} = \frac{E(1-\upsilon)}{(1+\upsilon)(1-2\upsilon)}$$
$$C_{12} = \frac{E\upsilon}{(1+\upsilon)(1-2\upsilon)} \quad (2.51)$$

here, E denotes the Young modulus or modulus of elasticity, while υ denotes the Poisson ratio. The relationship between the three-dimensional modulus of elasticity, E, and its two-dimensional equivalent, C, can be established by taking into account the effective thickness of a single-layer material in two dimensional form. The effective thickness, denoted as h_e, is often defined as the sum of the actual thickness of the layer and the spacing between layers in its bulk form. The relationship between the in-plane stiffness (C) and Young modulus (E) is expressed by the following expression:

$$C = Eh_e \quad (2.52)$$

By utilizing the relationships between C-E and E-υ, we can rewrite the expressions in terms of elastic constants, C_{ij}, as follows:

$$C = h_e C_{11}[1 - \left(\frac{C_{11}}{C_{12}}\right)^2] \quad (2.53)$$

The elasticity tensor can be obtained as an outcome of DFT-based first-principles simulations and it is feasible to compute the in-plane stiffness of a material using two distinct approaches, outlined here.

Similar to the calculation of the elasticity tensor components, Poisson's ratio can also be determined using the elastic constants obtained from the elasticity tensor. The Poisson ratio can be calculated from the components Cij using the following equation:

$$\upsilon = \frac{C_{12}}{C_{11}} \quad (2.54)$$

When analyzing anisotropic crystal structures, the elastic constant described above can be modified to determine the Poisson ratio of the material, which varies depending on the direction. By substituting C_{22} into the above equation, one can determine the Poisson ratio in direction-2, and so forth. So far, the elastic mechanical constants have been established and an overview of the calculation methodologies using DFT-based computations has been provided. In the following part will provide further clarification on additional mechanical qualities, such as yield stress, ultimate strength, fracture behavior, elastic and plastic region of structures by outlining the stress-strain relationship curve and discussing

its implications for material behavior.

2.5. Computational Parameters

This section introduces the general computational framework utilized to analyze the materials discussed in subsequent sections. In this thesis, in order to investigate the structural, magnetic, vibrational, electronic, and elastic properties of ultra-thin low dimensional materials, first-principles calculations were carried out by conducting spin-polarized calculations within Density Functional Theory as implemented in the Vienna ab-initio Simulation Package (VASP).[168] The VASP code employs an iterative approach to solve the Kohn-Sham equations for a material with periodic boundary conditions, utilizing a plane-wave basis set calculates an approximate solution to the many-body Schrödinger equation of the structure. The plane-wave projector-augmented wave (PAW) method was employed to portray the potentials of individual atoms within the all structures. The Perdew-Burke-Ernzerhof (PBE) form[169] of the generalized gradient approximation (GGA) was adopted to describe the exchange-correlation effects on electrons. In addition, the hybrid DFT-HSE06 functional[170] was implemented to provide a more precise calculation of the band gap of materials, since bare-GGA tends to underestimate the band gap of semiconducting materials. The electronic band dispersion calculations incorporated spin-orbit interactions, which are crucial effects for certain materials, particularly those with larger atomic radius. The DFT-D2 method by Grimme[171] was employed to consider the weak van der Waals forces between individual atoms within the structures, particularly crucial for layered materials. The Dudarev's DFT+U method was employed to address the limitations of the GGA functional in accurately describing strongly correlated systems with partially filled d subshells, particularly accounting for significant correlations between the Hf, Ti, Ta, and Mn-d orbitals. This method combines the on-site local Coulomb parameter, U, and the exchange parameter, J, into a single parameter, namely $U_{eff} = U - J$. The optimized U_{eff} parameter was taken to be 4.0, 5.8, 3.06, and 5.0 eV for $HfTe_5$, TiX_3, TaX_3 (X=S, Se, and Te), and $MnPS_3$ structures in all calculations. The Bader methodology was employed in order to ascertain the charge distribution on the structures and the analysis of charge transfer occurring within the structures.[172] Structural optimizations were carried out using the parameters provided below. The energy threshold of the plane-wave basis set was set at 500 eV for all calculations. To achieve minimum total energy, the energy difference between each sequential step was adjusted to 10^{-5} eV and the convergence threshold for the total Hellmann-Feynman forces within the unit cell

was set to 0.05 eV/Å. Additionally, to ensure accurate calculations and broadening of the density of states (DOS), a Gaussian smearing width of 0.05 eV was employed, and the pressure on the unit cell was reduced to below 1.0 kilobar along all three directions. In order to accurately determine charge densities, Brillouin Zone integration was performed utilizing dense Γ-centered k-point samplings. To avoid potential interactions between repeating layers of ultra-thin single-layer structures along the out-of-plane direction, a sufficiently large vacuum gap was taken into account.

In order to investigate the dynamical stability, vibrational characteristics were calculated for a large supercell of the structures under consideration using the small displacement methodology, as implemented in the VASP, with PHON code.[173] The total energy convergence criterion was tightened to 10^{-8} eV in order to study the dynamical matrix in calculations of phonon band dispersions. Each atom in the primitive unit cell was initially distorted by 0.01 Å and the corresponding dynamical matrix was constructed. Then the vibrational modes were obtained by a direct diagonalization of the dynamical matrix. Moreover, the vibrational properties of the structures were investigated in terms of the off-resonant zone-centered Raman activity of each phonon modes at Γ point. For this purpose, firstly, the vibrational phonon modes were computed using the small displacement methodology as implemented in VASP. Then the derivative of macroscopic dielectric tensor with respect to the each normal mode was calculated and the corresponding Raman activities were obtained. In addition to the dynamical stability, thermal stabilities were investigated by performing the ab-initio Quantum Molecular Dynamics (QMD) simulations at finite temperatures. The simulations were carried out at room temperature (300 K) using the Nosé-Hoover thermostat to control the temperature, employing a time step of 2 femtoseconds (fs) for integration. In order to investigate the mechanical stability of the considered structures, the elastic stiffness tensors were calculated and Poisson ratios and stiffness values of the structures are obtained. Furthermore, to investigate the chemical stabilities, the cohesive energies of structures under consideration were calculated using the following equation: $E_{coh} = (\frac{1}{\sum\limits_i n_i}(\sum\limits_i n_i E_i) - E_T)$, where i represents the atoms composing the structure; n_i, E_i, and E_T denotes the number of i atom in the unit cell, the energy of single i atom, and the total energy per unit cell, respectively. Using the local potential distribution along out-of-plane direction, the work functions are calculated by following formula: $\phi = E_{vac} - E_F$, where ϕ denotes the work functions, E_{vac} is the vacuum energy, and E_F represents the Fermi energy.

CHAPTER 3

NOVEL HIGHLY ANISOTROPIC SINGLE-LAYER TRANSITION METAL PENTACHALCOGENIDES

In this chapter, the structural, vibrational, electronic, optical, and elastic properties of single-layer $HfTe_5$ and its defected structures were investigated by means of ab initio calculations. It was found that free-standing $HfTe_5$ is dynamically and mechanically stable indirect band gap semiconductor possessing in-plane anisotropy. In addition, several point defects and their oxidized structures were shown to be distinguishable by means of the STM simulations. The rest of chapter is organized as follows; the structural, vibrational, thermal, electronic, optical, and elastic properties of $HfTe_5$ are presented in Section 3.1. Additionally, identification of point defects and their oxidized structures in single-layer $HfTe_5$ are given in this section. In the Section 3.2, structural, vibrational, electronic and elastic features of titanium pentachalcogenides (TiX_5, X=S, Se, and Te) are presented.

Table 3.1. For the single-layer $HfTe_5$; the optimized in-plane lattice parameters, *a and c*; the atomic bond lengths between individual atoms, $d_{Hf-Te_{ch}}$, $d_{Hf-Te_{out}}$, $d_{Te_{out}-Te_{out}}$, $d_{Te_{ch}-Te_{in}}$; vertical distance between uppermost and lowermost Te atoms (thickness), t; the cohesive energy per atom, E_{coh}; the work function, Φ; and electronic band gap energy E_g^{SOC}.

	a (Å)	c (Å)	$d_{Hf-Te_{ch}}$ (Å)	$d_{Hf-Te_{out}}$ (Å)	$d_{Te_{out}-Te_{out}}$ (Å)	$d_{Te_{ch}-Te_{in}}$ (Å)	t (Å)	E_{coh} (eV/atom)	Φ (eV)	$E_g^{HSE+SOC}$ (eV)
$HfTe_5$	3.99	13.88	3.02	2.99	2.80	3.35	5.37	1.740	4.36	0.158

3.1. Hafnium Pentatelluride

The optimized atomic structure of single-layer $HfTe_5$ is illustrated in Fig. 3.1(a) from top and side views. The crystal structure of $HfTe_5$ is made up of two Hf-Te_5 units, which are oppositely orientated along the out-of-plane direction, are connected together through Te atoms, giving rise to orthorhombic symmetry. Within the primitive unit cell of single-layer $HfTe_5$, there exist three type of Te atoms, namely the outer (Te_{out}), inner (Te_{in}), and the chain (Te_{ch}) atoms as shown in Fig. 3.1(a). Note that the two Hf-Te_5 units are connected through the Te_{ch} atoms. The optimized in-plane lattice parameters, a

and c, are found to be 3.99 and 13.88 Å, respectively, indicating the in-plane anisotropy of $HfTe_5$. Note that the vacuum is inserted along the b lattice vector. The direction a is defined to be parallel to Hf-chains ($Hf_{ch}^{\parallel}$) while c is defined to be perpendicular to Hf-chains ($Hf_{ch}^{\perp}$). The structural parameters were reported from the experimental observations for the bulk structure are a = 3.97 Å, b = 14.49 Å, and c = 13.72 Å.[174] Apparently, as the $HfTe_5$ is dimensionally reduced from bulk to single-layer, it expands along a direction ($Hf_{ch}^{\parallel}$), while it shrinks along the c direction ($Hf_{ch}^{\perp}$). The corresponding Hf-Te bond lengths are found to be 3.02 Å for Hf-Te_{ch} while that of Hf-Te_{out} is calculated to be slightly shorter (2.99 Å). In addition, the outer Te atoms are found to form Te-dimers with the corresponding Te-Te bond length of 2.79 Å and the one formed between Te_{ch} atoms is 2.92 Å. Moreover, the vertical distance between the outermost Te atoms, which is defined as the thickness of single-layer $HfTe_5$, is found to be 5.37 Å (see Table 3.1). Bader charge analysis reveals that upon forming single-layer $HfTe_5$, charge

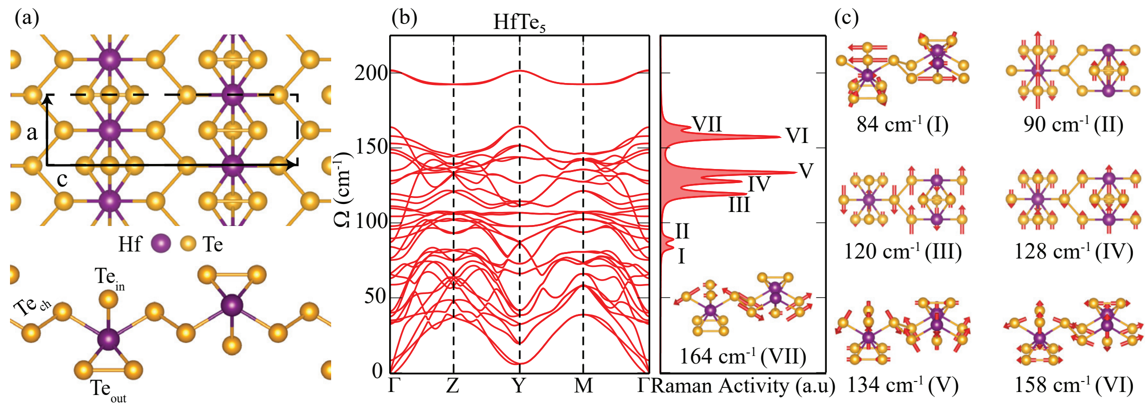

Figure 3.1. For the single-layer $HfTe_5$ structures, (a) top and side views of the structure. (b) The phonon band dispersions (left panel) with the corresponding Raman spectrum (right panel) and (c) atomic vibrations of each Raman-active phonon mode.

donation occurs from Hf atom to Te atoms such that each Hf donates 1.7 e^- to the surrounding five Te atoms. The amount of 0.6, 0.5, and 0.1 e^- are received by the Te_{in}, Te_{out}, and Te_{ch}, respectively. Bader analysis indicates the partially ionic bonding character between Hf and Te atoms. The well-known anisotropic single-layer black phosphorus (BP) was reported the consist of phosphorus atoms connected through covalent bonds.[175] Similarly, single-layer magnetic CrI_3 structure was shown to display strongly covalent character between the Cr and I atoms.[176] As compared to anisotropic BP and magnetic CrI_3, single-layer $HfTe_5$ structure may be more resistive to oxidation due to its partially ionic nature. Using the local potential distribution along the out-of-plane direction shown in Fig. 3.2(a), the work function is calculated using the formula: $\Phi = E_{vac} - E_F$. Work

function (Φ), which is defined as the amount of energy required to remove a charge carrier (electron/hole) located at the Fermi energy to vacuum as a free particle. In order to compare the work function of $HfTe_5$ with that of Hf-based single layers, the work function for various Hf-based structures are calculated and shown in Fig. 3.2(b). It is

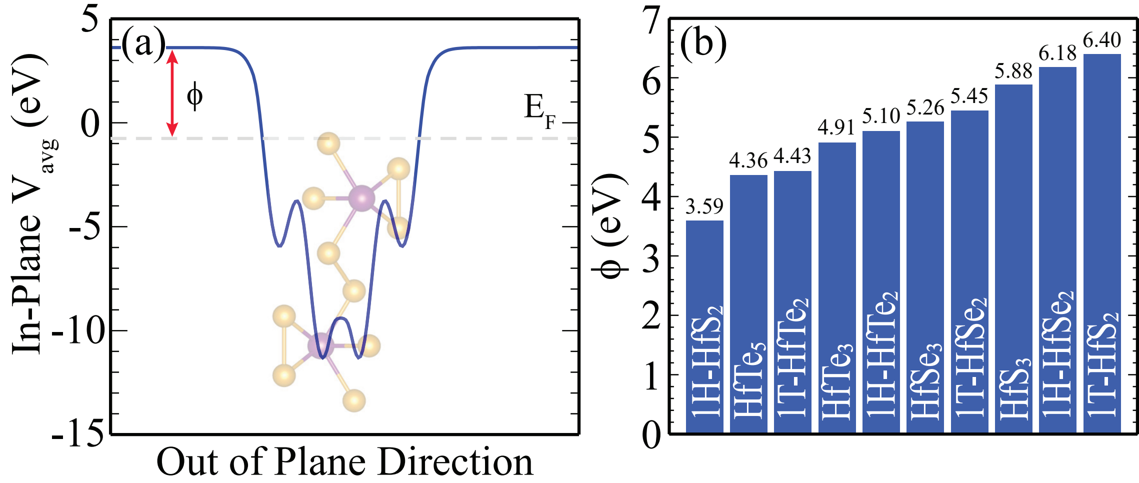

Figure 3.2. (a) Local potential profile of $HfTe_5$ plane averaged along the out-of-plane direction and (b) work functions of Hf-based single-layer structures. The Fermi energy (E_F) and the work function (Φ) are ilustrated as insets in (a).

seen that $HfTe_5$ has the second lowest work function (4.36 eV) among different phases of Hf-based single layers. In order to analyze the strength of the binding between the atoms, the cohesive energy E_{coh} of the $HfTe_5$ structure is calculated using the following formula: $E_{coh} = mE_{Hf} + nE_{Te} - E_{HfTe_5}/(m+n)$, where m and n stand for the number of Hf and Te atoms, respectively, in a unit cell. E_{Hf} and E_{Te} are the single atom energies of Hf and Te, respectively. Cohesive energy provides the information about energy required to separate individual atoms in a material and bring them into vacuum as free atoms. The calculated cohesive energy is 1.740 eV/atom, which is significantly lower than those for HfX_3, 1T- and 1H- HfX_2 (S,Se, and Te). Although, the cohesive energy of $HfTe_5$ is smaller than that of other Hf-based structures, the formation of $HfTe_5$ layers may be feasible through top-down synthesis approaches such as exfoliation from its bulk structure.

The dynamical stability of single-layer $HfTe_5$ is determined by calculating its phonon band dispersions through the whole BZ and it is presented in Fig. 3.1(b). It is shown that the phonon branches are almost free from any imaginary frequencies indicating the dynamical stability of the structure as a free-standing layer. The crystal structure of the 12-atom primitive cell of $HfTe_5$ possesses 3 acoustical and 33 optical phonon branches. The frequency of the highest optical branch is found to be 201 cm^{-1}. The cal-

culated Raman spectrum of single-layer $HfTe_5$ is shown on the right panel of Fig. 3.1(b). As labeled from I to VII, single-layer $HfTe_5$ exhibits seven Raman active phonon peaks as simulated at the Γ point of the BZ. The vibrational characteristics of each Raman active

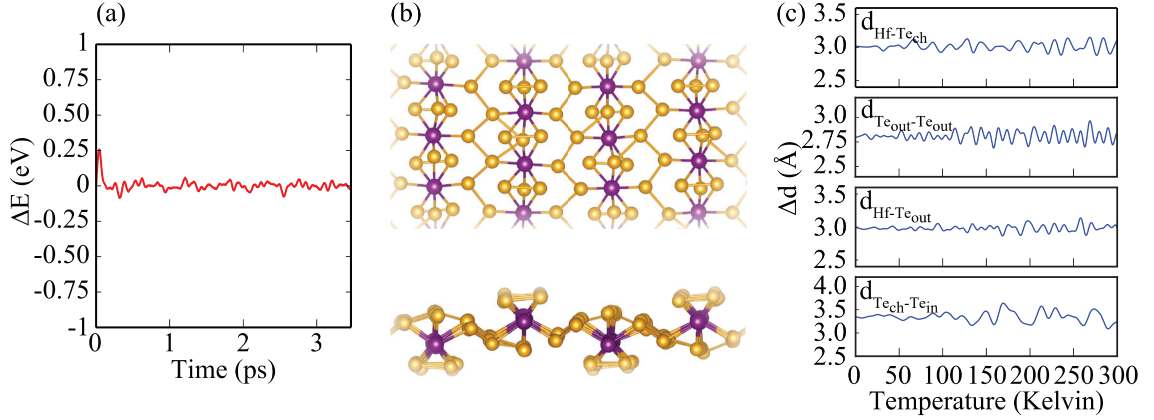

Figure 3.3. For the Quantum Molecular Dynamics simulations of $HfTe_5$ (a) total energy fluctuations, (b) final structure at 300K, and (c) variation in bond lengths of $d_{Hf-Te_{ch}}$, $d_{Hf-Te_{out}}$, $d_{Te_{out}-Te_{out}}$, and $d_{Te_{ch}-Te_{in}}$ as a function of the temperature.

mode are also shown by the eigenvector of individual atoms in Fig. 3.1(c). The highest frequency Raman active mode is calculated to occur at 164 cm^{-1} which is dominated by the mixed in-plane and out-of-plane vibration of Te_{ch} atoms. The Te_{in} atoms have tiny contribution with pure in-plane vibration against each other. The phonon modes labeled as II, III, and IV are found to be purely in-plane and have the frequencies of 89, 120, and 128 cm^{-1}, respectively. The remaining three peaks, having frequencies of 84, 134, and 158 cm^{-1}, are shown to be mixed in- and out-of-plane vibrations of Hf and Te atoms.

The thermal stability of $HfTe_5$ is examined by performing QMD simulations at room temeperature. The simulation run for totally 3.5 ps with a time step of 2 fs between each step. As shown in Fig. 3.3(a), the total energy fluctuations of the structure varies between 2 to 10 meV which states that single-layer $HfTe_5$ is thermally stable around room temperature. In order to support its thermal stability, the crystal structure of $HfTe_5$ is also visualized and shown in Fig. 3.3(b). In addition, we provide graphs showing the variations in atomic positions (bond lengths) with respect to the changing temperature. Fluctuations in bond length of four different types, namely $d_{Hf-Te_{ch}}$, $d_{Hf-Te_{out}}$, $d_{Te_{out}-Te_{out}}$, and $d_{Te_{ch}-Te_{in}}$ are presented as a function of the temperature from 0 to 300K in Fig. 3.3(c). It appears from the graphs that four bonds fluctuate around their equilibrium positions. It was reported for $ZrTe_5$ that changing temperature has effects on electronic features of pentatellurides.[177] The fluctuations in bond lengths may give predictions on the electronic features of $HfTe_5$ related to structural changes. Due to small fluctuations one

expects robust electronic behavior for $HfTe_5$. Overall, there does not occur any structural reconstructions in $HfTe_5$ around room temperature indicating the stability of the structure.

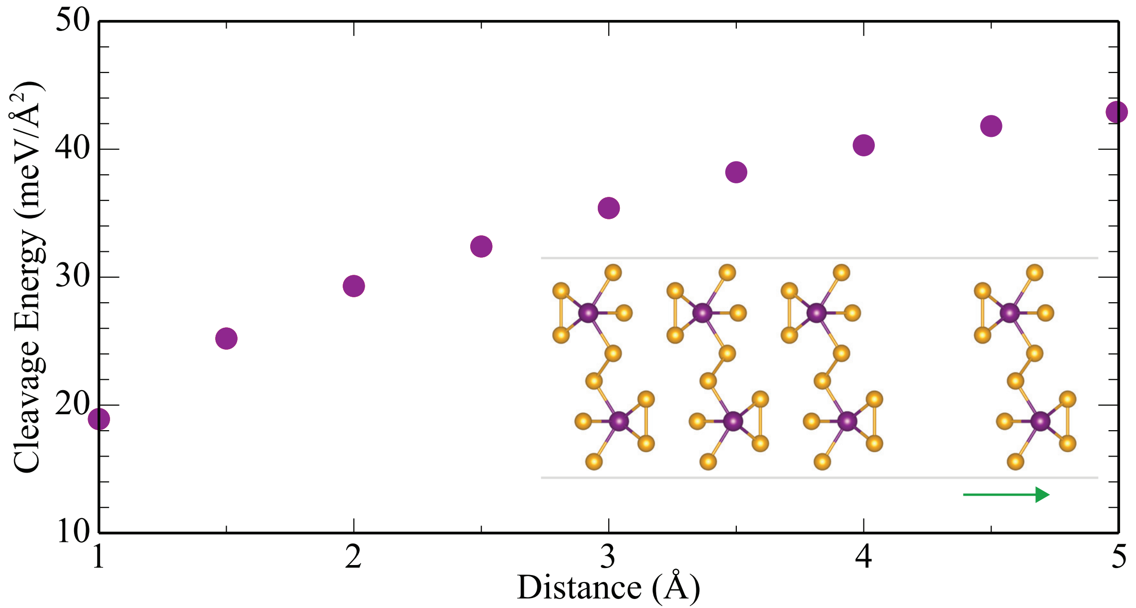

Figure 3.4. Cleavage energy of single-layer $HfTe_5$ crystal structure as a function of seperation distance.

It is worth noting that common methods for exfoliating bulk materials include mechanical exfoliation, chemical vapor deposition (CVD), and liquid-phase exfoliation. It is highly beneficial to study the mechanical exfoliation energy needed to separate the single-layer $HfTe_5$ from its bulk structures. For this purpose, we first obtained energy-minimized four-layer slabs of the $HfTe_5$ nanosheets, maintaining the identical stacking pattern observed in their bulk counterpart. In the next step, the last layer was steadily separated toward the out-of-plane vacuum direction, with a small step of 0.5 Å. Subsequently, the change in energy of the systems is calculated and the cleavage energy is obtained in meV/Å^2. As seen in the Fig. 3.4, the relative energies exhibited rapid initial increments and then reached to a converged value. According to our simulations, the exfoliation energy of 42 meV/Å^2 is predicted for the isolation of the single-layer $HfTe_5$, which is comparable to that of graphene,[178] $ZrTe_3$,[179] and WO_2:[178] 21, 25 and 62 meV/Å^2, respectively. Considering our predicted exfoliation energy, the prospect of experimentally isolating single-layer $HfTe_5$ from its bulk structures appears highly promising.

Electronic band structure and the corresponding partial density of states (PDOS) are calculated in order to investigate the electronic properties of single-layer $HfTe_5$. Although, it is not shown in Fig. 3.5(a) single-layer $HfTe_5$ is a metal without considering the effect of SOC. In addition, since the bare-GGA tends to underestimates the band gap of

semiconductors, electronic band structure calculations are performed within HSEO6 correction. $HfTe_5$ is found to be a semiconductor with an indirect band gap energy of 0.158 eV using HSE06 correction. The valence band maximum (VBM) and the conduction

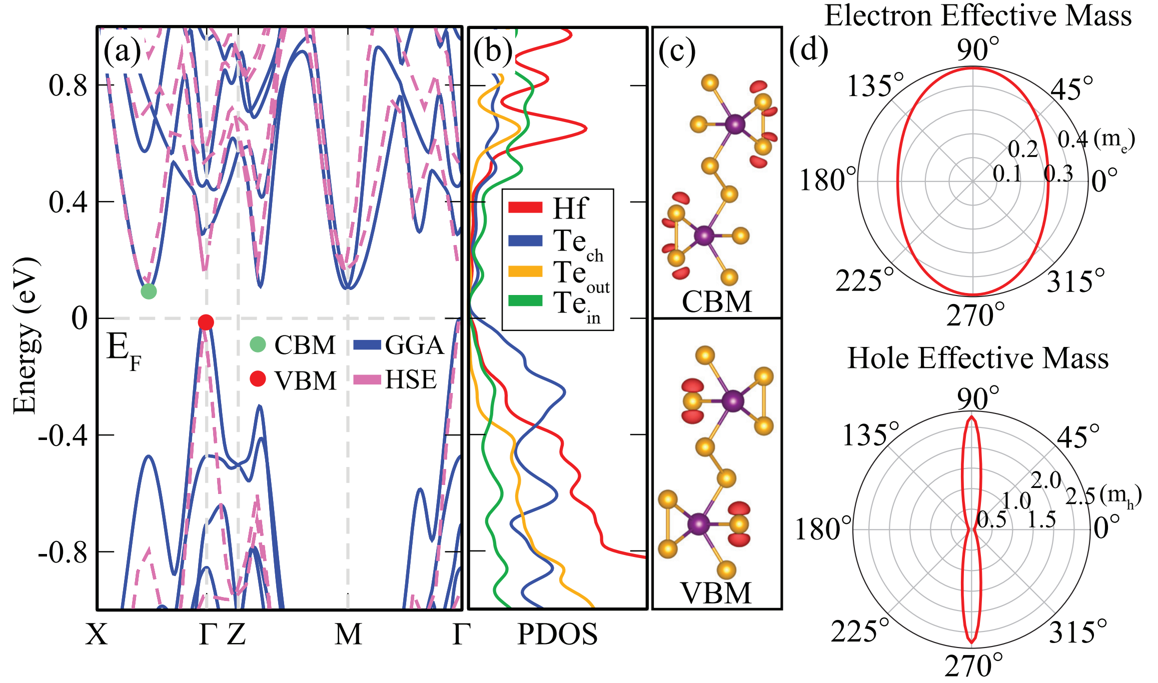

Figure 3.5. (a) The calculated electronic band dispersions of $HfTe_5$ with (b) corresponding partial density of states. (c) The atomic orbital contributions to charge densities of the VBM and the CBM states. (d) Effective masses of electrons and holes in single-layer $HfTe_5$ for different orientation angles.

band minimum (CBM) are found to reside at the Γ and between the X-Γ, respectively. The atomic orbital contributions to the VBM and CBM states are shown in Fig. 3.5(c) and it is found that while VBM is composed of p_z of the Te_{in} atoms while CBM state arises from the mixed p_z and p_y (out-of-plane) orbitals of the Te_{out} atoms, which are also supported by the PDOS shown in Fig. 3.5(b).

We further analyze both the electron and hole effective masses of single-layer $HfTe_5$ by considering the in-plane anisotropy of the structure. The effective masses are calculated by parabolic fitting of the band extrema using the formula E=$\hbar^2 k^2/2m^*$. The hole effective masses along the $X - \Gamma$ and $\Gamma - Z$ high symmetry directions of the VBM are calculated to be 0.073 and 2.758 m_0, respectively, where m_0 is the free electron mass. In addition, the electron effective masses are found to be 0.316 and 0.476 m_0 along the $X - \Gamma$ direction from X and Γ points, respectively. In addition, the in-plane anisotropy of the structure on the effective masses is obtained by plotting the orientation-dependent behavior of the masses using the formula:[180]

$$m^* = \frac{1}{[(cos^2\theta/m^*_{Hf^{\|}_{ch}}) + (sin^2\theta/m^*_{Hf^{\perp}_{ch}})]} \tag{3.1}$$

where θ is the angle between an arbitrary direction and the $Hf^{\|}_{ch}$ orientation (which is defined as the parallel direction along the Hf-chains). The coefficients $m^*_{Hf^{\|}_{ch}}$ and $m^*_{Hf^{\perp}_{ch}}$ represent the effective masses along the $Hf^{\|}_{ch}$ and $Hf^{\perp}_{ch}$ directions to the Hf-chains, respectively. It is shown that both electron and hole effective masses display decreasing trend along the $Hf^{\|}_{ch}$ direction, which is much greater for the hole effective mass. Moreover, behavior of holes is found to be more anisotropic as compared to that of electrons as a consequence of the anisotropy of the VBM states (see Fig. 3.5(d)).

The carrier mobility μ of 2D materials can be determined by using the following equation:

$$\mu = \frac{e\hbar^3 C_{2D}}{k_B T m^* m_d (E_1^i)^2} \tag{3.2}$$

where $\hbar$ is the Planck constant, C_{2D} is the elastic modulus, k_B is the Boltzmann constant, T is the temperature, m^* is the effective masss of charge carriers, and $m_d = \sqrt{m^*_{Hf^{\|}_{ch}} m^*_{Hf^{\perp}_{ch}}}$ is the average effective mass. E_1 is the deformation potential (DP) constant, which is proportional to the band edge (VBM or CBM) shift induced by external strain. E_1 is calculated from $\Delta E = E_1(\Delta l/l_0)$, in which ΔE is the energy shift of the band edge position along $Hf^{\|}_{ch}$ and $Hf^{\perp}_{ch}$ directions, the energies of the band edges are calculated with respect to the vacuum level. l_0 is the unstrained lattice constant along the transport direction, and Δl is the deformation of l_0 along the same direction. For VBM, E_1 is found to be -4.320, and 1.442 eV along $Hf^{\|}_{ch}$ and $Hf^{\perp}_{ch}$, respectively. In the case of CBM, values are found to be -0.360, and 1.800 eV, respectively. DP values also show the anisotropic nature of single-layer $HfTe_5$. By performing the first-principles calculations

Table 3.2. For the single-layer $HfTe_5$; deformation energy, E_1; the effective mass m^*; elastic moduli, C_{2D}; and the carrier mobilities, μ.

Direction	Carrier Type	E_1 (eV)	m^* (m_0)	C_{2D} (N/m)	μ_{2D} ($m^2V^{-1}s^{-1}$)
$Hf^{\|}_{ch}$	Electron	-0.360	0.316	38	5.107
	Hole	-4.320	0.073	38	0.132
$Hf^{\perp}_{ch}$	Electron	1.800	0.476	62	0.221
	Hole	1.442	2.758	62	0.051

and using deformation potential theory, it is examined the carrier mobilities of $HfTe_5$ structure along $Hf^{\|}_{ch}$ and $Hf^{\perp}_{ch}$ directions. The carrier mobilities at room temperature (300K) show strong in-plane anisotropy. The calculated carrier mobilities of single-layer

$HfTe_5$ structure are summarized in Table 3.2. The hole mobilities are calculated to be 0.132, and 0.051 $m^2V^{-1}s^{-1}$, while the electron mobilities are found to be 5.107, and 0.221 $m^2V^{-1}s^{-1}$, along $Hf_{ch}^{\parallel}$ and $Hf_{ch}^{\perp}$ directions, respectively. As compared to the hole mobility of $ZrTe_5$ (0.3 and 0.15 $m^2V^{-1}s^{-1}$ along a- and c-axis),[181] the hole mobilities of the $HfTe_5$ structure are lower for two directions. Moreover, the electron mobilities of black phosphorus (BP) were reported to be 0.11 and 0.008 $m^2V^{-1}s^{-1}$, while the hole mobilities were found to be 0.070 and 0.260 $m^2V^{-1}s^{-1}$ along armchair and zigzag directions, respectively.[182] Electron mobility of single-layer $HfTe_5$ is higher than BP along two orientation. Hole mobility of $HfTe_5$ is lower (higher) along zigzag (armchair) directions of BP.

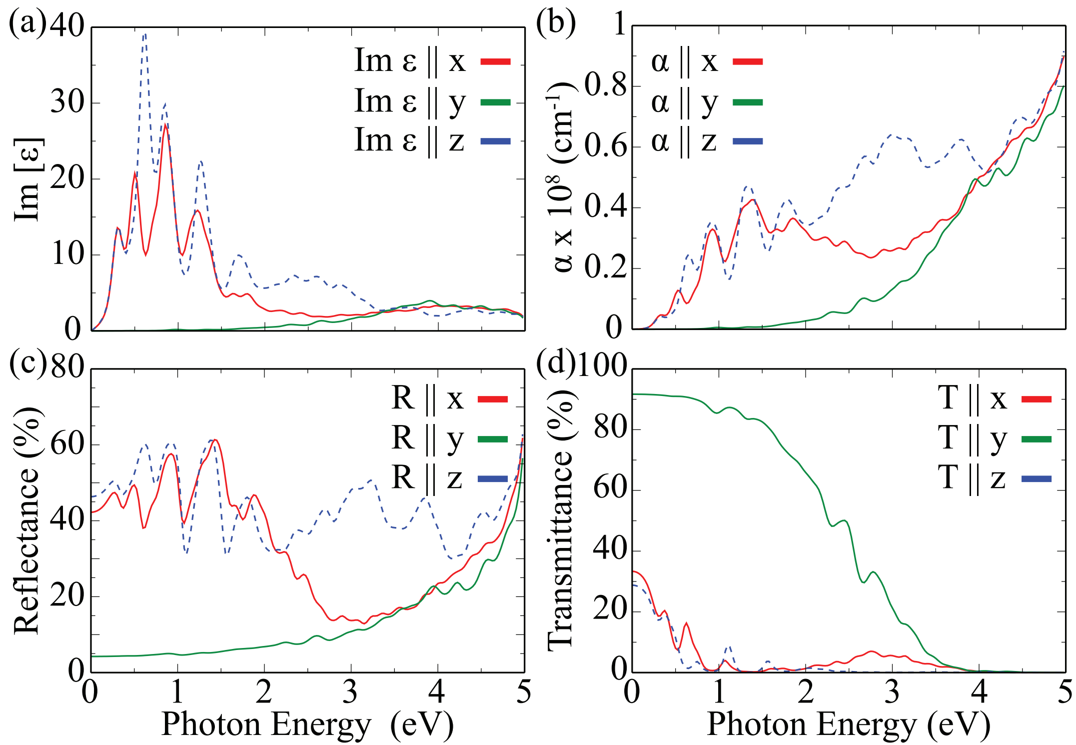

Figure 3.6. For single-layer $HfTe_5$ structure, calculated in- and out-of-plane (a) component of the imaginary parts of the dielectric function, (b) absorption, (c) reflectance, and (d) transmittance spectra, as a function of photon energy.

The GGA-PBE approximation is carried out to understand the light-matter interaction and optical properties of single-layer $HfTe_5$ structure, as illustrated in Figs. 3.6(a-d). Absorption coefficient, reflectance, and transmittance spectra are simulated through calculation of the frequency-dependent complex dielectric function. Firstly, the acquired real (ε_1) and imaginary (ε_2) parts of the dielectric function are used to calculate the refractive index (n) and extinction coefficient (κ), using the given formulas:

$$n = \frac{1}{\sqrt{2}} \left(\varepsilon_1 + \left(\varepsilon_1^2 + \varepsilon_2^2 \right)^{1/2} \right)^{1/2}$$
$$\kappa = \frac{1}{\sqrt{2}} \left(-\varepsilon_1 + \left(\varepsilon_1^2 + \varepsilon_2^2 \right)^{1/2} \right)^{1/2} \tag{3.3}$$

and furthermore, reflectance R(ω) and transmittance T(ω) spectra were predicted using the following equations:

$$R(\omega) = \frac{(n-1)^2 + \kappa^2}{(n+1)^2 + \kappa^2}$$
$$T(\omega) = (1 - R(\omega))^2 e^{-\alpha|\omega|l} \tag{3.4}$$

where l is the layer thickness, and $\alpha(\omega)$ is the absorption coefficient, which is calculated by the formula:

$$\alpha(\omega) = \sqrt{2\omega} \left[\left((\varepsilon_1(\omega))^2 + (\varepsilon_2(\omega))^2 \right)^{\frac{1}{2}} - \varepsilon_1(\omega) \right]^{\frac{1}{2}} \tag{3.5}$$

It is considered both in-plane and out-of-plane light polarizations to understand the effect of dipole orientation on the optical response of the structure. Because of the anisotropic geometry of the $HfTe_5$ nanosheet along the x-, y-, and z-axis, the optical properties are anisotropic for light polarizations along the in-plane ($E||x$ and $E||z$) and out-of-plane ($E||y$) directions. The imaginary part of the dielectric constant ($Im[\varepsilon]$ of the structure versus photon energy for all polarization directions are shown in Fig. 3.6(a). For x ($Hf_{ch}^{||}$) and z ($Hf_{ch}^{\perp}$) directions the lowest energy peaks, which correspond to the direct transition at the Γ point of the electronic band structure, are found to be at 0.30 eV. We next investigate the optical absorption coefficient of single-layer $HfTe_5$. The absorption coefficient determines how deeply light of a specific energy (or wavelength) can penetrate into a material before being absorbed. The absorption coefficients are illustrated in Fig. 3.6(b), the optical absorption of the structure is found to be highly anisotropic. In the absorption spectra, the first three absorption peaks are found at energies of 0.31 eV, 0.52 eV, and 0.92 eV for the x direction, and 0.30 eV, 0.64 eV, and 0.90 eV for the z direction. The peaks at 0.3 eV corresponds to the optical band gap (E_{opt}) of the structure and it arises from the in-plane dipole orientation, and almost compatible with our predicted band gap for single-layer $HfTe_5$ crystal. The highly anisotropic optical absorption along the $HfTe_5$ nanosheet can be useful for the employment in the direction-dependent optoelectronic nanodevices. In contrast to in-plane absorption, much weaker out-of-plane absorption is expected because of the enhanced quantum effects in the 2D limit, which lead to the decrease of the strength of dipole oscillations along the direction perpendicular to the sheet normal. The first peak along the out-of-plane direction occurs in between 2-2.5 eV. The reflectivity of single-layer $HfTe_5$ is shown in Fig. 3.6(c). The in-plane reflectivity of the

$HfTe_5$ is significantly higher than that of along out-of-plane direction. On the other hand, the transmittance of the structure in the out-of-plane direction is considerably greater than its transmittance in the in-plane direction. Maximum reflectivity for $HfTe_5$ along in-plane polarization is obtained at energy range between 0.6 and 1.5 eV while it is at energy range of 4.0-4.5 eV along out-of-plane direction. Our results show that the reflectivity along perpendicular polarization is larger than the parallel one at low frequencies. The calculated transmittance spectrum indicates that the transmission rate remains close to 0% in both the out-of-plane and in-plane directions range from 4 to 5 eV, which can be attributed to the small band gap energy of the material. Presented results confirm appealing anisotropic optical characteristics of the $HfTe_5$. Anisotropic optical features of $HfTe_5$ are promising for design of novel optoelectronic nanodevices that exploit their anisotropic properties, such as polarization-sensitive photodetectors.

Table 3.3. For single-layer $HfTe_5$, the relaxed ion elastic coefficients C_{ij}; the corresponding in-plane stiffness C, and Poisson ratio υ, along $Hf_{ch}^{\|}$ and $Hf_{ch}^{\perp}$ directions.

	C_{11} (N/m)	C_{13} (N/m)	C_{31} (N/m)	C_{33} (N/m)	C_{66} (N/m)	C_a (N/m)	C_c (N/m)	υ_a	υ_c
$HfTe_5$	66	13	13	40	20	38	62	0.32	0.20

The strain energy of a given crystal must always be positive for all possible values of applied strain, otherwise the crystal would be mechanically unstable. The quadratic form ($1/2C_{ij}e_ie_j$) of the strain energy is positive definite for all real values of strains unless all the strains are zero. The positivity of the energy imposes further restrictions on the elastic constants, C_{ij}, depending on the crystal structure. Elastic constants characterize the ability of a material to deform under small stresses and then returning to its original shape after stress ceases. For orthorombic structure the Born-Huang criteria[183] of mechanical stability in terms of the elastic strain tensor constants, C_{11}, C_{33}, C_{13}, and C_{66}, reads as: $C_{66} > 0$ and $C_{11}C_{33} - C_{13}^2 > 0$.[184] As listed in Table 3.3, the calculated C_{ij} values satisfy the Born criteria indicating the mechanical stability of orthorhombic single-layer $HfTe_5$. The linear-elastic properties of the mechanically stable $HfTe_5$ layer can be represented by two independent constants, namely the in-plane stiffnes (C) and the Poisson ratio (υ). For determination of the linear elastic constants, the elastic strain tensor elements, C_{ij}, are used to calculate the corresponding C and υ values for all orientations of the lattice and those for two main directions are listed in Table 3.3.

The in-plane stiffness is a measure of a rigidity or the flexibility of a material and depends on the geometry of the structure and the strength of the atomic bonds between the

individual atoms under consideration. Among 2D materials, graphene is known to have the highest C value (330 N/m),[185] which is a direct result of strong sp^2 C-C bonding. As referenced to that of graphene, stiffness of single-layer $HfTe_5$ (38 and 62 N/m for the lattice directions of a and c, respectively) are considerably small indicating its soft nature.

As shown in Fig. 3.7(b-c), the elasticity of $HfTe_5$ is quite orientation-dependent. The

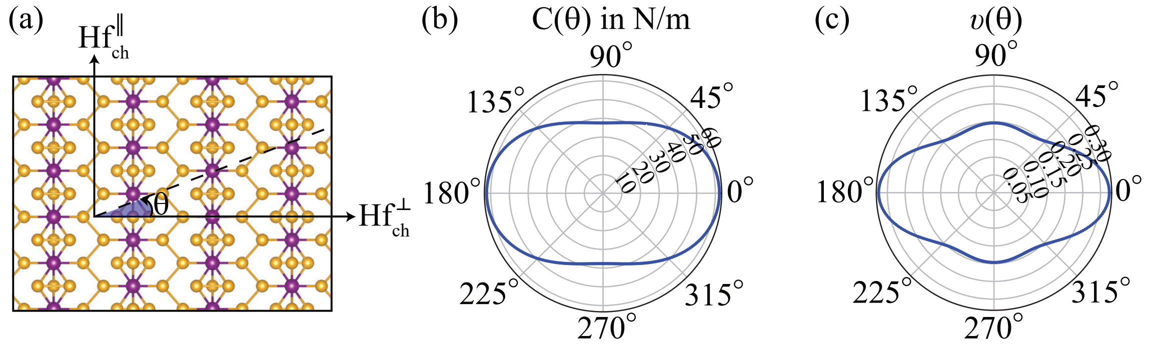

Figure 3.7. (a) Schematic representation of the orientation angle (θ). (b) The angle-dependent in-plane stiffness (C) and (c) that of Poisson ratio (υ). a and c in $HfTe_5$ structures represent the directions perpendicular and parallel to the Hf chains, respectively.

stiffness value along the Hf-chains is calculated to be almost half of that perpendicular to the Hf-chains. This means that the structure is less stiff along the Te_{ch} atoms. The orientation dependency is calculated using the formula:

$$C(\theta) = \frac{(C_{11}C_{33} - C_{13}^2)}{C_{33}cos^4(\theta) + Acos^2(\theta)sin^2(\theta) + C_{11}sin^4(\theta)} \tag{3.6}$$

where the numbers A defined as A=($C_{11}C_{33}$-C_{11}^2)/C_{66}-2C_{13} and B=C_{11}+C_{33}-($C_{11}C_{33}$-C_{13}^2)/ C_{66}. Using the above equations, in-plane stiffness along arbitrary orientations can be determined. Similarly, such an anisotropy is also found for the Poisson ratio which is defined as the ratio of transverse contraction strain to longitudinal extension. The orientation-dependency can be obtained using the formula:

$$\upsilon(\theta) = \frac{(C_{13}cos^4(\theta) - Bcos^2(\theta)sin^2(\theta) + C_{13}sin^4(\theta))}{C_{33}cos^4(\theta) + Acos^2(\theta)sin^2(\theta) + C_{11}sin^4(\theta)} \tag{3.7}$$

For the two main orientations, the Poisson ratio values are found to be 0.32 and 0.20 along the a and c lattice orientations, respectively. Apparently, the response of the lattice to the uniaxial strain is more sensitive along the Hf-Hf chains.

In experiments, depending on the synthesis technique and transfer procedure of the 2D material, various types of defects are likely to be formed or can be controllably

created. Commonly observed defect types in 2D materials include vacancies, antisite defects, substitutions, and adatoms.[186,187] It is also feasible to have oxidation of the vacancies due to unoccupied orbitals of the atoms around the vacancies. Therefore, in order to figure out the possible defects and their oxidized structures, six different types of vacancy defects are considered in single-layer $HfTe_5$. As shown in top panels of Figs. 3.8(a) and (b), the following defect types are studied, namely; vacany of one chain Te atom from the top and down of the chain ($V^{u}_{Te_u}$, $V^{d}_{Te_{ch}}$), vacany of outer and inner Te atom ($V_{Te_{out}}$, $V_{Te_{in}}$), vacany of a Te dimer ($V^{dim}_{Te_{out}}$) and vacany of a Hf atom (V_{Hf}). For the optimized defected structures, the expansion or the compression rate of the lattice is calculated with respect to the lattice parameter of bare $HfTe_5$. As seen in Table 3.4, most of the defects

Table 3.4. For various defects in $HfTe_5$, the type of the defect; the expansion rate of the lattice parameters ($-$ and $+$ stand for compression and expansion, respectively), a and c; the defect formation energy E_{for}; and the net magnetic moment of the defect domain, μ. For comparability, formation energies of Te-Hf vacancies are given in eV/(Te-Hf).

Defect Type	Δa (%)	Δc (%)	E_{for} (eV)	$\Delta\mu$ (μ_B)
$V^{u}_{Te_{ch}}$	-1.00	-1.15	1.62	0
$V^{d}_{Te_{ch}}$	-1.08	-1.22	1.62	0
$V_{Te_{out}}$	-0.41	-0.14	1.13	0
$V_{Te_{in}}$	-0.25	-1.72	2.16	0
$V^{dim}_{Te_{out}}$	-1.91	+1.15	2.27	1
V_{Hf}	+0.25	-4.03	3.38	1

lead to shrinkage in the lattice, while Hf and two Te defects shrink and expand along $Hf^{\parallel}_{ch}$ and $Hf^{\perp}_{ch}$ directions. Different types of single Te vacancies lead to the shrinking of the lattice along both orientations. However, as two outer Te atoms are missing in the structure, the optimized structure shrinks along the $Hf^{\parallel}_{ch}$ direction while it expands along the $Hf^{\perp}_{ch}$ direction. The shrinkage occurs along the Hf-Hf chains due to the attraction between Hf atoms. In contrast, formation of the Hf vacancy gives rise to the shrinking of the lattice along the $Hf^{\perp}_{ch}$ direction while expansion occurs along the a direction. The reason for such opposite behavior of V_{Hf} is that Hf atoms along the chain get closer and thus the lattice expands along the $Hf^{\parallel}_{ch}$ direction. As the lattice expands along the $Hf^{\parallel}_{ch}$ direction, the Te_{ch} atoms tend to get closer and the lattice shrinks along the $Hf^{\perp}_{ch}$ direction. Defect formation energies of each defect type are calculated by using the equation: $E_{formation} = E_{defect} - E_{bare} \pm \Sigma n_i E_i$, where E_{bare} and $E_{defected}$ represent the total energies of the bare and defected single-layer $HfTe_5$ supercells, respectively, while n_i and E_i denote the total number of and the total energy of the vacant atom. The $+$ sign is used

for the adsorbed atoms while the $-$ sign for the vacant atoms. The chemical potentials for Hf and Te atoms are calculated from their bulk forms and using the single-layer energy of $HfTe_5$ by the following formula: $\mu_{HfTe_5} = \mu_{Hf} + 5\mu_{Te}$, where μ_{Hf} and μ_{Te}

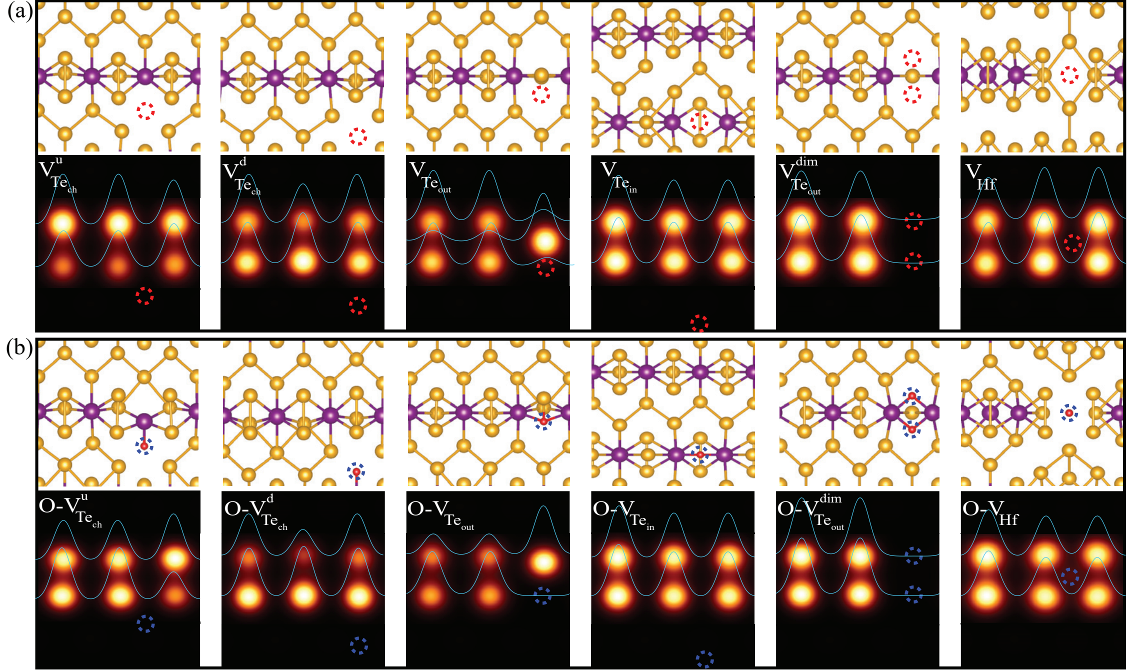

Figure 3.8. (a) Top views and simulated STM images of defected $HfTe_5$ and (b) those for the oxidized defect structures. The dashed red circles indicate the vacant atom in the structure and the blue dashed circles stand for the O atoms. Turquoise lines represent the line profile of STM images of defected and oxidized defected structures.

represent the chemical potentials of Hf and Te atoms, respectively, while μ_{HfTe_5} is the total energy of single-layer $HfTe_5$. The defect formation energies of $V^{u}_{Te_ch}$, $V^{d}_{Te_ch}$, $V_{Te_{out}}$, $V_{Te_{in}}$, $V^{dim}_{Te_{out}}$, and V_{Hf} vacancies are calculated to be 1.62, 1.62, 1.13, 2.16, 2.27, and 3.38 eV/atom, respectively. The formation of $V_{Te_{out}}$ is the most favorable defect among the all considered types. On the other hand, the formation of V_{Hf} is the less favorable since it has the highest formation energy. To determine the nature of magnetic coupling between a defect domain and its host lattice, the net magnetic moment (in $\Delta\mu$) of the each defect type is calculated and the results are listed in Table 3.4. While the non-magnetic feature of single-layer $HfTe_5$ is preserved via $V^{u}_{Te_ch}$, $V^{d}_{Te_ch}$, $V_{Te_{out}}$, and $V_{Te_{in}}$ defects, the $V^{dim}_{Te_{out}}$ and V_{Hf} vacancies give rise to a local magnetism with 1 μ_B of magnetic moment per structure. The origin of magnetization for $V^{dim}_{Te_{out}}$ is the magnetic contribution resulting from the unoccupied orbitals of the two Hf atoms bonding with the vacant outer dimer. The magnetization for the V_{Hf} arises from the unpaired Hf-d orbitals. The presence of intrinsic and extrinsic defects makes them sensitive to oxygen present in their

environment, and the presence of oxygen in the environment can cause to oxidation of the material especially from the defect site. Particularly, exposure to air frequently results in the oxidation of materials, which has a significant effect on the functional properties and efficacy of devices constructed.[188] In order to study the effect of oxygen adsorption on the vacancies, equal number of O atoms with that of vacant atoms are adsorbed on the vacant sites as shown in Fig. 3.8(b). For the optimized oxygen substituted structures, the expansion or the compression rate of the lattice is calculated with respect to the lattice parameters of defected $HfTe_5$. As listed in Table 3.5, each of the O-adsorbed vacancy defect exhibits opposite behavior along the two lattice orientations by means of the lattice expansion rates, which causes the increase of the in-plane anisotropy of the structure. The highest shrinking and expansion occurs for the O-adsorption in V_{Hf} due to the atomic radius difference of O and Hf atoms that a single O atom does not fill the location of a Hf vacancy. The binding energy of O atoms on the vacant sites are calculated by using

Table 3.5. For the oxygen substituted in defected single-layer $HfTe_5$, we present the different types of oxidation; the expansion rate of the lattice parameter (- and + stand for compression and expansion, respectively), a and c; the defect formation energy E_{for}; the net magnetic moment of the defect domain, μ; the electronic ground state; and the energy band gap of defected structure. For comparability, binding energy for oxygen atom adsorbed on the Te-Hf vacancies are given in eV/Te-Hf.

Defect Type	Δa (%)	Δc (%)	E_{for} (eV)	$\Delta\mu$ (μ_B)
O-$V^{u}_{Te_{ch}}$	0.25	-0.58	5.35	0
O-$V^{d}_{Te_{ch}}$	0.33	-0.65	5.35	0
O-$V_{Te_{out}}$	-0.75	0.84	6.07	0
O-$V_{Te_{in}}$	-0.83	1.46	6.74	0
O-$V^{dim}_{Te_{out}}$	-0.08	2.27	5.12	0
O-V_{Hf}	-3.24	5.40	-1.18	1

the equation: $E_{binding} = E_{vacancy} + E_O - E_{O-adsorb}$, where $E_{vacancy}$ represents the total energy of the defected structure while E_O and $E_{O-adsorb}$ stand for the total energies of the single O atom and O-adsorbed defected single-layer, respectively. The binding energies of O adsorption on the various vacant sites are calculated to be 5.35, 5.35, 6.07, 6.74, 5.12 and -1.18, respectively for the O-$V^{u}_{Te_{ch}}$, O-$V^{d}_{Te_{ch}}$, O-$V_{Te_{out}}$, O-$V_{Te_{in}}$, O-$V^{dim}_{Te_{out}}$ and O-V_{Hf}. Apparently, the negative value of binding energy for the O-V_{Hf} indicates that the oxygen substitution is not favorable at the Hf-vacancy site. It is also found that the energetically most favorable adsorption site for the O atom are the inner and outer Te positions. If two O atoms fill the vacancy positions created by the outer Te-dimer, the binding energy of a

single O is lower than that of a single O at the $V_{Te_{out}}$ site. While the non-magnetic feature of single-layer $HfTe_5$ is preserved via O-$V^u_{Te_1}$, O-$V^d_{Te_{ch}}$, O-$V_{Te_{out}}$, O-$V_{Te_{in}}$, $V^{dim}_{Te_{out}}$, oxygen substituted structure of Hf vacancy (O-V_{Hf}) give rise to local magnetism with 1 μ_B of magnetic moment. The origin of magnetization for 0-V_{Hf} stems from the Hf-d orbitals.

Scanning Tunneling Microscopy (STM) is a powerful imaging technique for visualizing surfaces at the atomic scale. It allows one to observe individual atoms on surface with a good accuracy. It also provides atomically precise information about the crystal structure. Here, we present our calculated STM images for six different vacancy and their oxygen substituted structures (see Fig. 3.8). In the bare $HfTe_5$ layer, the top Te-dimers are found to be at a higher position and thus closer to the tip in STM simulation. So the bright spots belong to the top Te-dimers. As shown in Fig. 3.8(a), as either $V^u_{Te_{ch}}$ or $V^d_{Te_{ch}}$ are created in single-layer $HfTe_5$, one line of the Te-dimers become less bright and thus, the defected site can be distinguished. If the upper Te_{ch} is missing in the structure, the Te-dimer atoms closer to the vacant site will be monitored as less bright. In contrast, as the bottom Te_{ch} is removed, the Te-dimer atoms closer to the vacant site are at higher position and are brighter than their twins. In the case of $V_{Te_{out}}$, one of the top dimers is broken and remaining Te atom optimizes at the center. The structure of $V_{Te_{out}}$ can be monitored in STM as one single bright spot centered between Te-dimers. As an inner Te atom is missing in the lattice, namely the $V_{Te_{in}}$ is formed, the top Te-dimers are not affected and the STM image looks very similar to the bare structure, thus the defect site is not distinguishable. In contrast, the $V^{dim}_{Te_{out}}$ structure can be clearly observed in STM measurement since a dark site appears within the location of Te-dimer missing in the structure. In the case of Hf-vacancy, the Te-dimers closest to the Hf-vacancy site look still bright while the Te-dimer away from the vacancy becomes less brighter since the two Te atoms are attracted by a Hf atom which shifts closer to the Te-dimer. In addition, the STM line profiles along the apparent atoms are also shown on the STM images as seen in Fig. 3.8. The difference between the intensities representing different atoms can also be distinguished from the amplitudes of the line profiles.

In O-substituted structures, the O atoms can also be distinguished in some of the vacant structures by STM image analysis. When an O atom is adsorbed at the vacant site in $V^u_{Te_{ch}}$, O atom binds to the Hf atom and the Te atoms looking darker optimize at upper position and become brighter while one Te close to O atom still remains to be darker. Clearly, as seen at the first panel of Fig. 3.8(b), the presence of O atom at the $V^u_{Te_{ch}}$ site can be monitored via STM analysis. In the case of O adsorption on the $V^d_{Te_{ch}}$, the Te atoms on the vacancy site of dimers are still brighter, however, the remaining Te atoms within

the dimers are darker as compared to that of bare vacancy. The O atom at the $V_{Te_{out}}$ site can also be monitored via STM since the bright centered Te atom quite shifts and is not at the center of neighboring Te-dimers anymore. The O-$V_{Te_{in}}$ and $V_{Te_{in}}$ structures are not distinguishable through the STM analysis since the outer Te-dimers are not affected by the adsorption of O atom at the inner site. Similarly, the O atoms can not be monitored in the case of $V^{dim}_{Te_{out}}$ since two O atoms bind with neighboring Hf atoms and the Te-dimers are not affected and look still as bright spots. Finally, in the Hf-vacany structure by the O adsorption, the neighboring four Te atoms become less bright and thus, the presence of O atom can be monitored.

Table 3.6. For the single-layer TiX_5; the optimized in-plane lattice parameters, *a and c*; the atomic bond lengths between individual atoms, $d_{Ti-X_{ch}}$, $d_{Ti-X_{out}}$, $d_{X_{out}-X_{out}}$; vertical distance between uppermost and lowermost Te atoms (thickness), t; the cohesive energy per atom, E_{coh}; the work function, Φ; and electronic band gap energy E_g^{SOC}.

	a (Å)	b (Å)	$d_{Ti-X_{ch}}$ (Å)	$d_{Ti-X_{out}}$ (Å)	$d_{X_{out}-X_{out}}$ (Å)	t (Å)	E_{coh} (eV/atom)	E_g^{SOC} (eV)
TiS_5	3.39	11.42	2.56	2.52	2.07	5.71	4.679	0.06
$TiSe_5$	3.61	12.25	2.70	2.67	2.37	6.13	5.229	0.16
$TiTe_5$	3.92	13.67	2.97	2.92	2.74	6.94	5.760	0

3.2. Titanium Pentachalcogenides

The optimized atomic structures of single-layer TiX_5 (X=S, Se, and Te) are shown in Fig. 3.9(a) and (c), highlighting top and side views of the materials. The lattice structure of TiX_5 consists of two Ti-X_5 units that are oppositely oriented along the out-of-plane direction and connected through chalcogen atoms, resulting in orthorhombic lattice symmetry. Within the primitive unit cell of single-layer TiX_5, there exist three type of X atoms, namely the outer (X_{out}), inner (X_{in}), and the chain (X_{ch}) atoms as shown in Fig. 3.9(c). The two Ti-X_5 units are connected through the X_{ch} atoms in the lattice. The geometrical calculations show that the optimized in-plane anisotropic lattice parameters are *a*/*b*=3.39/11.42 Å, 3.61/12.25 Å, 3.92/13.67 Å for TiS_5, $TiSe_5$, and $TiTe_5$, respectively (see Table 3.6). The direction *a* is defined as parallel to Ti chains ($Ti^{\parallel}_{ch}$), while *b* is defined as perpendicular to Ti chains ($Ti^{\perp}_{ch}$). The corresponding Ti-X bond lengths are found to be 2.56 Å, 2.70 Å, and 2.97 Å for Ti-S_{ch}, Ti-Se_{ch}, and Ti-Te_{ch}, respectively. The Ti-X bond lengths for Ti-S_{out}, Ti-Se_{out}, and Ti-Te_{out} are slightly shorter, calculated to be 2.52

Å, 2.67 Å, and 2.92 Å, respectively. Additionally, the outer S, Se, and Te atoms are found to form dimers with the corresponding S-S, Se-Se, and Te-Te bond lengths of 2.07, 2.37, 2.74 Å, respectively, while the one formed between the S_{ch}, Se_{ch}, and Te_{ch} atoms are 2.27, 2.55, and 2.94 Å, respectively. As the atomic radius of the chalcogenide atoms increases from S to Te, the bond length between Ti and X atoms also increases. It indicates

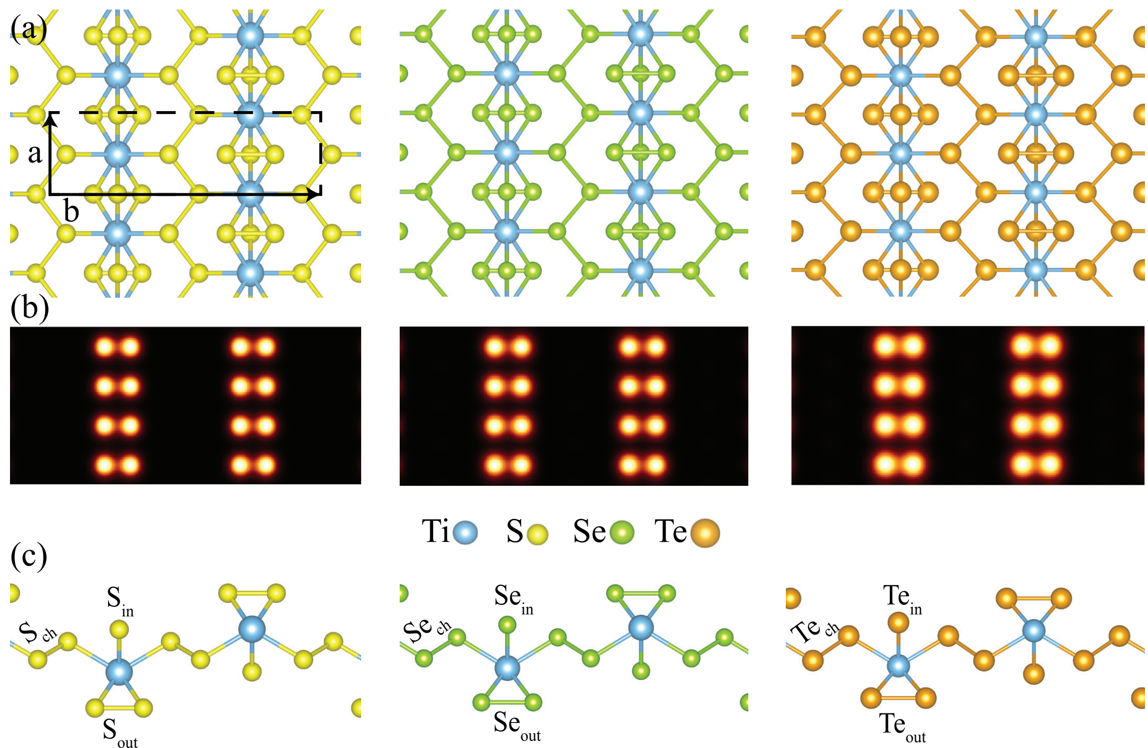

Figure 3.9. For the single-layer ultra-thin TiX_5 (X=S, Se, and Te) structures, (a) top views of the crystal structures, (b) simulated STM images, and (c) side views of the lattice structures.

the presence of relatively weaker bonds, implying that less energy is needed to remove the chalcogenide atom from the crystal structure. Moreover, the reason for the decrease in bond length among chalcogens in the order Te $>$ Se $>$ S can be attributed to the increasing electronegativity in the S $>$ Se $>$ Te. Furthermore, the vertical distance between outermost chalcogen atoms, defined as the thickness of the single-layer TiS_5, $TiSe_5$, and $TiTe_5$ are found to be 5.71 Å, 6.13 Å, 6.94 Å, respectively. In order to investigate the detailed features of crystal structures, here, we present our simulated scanning tunneling microscopy (STM) images for single-layer TiS_5, $TiSe_5$, and $TiTe_5$ structures as seen in Fig. 3.9(b). In the TiX_5 layers, the top chalcogen dimers are found to be at a higher position and therefore closer to the tip in the STM simulation. Thus, the bright spots belong to the top chalcogen dimers, and as the atomic radius of the chalcogen atom increases, the brightness of the spots in the STM simulation also increases. In order to analyze the

strength of the binding between the atoms and chemical stability of the structures, the cohesive energies E_{coh} of the TiX_5 structures are calculated. The calculated cohesive energies are 4.679, 5.229, and 5.760 eV/atom, consistent with a decrease in binding energy observed with decreasing radius and decreasing electronegativity.

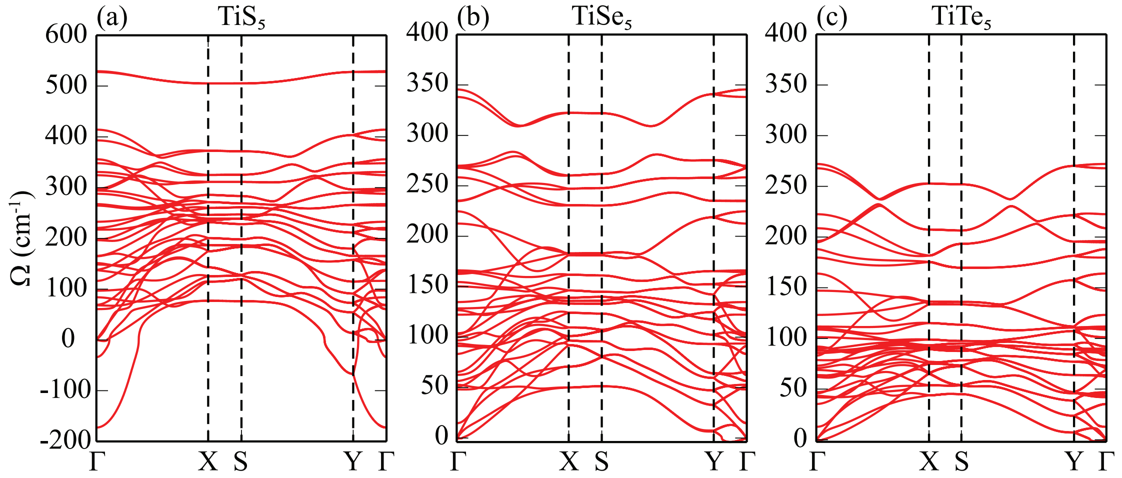

Figure 3.10. Phonon band dispersions of single-layers (a) TiS_5, (b) $TiSe_5$, and (c) $TiTe_5$, respectively.

The dynamical stability of free-standing single-layer TiX_5 structures are assessed by calculating their phonon band dispersions through the entire BZ and it is presented in Fig. 3.10(a-c). As illustrated, the phonon branches are almost free from any imaginary frequencies except around the Γ point, indicating the dynamical stability of the structures except TiS_5. The presence of imaginary frequencies in the phonon spectrum of single-layer TiS_5 indicates its structural instability. Small imaginary frequencies near the Γ point in the out-of-plane acoustic mode result from numerical artifacts caused by the lack of precision in the fast Fourier transform (FFT) grid. Specifically, TiS_5 structure dynamically unstable with a negative frequency -172.6 cm^{-1}, while $TiSe_5$ and $TiTe_5$ are dynamically stable as a free-standing layer. The crystal structure of the 12-atom primitive cell of TiX_5 exhibits 3 acoustical and 33 optical phonon branches. The frequency of the highest optical phonon branch at the Γ high symmetry point of the $TiSe_5$ and $TiTe_5$ crystal structures are 345.7 cm^{-1} and 272.1 cm^{-1}, respectively. It is seen that the frequency of phonon modes (including the maximum phonon frequency, w_{max}) gradually decrease (phonon softening) with increasing the weight the chalcogenide atom. The force constant matrices demonstrate that this decrease is attributable to both the increased mass of the X atoms and the reduced strength of interatomic connections.

The electronic band structure and the corresponding partial density of states (PDOS) are calculated in order to analyze the electronic features of single-layer TiX_5 crystals.

Electronic band structure calculations are conducted across the whole BZ to explore the electron behavior in the momentum space of the TiX_5 structure, considering spin-orbit interactions (SOC) along with the U-Hubbard term. TiS_5 and $TiSe_5$ are found to be

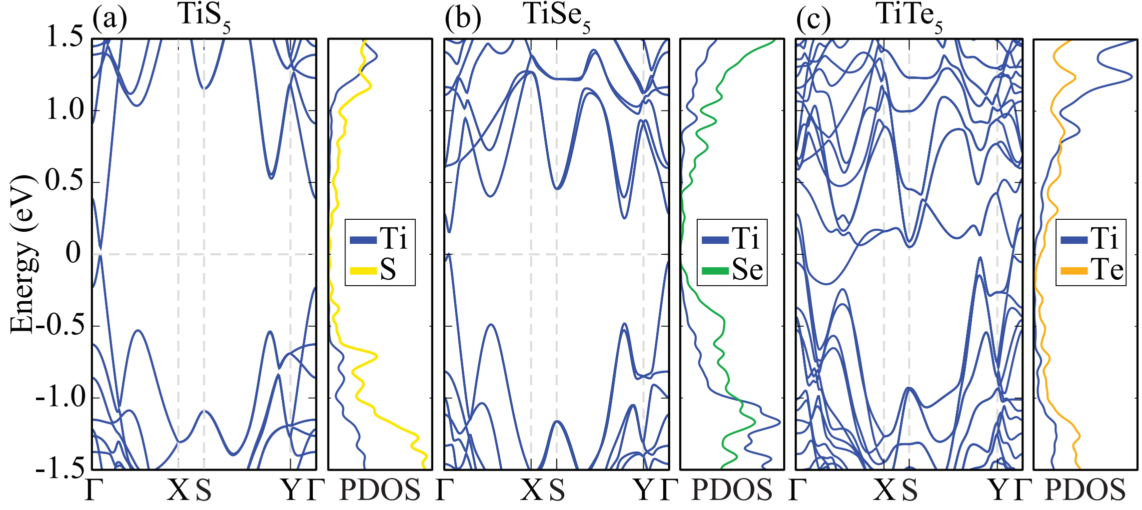

Figure 3.11. (a) The calculated electronic band dispersions (SOC) of single-layer TiX_5 structures. The Fermi energy (E_F) level is set to the top of valence states and (b) corresponding partial density of states of single-layer TiX_5 crystals.

a semiconductor with a direct band gap energy of 0.06 and 0.16 eV, respectively, while $TiTe_5$ structure possesses metallic behavior as seen in Fig. 3.11(a-c). The valance band maximum (VBM) and the conduction band minimum (CBM) are found to at the between Γ and X high symmetry points.

In order for a crystal to remain mechanically stable, the strain energy must always be positive for all potential values of applied strain. The quadratic form ($1/2C_{ij}e_ie_j$) representing the strain energy is always positive for any real values of strains, except when all the strains are zero. The energy's positivity imposes additional constraints on the elastic constants, C_{ij}, which vary according to the crystal structure. Elastic constants quantify a material's capacity to undergo deformation in response to minor loads and thereafter revert back to its initial shape once the stress is removed. The Born-Huang requirements for mechanical stability in an orthorhombic structure, as described by the elastic strain tensor constants C_{11}, C_{22}, C_{12}, and C_{66}, can be expressed as stated in the work of Born and Huang (1955)[183] and Bhattacharya (2022) [$C_{66} > 0$ and $C_{11}C_{33}-C_{13}^2 > 0$].[184] The C_{ij} values obtained for orthorhombic single-layer TiX_5, as presented in Table 3.7, satisfy the Born conditions, indicating the mechanical stability of the material. For the HfTe5 layer, its mechanical stability is characterized by two distinct parameters: the in-plane stiffness (C) and the Poisson ratio (υ). The linear elastic constants are determined using the elastic strain tensor elements, Cij, to compute the corresponding C and υ values

for all lattice orientations and those for two main directions are presented in Table 3.7.

Table 3.7. For single-layer TiX_5, the relaxed ion elastic coefficients C_{ij}; the corresponding in-plane stiffness C, and Poisson ratio υ, along $Ti_{ch}^{\parallel}$ and $Ti_{ch}^{\perp}$ directions.

	C_{11} (N/m)	C_{13} (N/m)	C_{31} (N/m)	C_{33} (N/m)	C_{66} (N/m)	C_a (N/m)	C_c (N/m)	υ_a	υ_c
TiS_5	98	18	18	50	31	92	47	0.35	0.18
$TiSe_5$	83	18	18	49	28	76	45	0.36	0.22
$TiTe_5$	66	15	15	44	26	60	41	0.34	0.23

The in-plane stiffness is a quantitative measure of the rigidity or flexibility of a material. It is determined by the structure's geometry and the strength of the atomic connections between the individual atoms being analyzed. As listed in Table 3.7, the stiffness values of TiS_5, $TiSe_5$, and $TiTe_5$ are 92/47, 76/45, and 60/41 N/m along the parallel and perpendicular direction, respectively. As compared to the single-layer $HfTe_5$ (38/65 N/m), TiX_5 structures exhibit stiffer character along a direction while possessing softer feature along b direction. As seen in Fig. 3.12, the elasticity of TiX_5 crystals exhibits direction-

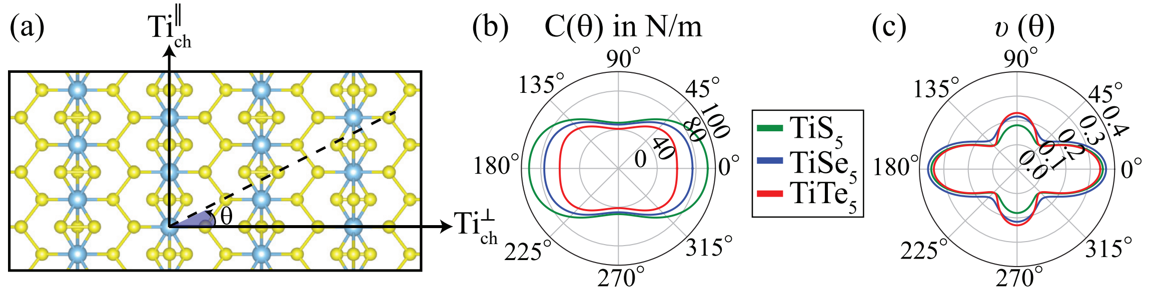

Figure 3.12. (a) Schematic representation of the orientation angle (θ). (b) The angle-dependent in-plane stiffness (C) and (c) that of Poisson ratio (υ). a and b in TiX_5 structures represent the directions perpendicular and parallel to the Ti chains, respectively.

dependence. The Poisson ratio, which is defined as the ratio of transverse contraction strain to longitudinal extension, also shows anisotropy. For the two main directions, the Poisson ratio values of TiS_5, $TiSe_5$, and $TiTe_5$ are calculated to be 0.35/0.18, 0.36/0.22, and 0.34/0.23 along the a and c lattice orientations, respectively. The lattice structures are more sensitive to uniaxial strain along the Ti-Ti chains, similar to $HfTe_5$.

CHAPTER 4

NOVEL HIGHLY ANISOTROPIC SINGLE-LAYER TRANSITION METAL TRICHALCOGENIDES

In this chapter, the structural, vibrational, electronic, optical and elastic properties of single-layer TaX_3 structures were investigated by means of ab-initio calculations. It was found that free-standing TaX_3 crystal structures are dynamically and mechanically stable metallic materials, exhibiting in-plane anisotropy. The rest of paper is organized as follows; Structural and vibrational properties of TaX_3 layers are presented in Section 4.1. Electronic, optical (Section 4.2), and elastic properties (Section 4.3) of single-layers of TaX_3 are illustrated.

4.1. Structural and Vibrational Properties

The optimized atomic structures of single-layer TaX_3 are illustrated in Fig. 4.1(a) and (b) showcasing top and side views. Single-layer TaX_3 crystal structures consist of two different types of atoms (Ta, and X:S, Se, Te) with monoclinic lattice symmetry ($P2_1/m$), and the unit cell is composed of X-Ta-X sandwich layers. For TaS_3, $TaSe_3$, and $TaTe_3$, the

Table 4.1. For the single-layer 2D TaX_3: the optimized in-plane lattice parameters (a *and* b), vertical distance between uppermost and lowermost S atoms (t), the cohesive energy per atom (E_{coh}), and the work function, (Φ).

	a (Å)	b (Å)	t (Å)	E_{coh} (eV/atom)	Φ (eV)
TaS_3	14.60	3.42	7.75	4.79	4.64
$TaSe_3$	15.60	3.55	7.95	4.29	4.37
$TaTe_3$	17.15	3.77	8.75	3.80	4.12

optimized in-plane anisotropic lattice parameters are calculated to be $a/b = 14.60/3.42$, $15.60/3.55$, and $17.15/3.77$, respectively. Highly anisotropic nature of TaX_3 crystals is originated by extending the prismatic TaX_6 chains of TaX_3 along the b-axis. The increase in the atomic radius of the chalcogenide atom from S to Te leads to an elongation in the bond length between Ta and X atoms. Specifically, bond lengths vary between 2.56-2.71,

2.67-2.91, and 2.87-4.95 for TaS_3, $TaSe_3$ and $TaTe_3$, respectively. The thicknesses (which

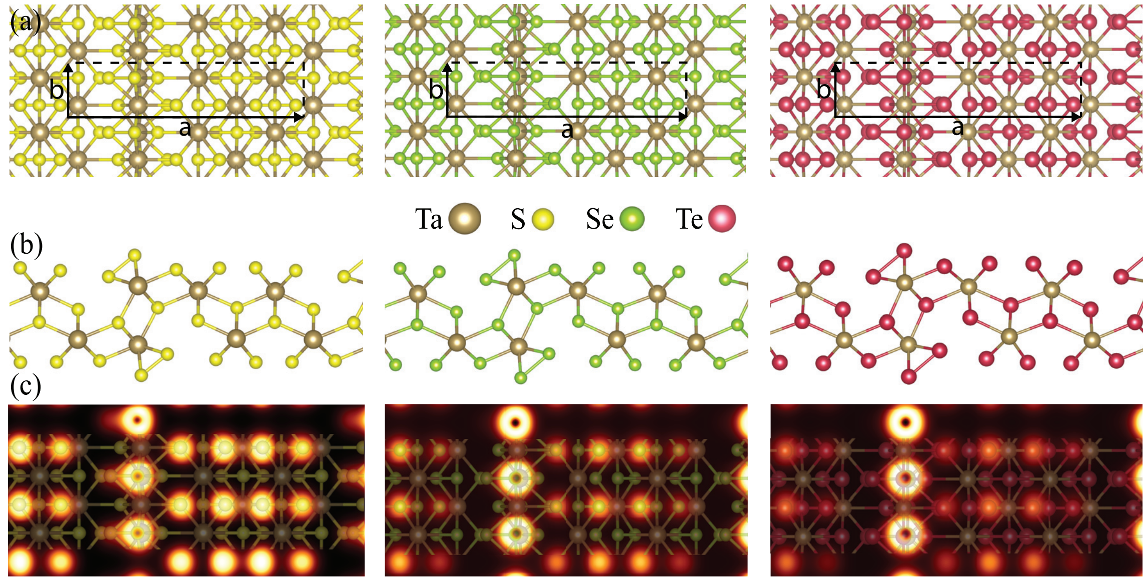

Figure 4.1. For single-layer TaX_3 structures (a) top and (b) side view of the optimized atomic structures. (c) Simulated STM images of TaS_3, $TaSe_3$ and $TaTe_3$ crystals.

is defined to be the vertical distance between uppermost and lowermost chalcogenide atoms) of the single layers are calculated to be 7.75, 7.95, and 8.75 Åfor TaS_3, $TaSe_3$ and $TaTe_3$, respectively. According to spin-polarized calculations, it is found that TaX_3 systems are not magnetic. The calculated structural parameters are summarized in Table 4.1. The lattice parameters, bond lengths, and geometric thickness exhibit an increasing trend with the expanding atomic radius of the chalcogenide (X) atom in single-layer TaX_3 structures. Additionally, in order to analyze the strength of the binding between the atoms, the cohesive energy per atom E_coh of the TaX_3 structures are calculated using the following formula: $E_{coh} = mE_{Ta} + nE_X - E_{TaX_3}/(m+n)$, where m and n stand for the number of Ta and X atoms, respectively, in the unit cell. E_{Ta} and E_X are the single atom energies of Ta and X, respectively. The cohesive energy offers insights into the energy needed to separate individual atoms within a material and move them into a vacuum as independent atoms. The cohesive energies for TaS_3, $TaSe_3$ and $TaTe_3$ are calculated as 4.79, 4.29, 3.80 eV/atom, respectively. The cohesive energy decreases as the size of the structures increases. The cohesive energy of TiS_3 (4.72 eV/atom), $TiSe_3$ (4.37 eV/atom), $TiTe_3$ (3.81 eV/atom), ZrS_3 (5.21 eV/atom), $ZrSe_3$ (4.75 eV/atom), $ZrTe_3$ (4.26 eV/atom), HfS_3 (5.49 eV/atom), $HfSe_3$ (4.72 eV/atom), and $HfTe_3$ (4.20 eV/atom) are reported.[189] The cohesive energy values of TaX_3 structures are comparable to those of Ti-based structures, while the cohesive energies of the Zr and Hf-based structures are higher than TaX_3. The formation of TaX_3 layers can potentially be achieved through top-down synthesis

approaches, such as exfoliation from its bulk structures. Work function provides insights into the electronic properties and surface behavior of the materials. The work functions of electrode metals govern the Schottky barrier height of metal-semiconductor connections, hence impacting the injection of charge carriers. Utilizing the suitable metal as the elec-

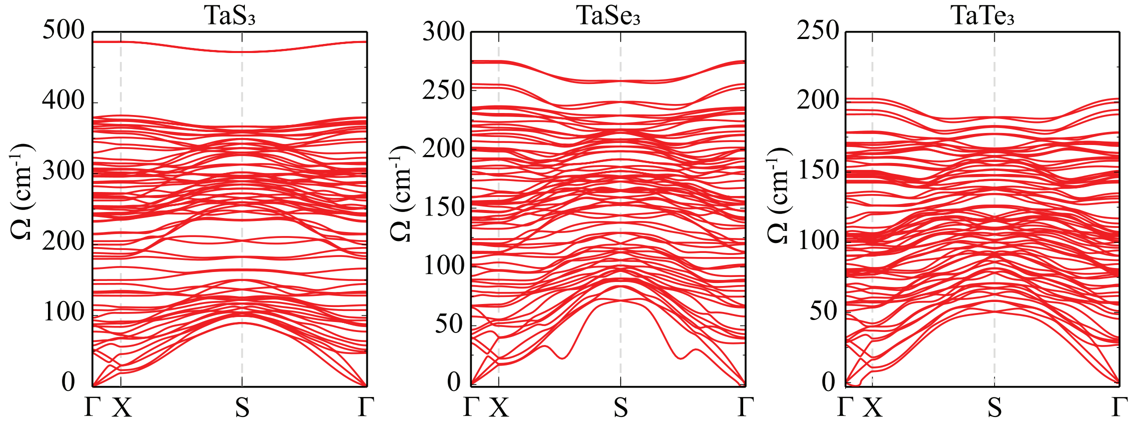

Figure 4.2. The phonon band dispersions of single-layer TaS_3, $TaSe_3$ and $TaTe_3$ crystals.

trode is a highly effective method for enhancing connections. Using the local potential distribution along the out-of-plane direction, the work function values are calculated to be 4.65, 4.37, 4.12 for TaS_3, $TaSe_3$ and $TaTe_3$, respectively. The work function values of ZrS_3, $ZrSe_3$, HfS_3, $HfSe_3$, are reported to be 5.57, 5.17, 5.48, 5.11 eV, respectively.[82] Bader charge analysis reveals that the formation of three single-layers of TaX_3 structures, charge donation occurs from the Ta atom to the surface and internal chalcogen X atoms which indicates the partially ionic character between the individual atoms. The amount of charge donation decreased as the electronegativity of chalcogen X atoms decreased. In addition, Bader charge analysis indicate that electrostatic interactions play a critical role in keeping the structural integrity of single-layer TaX_3 crystals. Scanning tunneling microscopy (STM) is a highly effective imaging technique that enables precise visualizing of individual atoms at the atomic scale, offering essential understanding into surface structures. The simulated STM images for TaS_3, $TaSe_3$ and $TaTe_3$ are illustrated in Fig. 4.1(c). The bright regions represent the chalcogenide atoms located on the outermost surface, respectively.

The dynamical stability of single-layers of TaX_3 are determined through their phonon band dispersions through the whole Brillouin Zone (BZ) and it is presented in Fig. 4.2. It appears from the dispersions that all phonon branches are free from any imaginary frequencies which shows the dynamical stability of free-standing TaX_3 layers. Increasing the atomic number of chalcogen atoms in the TaX_3 nanosheets resulted in phonon modes with smaller frequency ranges, indicating reduced group velocity while maintaining the

general pattern of dispersions. The crystal structures of the 24-atom primitive cell of TaX_3 possesses 3 acoustical and 69 optical phonon branches none of which are degenerate at the Γ point due to the structural anisotropy of the structures. The frequency of the highest optical branch is found to be 485, 275, and 202 cm^{-1} for TaS_3, $TaSe_3$ and $TaTe_3$, respectively. The dispersive nature of the highest optical branches in TaX_3 structures is due to the presence of surface chalcogen atoms. In contrast, bulk structures, which lack surface atoms, exhibit localization and flat branches in the highest optical modes. When transitioning from TaS_3 to $TaTe_3$, the force constants decrease as the chalcogen atom becomes heavier, indicating weaker bonds formed by the heavier chalcogenide atom. Therefore, soft crystals composed of heavier chalcogenide atoms exhibit significant phonon softening in their spectrum, as illustrated in the Fig. 4.2. The dominant vibrations in the phonon modes are found to occur in the out-of-plane direction, specifically the outermost chalcogenide (S-S, Se-Se, and Te-Te) pairings. Larger atomic bond lengths lead to a higher dielectric constant, causing a more significant change in polarizability in the crystal when exposed to light. The increase in Raman activity of the phonon modes from TaS_3 to $TaTe_3$ is due to the higher macroscopic static dielectric constants.

4.2. Electronic and Optical Properties

Electronic band structure and the corresponding partial density of states (PDOS) are calculated in order to investigate the electronic features of single-layer TaS_3, $TaSe_3$ and $TaTe_3$, respectively. As shown in Fig.4.3, single-layer TaX_3 structures exhibit metallic behavior unlike TiX_3 and ZrX_3 which belong to the same material group. The electronic states around the Fermi level are predominantly influenced by tantalum atoms rather than chalcogenide atoms. It is the presence of tantalum that imparts metallic character to TaX_3 structures.

The GGA-PBE approximation is employed to investigate the light-matter interaction and optical properties of single-layer TaX_3 structures, as depicted in Figs. 4.4(a-c). The simulation of absorption coefficient, reflectance, and transmittance spectra is achieved by calculating the frequency-dependent complex dielectric function. To begin with, the obtained real (ε_1) and imaginary (ε_2) components of the dielectric function are utilized to compute the refractive index (n) and extinction coefficient (κ). Furthermore, absorption coefficient $\alpha(\omega)$, reflectance R(ω) and transmittance T(ω) spectra were predicted. To comprehend the impact of dipole orientation on the optical response of the structure, both in-plane and out-of-plane light polarizations are taken into account. The

TaX_3 nanosheet exhibits anisotropic optical properties due to its anisotropic geometry along the x-, y-, and z-axis. This anisotropy is observed when the light polarizations are aligned with the in-plane directions ($E||x$ and $E||y$) as well as the out-of-plane direction ($E||z$). The imaginary part of the dielectric constant ($Im[\varepsilon]$ of the TaS_3, $TaSe_3$,

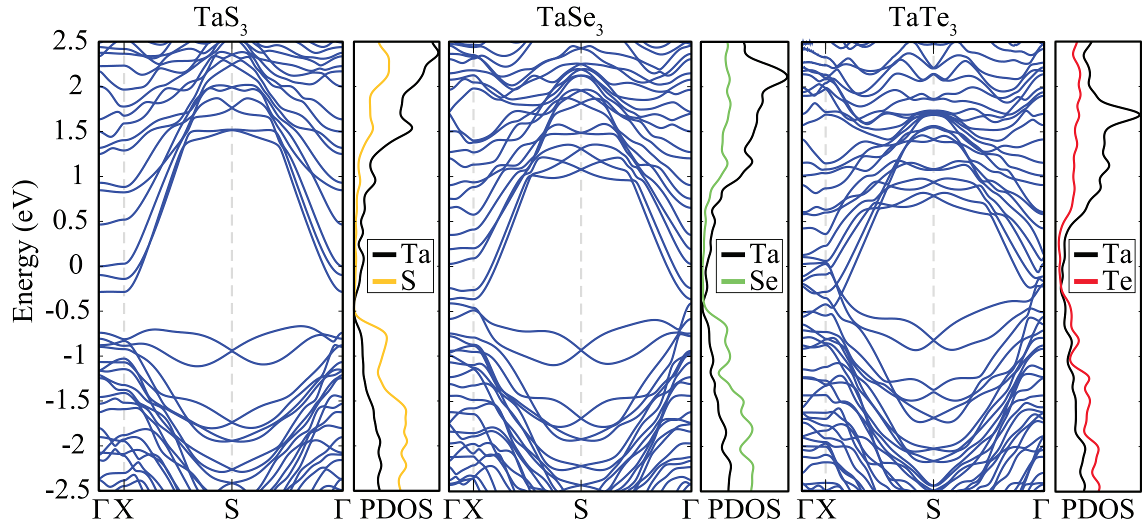

Figure 4.3. (a) The calculated electronic band structures of TaS_3, $TaSe_3$ and $TaTe_3$ single-layers with (b) corresponding partial density of states.

and $TaTe_3$ structures versus photon energy for all polarization directions are shown in Fig. 4.4(a-c), respectively. Next, we examine the optical absorption coefficient of single-layer TaX_3 structures, which denotes the extent to which a material can absorb light of a particular energy (or wavelength) before it can no longer permeate the material. The absorption coefficients of the TaS_3, $TaSe_3$, and $TaTe_3$ are showed in Fig. 4.4(a-c), respectively. The optical absorption profiles of the structures exhibit anisotropic character. The TaX_3 nanosheet exhibits a significant difference in optical absorption in different directions, making it suitable for application in optoelectronic nanodevices that rely on direction-dependent properties. Unlike the strong absorption that occurs within the plane, out-of-plane absorption is significantly weaker due to the enhanced quantum effects in the 2D state. Such effects induce a reduction in the intensity of dipole oscillations along the direction perpendicular to the normal of the sheet. The reflectivity of single-layers of TaX_3 are illustrated in Fig. 4.4(a-c), respectively.

The in-plane reflectivity of the TaX_3 are considerably greater than its reflectivity along out-of-plane direction. Conversely, the transmittance of the TaX_3 materials in the out-of-plane direction is considerably greater than its transmittance in the in-plane orientation. Maximum reflectivity for TaS_3 and $TaSe_3$ along in-plane and out-of-plane polarizations are obtained in the energy range between 3-4 eV. For $TaTe_3$, the maximum

reflectivity is attained in the energy range of 2-3 eV for the x- and z-directions, and in the range of 0-1 eV for the y-direction. Our simulations demonstrate that the reflectivity of single-layer TaX_3 along the out-of-plane polarization direction is lower than that along the in-plane direction. The transmittance spectrum calculation reveals that the transmis-

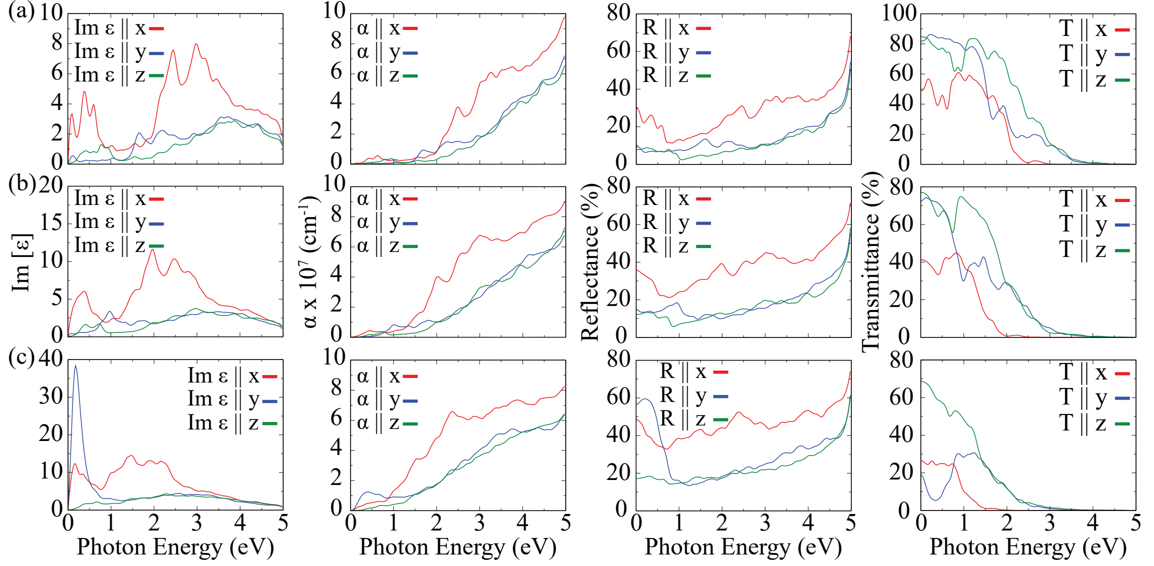

Figure 4.4. Calculated in- and out-of-plane component of the imaginary parts of the dielectric function, absorption, reflectance, and transmittance spectra as a function of photon energy for single-layers (a) TaS_3 (b) $TaSe_3$ and (c) $TaTe_3$ crystal structure.

sion rate remains almost 0% in both the out-of-plane and in-plane directions within the energy range of 4 to 5 eV, which can be attributed to the metallic character of the structures. The optical characteristics of the $TaTe_3$ structure display anomalies in comparison to TaS_3 and $TaSe_3$. The difference mainly stems from the electronic band structure of $TaTe_3$ where the increasing atomic weight of the chalcogenide atoms causes the band gaps between electronic states to close, resulting in degeneracy. The presented results reveal attractive anisotropic optical characteristics of the TaS_3, $TaSe_3$, and $TaTe_3$ structures. The anisotropic optical properties of TaX_3 layers show great potential for developing new optoelectronic nanodevices that can take advantage of their anisotropic features, particularly for polarization-sensitive photodetectors.

4.3. Elastic Properties

Linear-elastic parameters describe how a material responds to small stresses by deforming within the linear range. For monoclinic structure, the Born-Huang criteria of

mechanical stability in terms of the elastic strain tensor constants, C_{11}, C_{22}, C_{12}, and C_{66}, should satisfy the following conditions: $C_{66} > 0$ and $C_{11} + C_{22} - 2C_{12} > 0$.[190] According to our calculated values for C_{11}, C_{22}, C_{12}, and C_{66}, single-layers of TaX_3

Table 4.2. For single-layer TaS_3, $TaSe_3$ and $TaTe_3$ structures, the relaxed ion elastic coefficients C_{ij} the corresponding in-plane stiffness C, and Poisson ratio υ, along a and b direction.

	C_{11} (N/m)	C_{12} (N/m)	C_{21} (N/m)	C_{22} (N/m)	C_{66} (N/m)	C_a (N/m)	C_b (N/m)	υ_{ac}	υ_{zz}
TaS_3	105	21	21	169	40	102	165	0.12	0.20
$TaSe_3$	102	18	18	159	34	100	155	0.11	0.18
$TaTe_3$	94	14	14	130	28	92	128	0.11	0.15

display mechanical stability indicating that TaX_3 crystal structures preserves their shape under small loads. The linear-elastic features of the mechanically stable TaX_3 layers can be represented by two independent constants, namely the in-plane stiffness (C) and the Poisson ratio (υ). The in-plane stiffness is a property that indicates the rigidity or flexibility of a material. It is influenced by the geometry of structure and the strength of the atomic connections between the individual atoms. As seen in Fig. 4.5(b) and (c), elastic properties of TaX_3 structures are highly orientation-dependet. As listed in Table 4.2 for

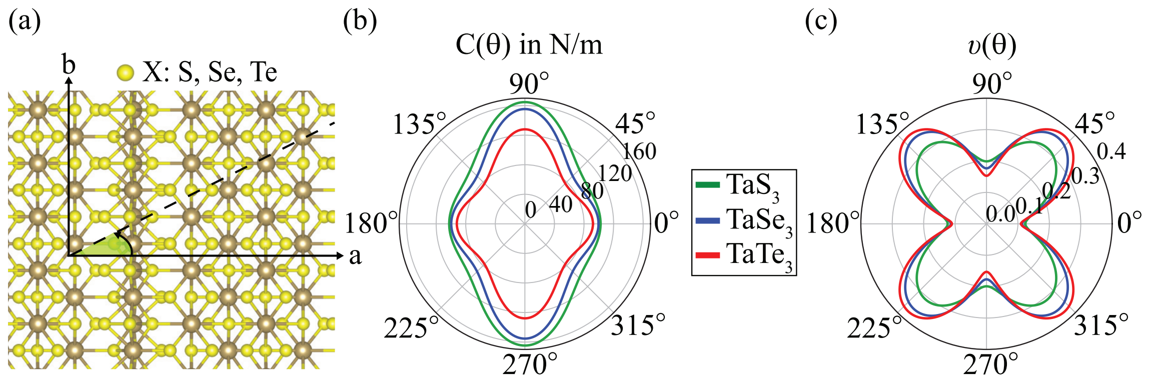

Figure 4.5. (a) Schematic representation of the orientation angle (θ). (b) The angle-dependent in-plane stiffness (C) and (c) that of Poisson ratio (υ) of TaX_3 layers.

TaS_3, $TaSe_3$ and $TaTe_3$, the C values are 102/165, 100/155, and 92/128 in the parallel and perpendicular direction, respectively. The larger the bond lengths result in the smaller the in-plane stiffness. When the in-plane stiffness decreases, the restoring forces in the structure become effective over a shorter range of applied strain, resulting in a smaller harmonic strain zone for soft materials. The TaX_3 structures show greater resistance to strains in the y-direction than in the x-direction. The structures have quasi-1D ribbons

aligned in the x-direction and strongly linked connections in the y-direction. It causes less strength in the x-axis but leads to more durable structures in the y-axis. Moreover, the Poisson ratio characterizes a response of material in the perpendicular direction to an external uniaxial strain leading to longitudinal extension. Poisson ratios exhibit direction-dependent characteristics, displaying small changes in the parallel direction from single-layer TaS_3 to $TaTe_3$ (0.12 for TaS_3, 0.11 for $TaSe_3$, and 0.11 for $TaTe_3$). Conversely, in the perpendicular direction, the Poisson ratios for TaS_3, $TaSe_3$, and $TaTe_3$ are 0.20, 0.18, and 0.15, respectively. Single-layer TaS_3 exhibits larger responses to the applied stress along the both parallel and perpendicular direction.

CHAPTER 5

ANISOTROPIC SINGLE-LAYER TILTED α-BISMUTHENE

In this chapter, the structural, vibrational, electronic, and elastic properties of single-layer tilted α-Bi and its vibrational spectrum under external uniaxial strain were investigated by means of ab-initio calculations. It was found that free-standing tilted α-Bi is a dynamically and mechanically stable indirect band gap semiconductor possessing in-plane anisotropy. In addition, strain-induced modifications can be identified by means of the Raman spectrum analysis. The rest of paper is organized as follows; Structural, vibrational and thermal properties of tilted α-Bi are presented in Section 5.1. Electronic (Section 5.2), and elastic properties (Section 5.3) of α-Bi are illustrated. In addition, strain characterization via vibrational spectrum is shown in Sec. 5.4.

5.1. Structural and Vibrational Properties

The optimized atomic structure of single-layer α-Bi is shown in Fig. 5.1(a). The α-Bi has a distorted atomic structure which consist of two sub-layers of Bi atoms, which is similar to that of black phosphorus. The α-Bi undergoes structural distortion that the atomic sub-layers become tilted unlike black phosphorus. In addition, α-Bi has par-

Table 5.1. For the optimized free-standing structure of single-layer α-Bi; the in-plane lattice parameters (a and b), tilting between Bi_A and Bi_B atoms (Δh); the atomic bond lengths between A and B type Bi atoms, d^{in}_{A-B}, d^{out}_{A-B}; vertical distance between uppermost and lowermost Bi, t; the cohesive energy per atom, E_{coh}; the work function, Φ; and electronic band gap calculated within HSE06 (E_g^{HSE06}).

	a (Å)	b (Å)	Δh (Å)	d^{in}_{A-B} (Å)	d^{out}_{A-B} (Å)	t (Å)	E_{coh} (eV/atom)	Φ (eV)	E_g^{HSE06} (meV)
α-Bi	4.44	4.87	0.62	3.08	3.02	3.67	2.84	3.55	304

tial sp^2 configuration in contrary to the tetrahedral sp^3 configuration of black phosphorus,[191,192] which is the main reason of the tilting between neighboring sublattices and loss of centrosymmetry. There are two different types of bismuth atoms in α-Bi labeled as Bi_A and Bi_B, which are shown by purple and blue colors, respectively (see Fig. 5.1(a)). Tilt-

ing between Bi_A and Bi_B atoms (Δh) is found to be 0.62 Å. The optimize in-plane lattice parameters (a and b to be 4.44 and 4.87 Å, respectively) reveal the in-plane anisotropic nature of the structure. There exists two types of Bi-Bi bonding which are named as d^{in}_{A-B} and d^{out}_{A-B} are calculated to be 3.08 and 3.02 Å, respectively as listed in Table 5.1.

The spin-polarized calculations reveal the non-magnetic ground state of single-layer α-

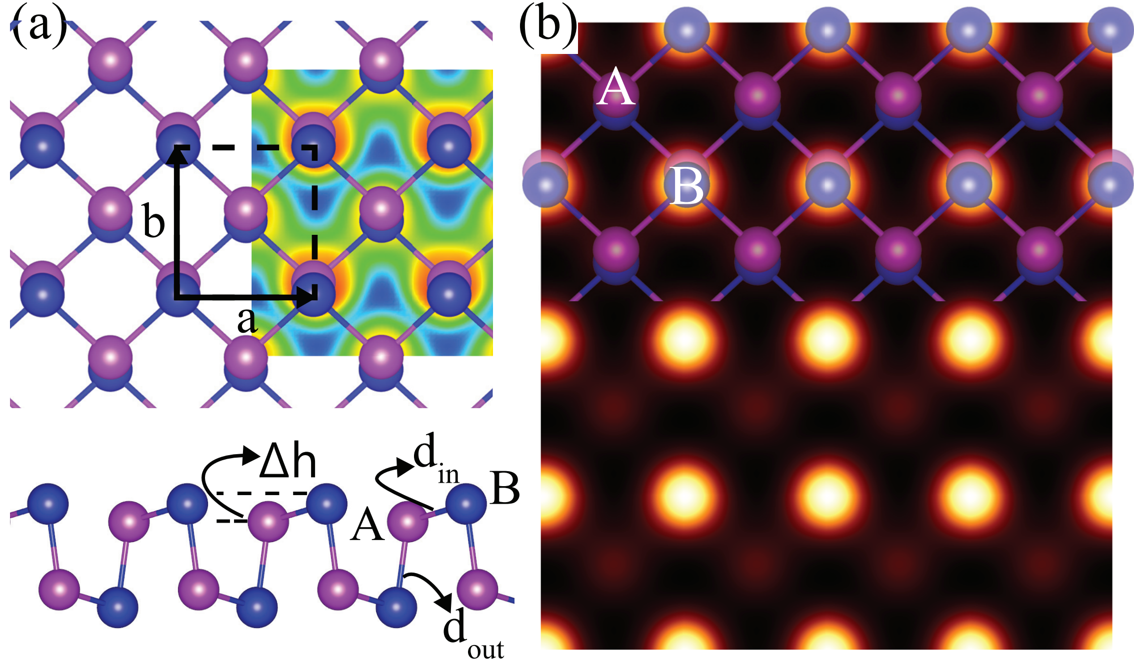

Figure 5.1. For the single-layer α-Bi structure, (a) top and side views of the crystal structure, and (b) simulated STM image. Corresponding electron localization function contour map for the plane containing directly connected top Bi atoms is shown in (a).

Bi. In addition, the thickness (the vertical distance between uppermost and lowermost Bi atoms) of single-layer α-Bi is 3.67 Å. In order to analyze the chemical stability of strength of α-Bi, the cohesive energy per atom, E_{coh}, is calculated to be 2.84 eV/atom which is significantly lower than black phosphorus (3.61 eV/atom). The work function (Φ) is found as 3.55 eV for single-layer α-Bi which is much lower than that of black phosphorus (4.81 eV) indicating that the energy required to remove an electron from α-Bi is much lower as compared to the case of black phosphorus. Moreover, Bader charge analysis shows that upon the formation of α-Bi structure, charge donation occurs from the Bi_B atoms to Bi_A atoms with an amount of 0.05 e^-/Bi_B which indicates the partially covalent character between the individual atoms. To gain deeper understanding of the chemical bonding character in α-Bi structure, the electron localization function (ELF) is examined. Typically, areas with ELF values approaching 1 (red region) suggest strong covalent bonding or presence of lone pair electrons, while lower ELF values indicate delocalization ($\approx$0.5),

ionic bonds, or weak van der Waals interactions. Fig. 5.1(a) display the ELF contour maps for plane containing top Bi_B atom. The small ELF values in regions between Bi

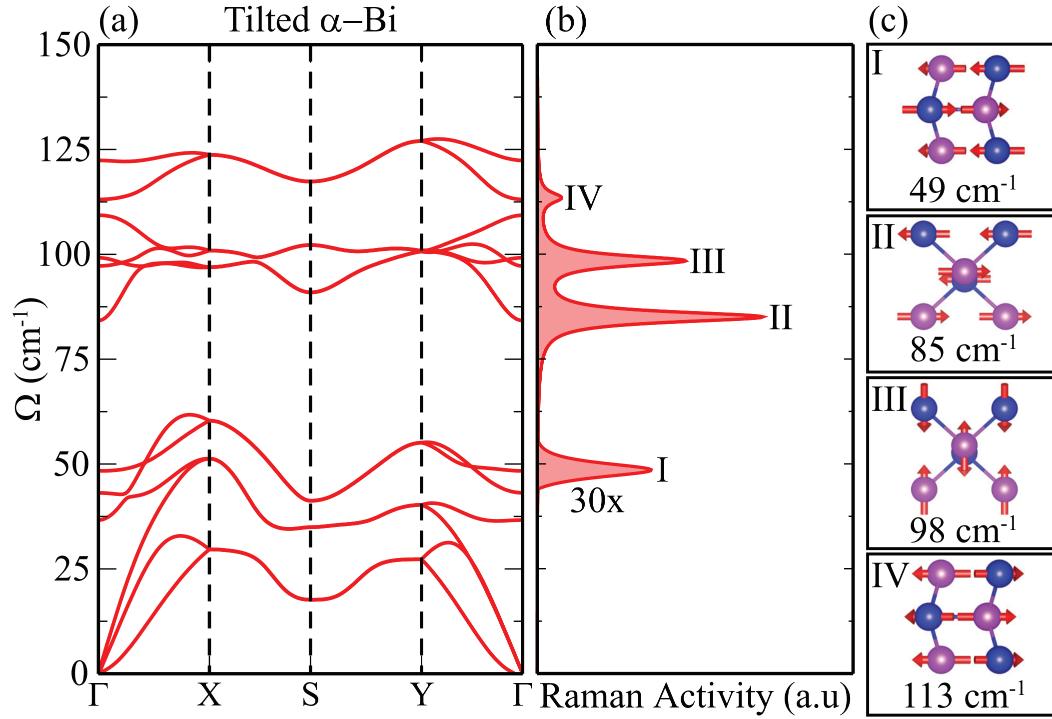

Figure 5.2. (a) The phonon band dispersions, (b) Raman activity of zone-centered vibrations, and the corresponding (c) atomic vibrations of Raman active phonon modes in single-layer α-Bi.

atoms reflect that ionic interactions are almost dominant. Scanning tunneling microscopy (STM) is highly effective imaging method in order to utilize surfaces at the atomic scale. STM technique enables the precise observation of individual atoms on a surface. As presented in Fig. 5.1(b), the Bi_B atoms can be observed as bright spots and thus, single-layer α-Bi has a stripe-like surface characteristic owing to its tilted structure.

The dynamical stability of single-layer α-Bi is determined through its phonon band dispersions and the result is shown in Fig. 5.2(a). It appears from the dispersions that all phonon branches are free from any imaginary frequencies which shows the dynamical stability of the free-standing α-Bi. There are 3 acoustical and 9 optical phonon branches none of which are degenerate at the Γ point due to the structural anisotropy of the structure. The vibrational frequency of the highest optical phonon branch at the Γ point is found to be 122 cm^{-1} which may give information about the Bi-Bi bond strength. In order to have detailed inofmration about the vibrational characterics of the optical branches, the first-order off-resonant Raman spectrum of α-Bi is calculated and the results are presented in Fig. 5.2(b). The calculated Raman spectrum of single layer α-Bi reveals that four optical phonon modes are Raman active and possess non-zero Raman activity. Such

Raman active modes are labeled as I-IV and their corresponding vibrational eigenvectors are shown in Fig. 5.2(c). The highest activity is calculated for the mode-II whose frequency is found to be at 85 cm^{-1}. The phonon mode-II has a pure in-plane vibrational character, in which Bi$_A$ and Bi$_B$ vibrate oppositely. In contrast, the modes I and IV possess out-of-plane vibrational characteristics, whose frequencies are found to be at 49 and 113 cm^{-1}, respectively. The mode-I arises from the out-of-phase vibrations of the top and bottom Bi$_A$-Bi$_B$ pairs. In addition, the mode-IV presents the in-phase vibration of the top and bottom Bi$_A$-Bi$_B$ pairs while each Bi$_A$ and Bi$_B$ atoms vibrate out-of-phase. Finally, the phonon mode-III having frequency of 98 cm^{-1} is found to exhibit in-plane vibrational character, in which Bi$_A$ and Bi$_B$ atoms vibrate oppositely.

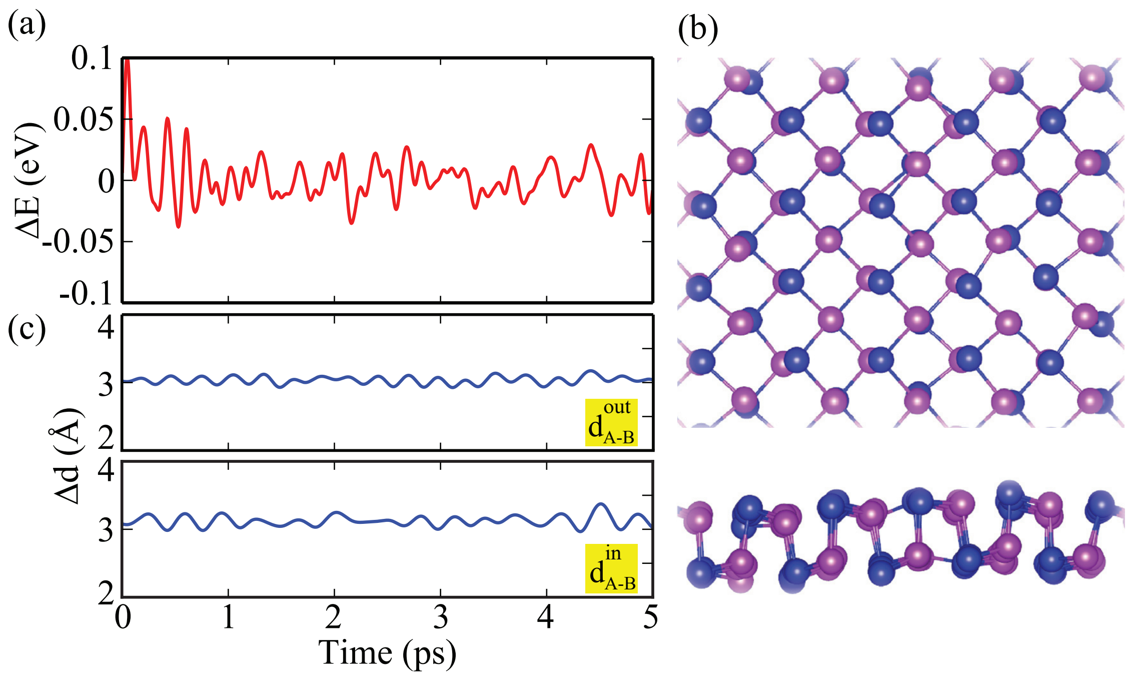

Figure 5.3. For the QMD simulations of α-Bi structure, (a) total energy fluctuations, (b) the crystal structure at 300K, and (c) variation in bond lengths of d$^{out}_{A-B}$ and d$^{in}_{A-B}$ as a function of total simulation time at room temperature.

In addition to the dynamical stability analysis of α-Bi, we further investigate the thermal stability of the free-standing layer by performing ab-initio Quantum Molecular Dynamics (QMD) simulations at room temperature. The total time for our simulation is considered to be 5 picoseconds (ps) with time steps of 2 femtoseconds (fs) between each step. The variations in total energy of the structure is shown in Fig. 5.3(a) and it is found that the average fluctuations reside between $\pm$30 meV which is the range for a 64-atom supercell, indicating that the total energy variation per Bi-atom is less than 1 meV. Apparently, the total energy variation per atom of 1 meV reveals the thermal stability of the single-layer α-Bi. The crystal structure of α-Bi at room temperature at the end of the

5 ps simulation is also shown in Fig. 5.3(b). It is seen that there exists tiny distortions in the lattice with no structural reconstructions. Therefore, the crystalline morphology of α-Bi is preserved around room temperature. In addition, fluctuations in bond length of

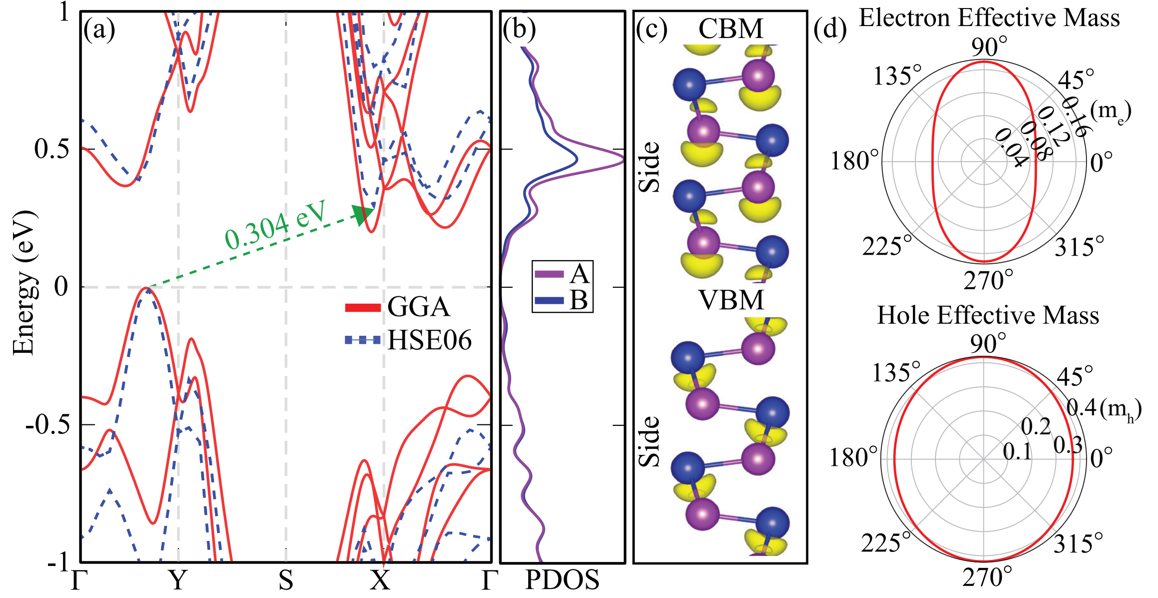

Figure 5.4. (a) The calculated electronic band dispersions (GGA and HSE06) of single-layer α-Bi structure. The Fermi energy (E_F) level is set to the top of valence states. The blue dashed line and red solid lines represent the band structures calculated within HSE06 and GGA, respectively. (b) Corresponding partial density of state of α-Bi and (c) atomic orbitals contributing to the VBM and CBM states. Isosurface value for the atomic orbitals in (c) is taken to be $2.5x10^{-5}e^{-}/^{3}$. (d) Effective masses of electrons and holes for different orientation angles.

the two different types, namely d^{in}_{A-B} and d^{out}_{A-B}, are presented in Fig. 5.3(c). It appears from the graphs that both bonds fluctuate around their equilibrium positions, an indication of the thermal stability of the structure.

5.2. Electronic Properties

Electronic features of α-Bi are investigated by means of the electronic band structure and the corresponding partial density of states (PDOS). As shown in Fig. 5.4(a), single-layer α-Bi exhibits semiconducting behavior with an indirect electronic band gap of 304 meV. The valence band maximum (VBM) state resides between the Γ and the Y high symmetry points while the conduction band minimum (CBM) lies in between the S and the X points of the BZ. PDOS plots reveal that top valence states of α-Bi is composed of partial contributions from Bi_A and Bi_B atoms the bottom conduction states are

significantly dominated by Bi_A atoms. In order to understand the atomic-orbital contributions to the edge electronic states, the band decomposed charge densities are calculated and the results are presented in the Fig. 5.4(c). It is shown that a hybridization between the in-plane orbitals of Bi_A and Bi_B atoms occurs in the VBM state. However, the charge distribution in the CBM state is distributed only around the Bi_A atoms.

We further analyze both the electron and hole effective masses of single-layer α-Bi by considering the in-plane anisotropy of the structure. The effective masses are calculated by parabolic fitting of the band extrema using the formula E=$\hbar^2 k^2/2m^*$. The hole effective masses along the Γ and the Y directions of the VBM are calculated to be 0.331 and 0.467 m_0, respectively, where m_0 is the free electron mass. The hole effective masses were reported to be 1.140 and 0.182 m_0 for the black phosphorus[57] indicating the higher anisotropic nature of the structure. In addition, the electron effective masses are 0.112 and 0.152 m_0 along the $S-X$ and the $X-\Gamma$ directions, respectively, which are smaller than those for black phoshporus (0.846 and 0.166 m_0).[57] In addition, the in-plane anisotropy of the structure of α-Bi is combined with the effective masses by plotting the orientation-dependent behavior of the masses using the formula:

$$m^* = \frac{1}{[(cos^2\theta/m^*_{zz}) + (sin^2\theta/m^*_{ac})]} \tag{5.1}$$

where θ is the angle between an arbitrary direction and the zigzag orientation and the coefficients m^*_{zz} and m^*_{ac} represent the effective masses along the zigzag (ZZ) and armchair (AC) directions, respectively. It is shown that both electron and hole effective masses display decreasing trend along the ZZ direction, which is much greater for the electron effective mass. Moreover, behavior of holes is found to be more isotropic as compared to that of electrons as a consequence of the anisotropy of the CBM states (see Fig. 5.4(d)).

5.3. Elastic Properties

Linear-elastic parameters characterize the ability of a material to deform under small loads. For orthorombic crystals, the Born-Huang criteria[183] gives detailed information about the mechanical stability of the material. The linear-elastic parameters obtained from the elastic tensor, namely C_{11}, C_{22}, C_{12}, and C_{66}, should satisfy the following conditions: $C_{66} > 0$ and $C_{11}C_{22} - C_{12}^2 > 0$.[193] According to our calculated values for C_{11}, C_{22}, C_{12}, and C_{66} (see Table 5.2), single-layer α-Bi exhibits mechanical stability indicating

that α-Bi preserves its shape unders small strains. For the mechanically stable α-Bi, the

Table 5.2. The relaxed-ion elastic coefficients, C_{ij}; and the corresponding in-plane stiffness, C; and Poisson ratio, υ; along ZZ and AC directions in single-layer α-Bi.

	C_{11} (N/m)	C_{12} (N/m)	C_{21} (N/m)	C_{22} (N/m)	C_{66} (N/m)	C_{ac} (N/m)	C_{zz} (N/m)	υ_{ac}	υ_{zz}
α-Bi	39	17	17	19	19	24	11	0.90	0.43

linear-elastic properties can be analyzed in terms of two independent constants, namely the in-plane stiffnes (C) and the Poisson ratio (υ). The orientation dependency of both C and υ are obtained using the equations given below:

$$C(\theta) = \frac{(C_{11}C_{22} - C_{12}^2)}{C_{22}cos^4(\theta) + Acos^2(\theta)sin^2(\theta) + C_{11}sin^4(\theta)}$$

$$\upsilon(\theta) = \frac{C_{12}cos^4(\theta) - Bcos^2(\theta)sin^2(\theta) + C_{12}sin^4(\theta)}{C_{22}cos^4(\theta) + Acos^2(\theta)sin^2(\theta) + C_{11}sin^4(\theta)} \quad (5.2)$$

where the numbers $A=(C_{11}C_{22}-C_{12}^2)/C_{66}-2C_{12}$ and $B=C_{11}+C_{22}-(C_{11}C_{22}-C_{12}^2)/C_{66}$ are used for simplifying the equations. Note that the ZZ and AC values of both constants can be calculated for the angles 0 and 90 degrees, respectively. As presented in Fig. 5.5, the in-plane stiffness is found to be 24 and 11 N/m for the ZZ and AC directions, respectively. Apparently, α-Bi possesses ultra soft behavior along the AC orientation and it becomes quite stiffer as the external strain is applied along the ZZ direction. As the external strain is applied with an angle around 40 degrees, the in-plane stiffness is maximized and becomes 43 N/m. As compared to the stiffness values reported for the other mono-elemental single layers such as graphene (330 N/m),[11] silicene (62 N/m),[194] and germanene (48 N/m).[194] α-Bi has much softer character than graphene and comparable stifness with those of silicene and germanene. Moreover, the reported orientation-dependent stiffness values for single layers of black phoshporus (39 and 92 N/m)[58] and black arsenic (20 and 55 N/m)[58] for the AC and ZZ orientations, respectively, reveal the less anisotropic nature of α-Bi.

Poisson ratio, represents the perpendicular response of a material to an external uniaxial strain and is known to be positive for most of the materials. Most materials have tendency to compress in one direction when expanded in the perpendicular direction. The υ values of single-layer α-Bi along the two main orientations are calculated to be 0.90 and 0.43 for the ZZ and AC directions, respectively. The high υ values of α-Bi indicate its strong ability to preserve the equilibrium area. As compared to the values for graphene (0.16),[194] silicene (0.30),[194] and germanene (0.33),[194] α-Bi is more responsive

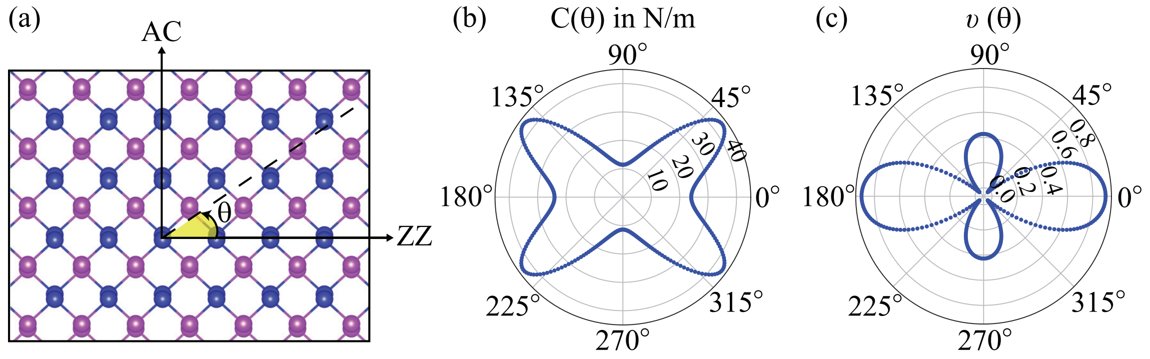

Figure 5.5. (a) Schematic representation of the orientation angle θ, (b) the angle-dependent in-plane stiffness (C) and (c) that of Poisson ratio (υ).

to the external uniaxial strains. Similar to the high υ values of single-layer α-Bi, black arsenic was reported to exhibit 0.33 and 0.91 for the AC and ZZ orientations.[58] The poisson ratio along the orientation angle of 45 degrees is found to be negative (-0.02) for α-Bi, which indicates the auxetic behavior of the material. Such behavior reveals that as α-Bi is exposed to an external strech along the 45 degrees, the structure gets streched along the perpendicular direction. The negative Poisson ratio of α-Bi (-0.02) is predicted to be lower than well-known auxetic materials such as black arsenic (-0.093),[195] penta-graphene (-0.078),[196] and black phosphorus (-0.027).[56]

5.4. Strain Characterization via Vibrational Spectrum

Raman spectroscopy is an efficient experimental methodology not only to demonstrate the correct structural phase but also to understand whether the material is exposed to any external strain or not. Although, strain can be operated controllably on a material, it is also possible that strain may internally occur as a result of substrate effect. Therefore, it is critical to distinguish the direction and the strength of the strain by analyzing the vibrational properties of the materials. In this section, the effect of uniaxial strains on the phononic properties of single-layer α-Bi are discussed by means of the phonon band dispersions and the corresponding Raman spectra. The uniaxial strains are applied on the α-Bi structure along the two main orientations, namely the ZZ and AC directions, between the $\pm5\%$ strengths. As the compressive and tensile strains are applied, all the atoms are fully relaxed except for the lattice parameters. First of all, the dynamical stability of single-layer α-Bi is obtained for the higher limits of both compressive and tensile

strains. The corresponding phonon band dispersions are presented in Figs. 5.6(a) and (b).

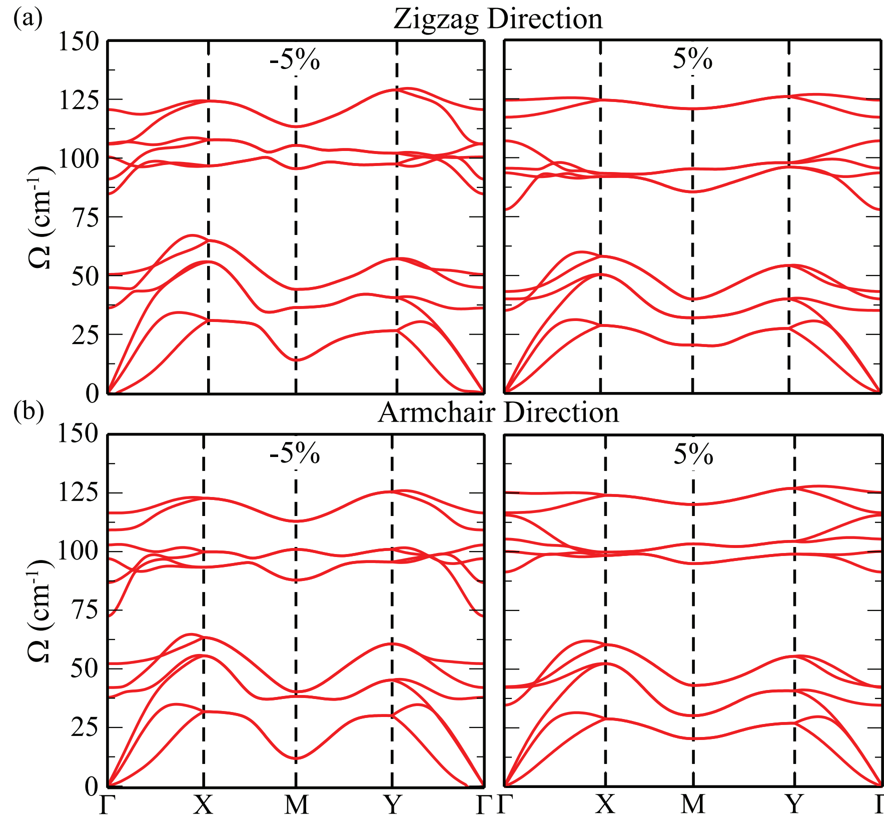

Figure 5.6. The phonon band dispersions under $\pm 5\%$ strains along the (a) ZZ and (b) AC directions.

Apparently, single-layer α-Bi exhibits dynamical stability by means of the phonons as it is either compressed or streched up to 5% strains. As the Bi-Bi bond distances vary with the type and the strength of the applied strain, there exist phonon softening/hardening depending on the type of the applied strain. It feasible to observe such phonon shifts through the analysis of Raman features of α-Bi. The frequency shifts result from the strains can be detected by the Raman spectra. In addition, in order to understand the strain-behavior of each phonon mode, the corresponding mode Gruneissen parameters are also calculated using the equation:

$$\gamma(q) = -\frac{a_0}{2\omega_0(q)}\left[\frac{\omega_+(q) - \omega_-(q)}{a_+ - a_-}\right] \tag{5.3}$$

where a_0 is the relaxed (unstrained) lattice parameter, $\omega_0(q)$ is the unstrained phonon frequency at wave vector q, $\omega_+(q)$ and $\omega_-(q)$ are the phonon frequencies under tensile and compressive uniaxial strains, respectively, and a_+ and a_- are the strained and the compressed lattice parameters, respectively. The calculated Raman spectra for each strain type and the corresponding strength are presented in Figs. 5.7(a) and (b). The Raman

active phonon mode, labeled as mode-I, is shown to exhibit phonon softening (hardening) via applied tensile (compressive) strains independent of the strain direction. The calculated mode Gruneissen parameters of mode-I (0.20 and 0.30 for the ZZ and AC strain directions, respectively) indicate that the mode is more sensitive to the applied uniaxial strain along the AC direction since the central Bi_A-Bi_B pair vibrate out-of-phase with the surrounding Bi_A and Bi_B atoms. The frequency of the mode-I is found to vary between

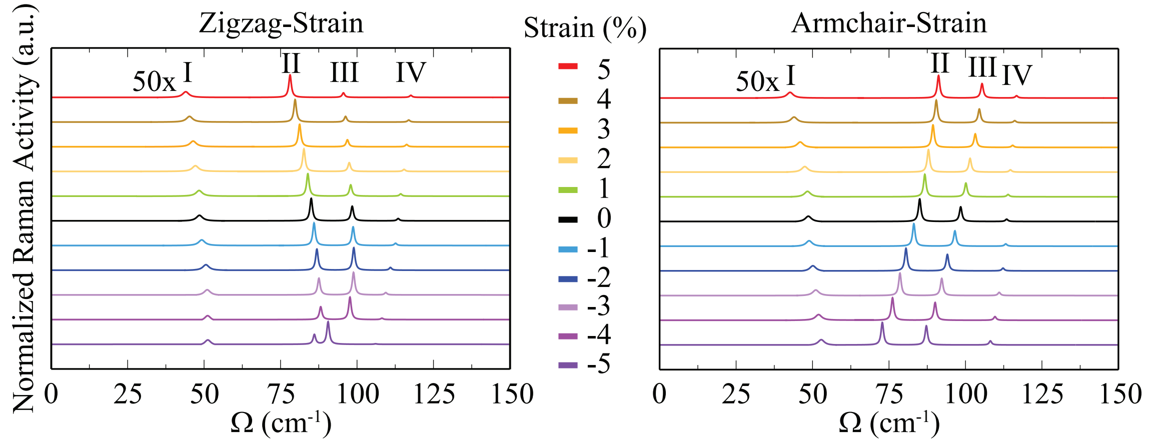

Figure 5.7. Raman spectra of single-layer α-Bi under the effect of (a) ZZ and (b) AC strains.

51-44 and 53-43 cm^{-1} for the ZZ and AC strains, respectively. The phonon mode-II is shown to display similar behavior with that of mode-I under ZZ-strain while it exhibits phonon softening (hardening) via applied compressive (tensile) strains. Such contrary behavior can be used to identify the direction of the applied strain on the structure. The opposite behavior of the mode-II under ZZ and AC strains is also predicted through the mode Gruneissen parameters for the two strain directions. The γ is found to be 0.23 and -0.41 for the ZZ and AC strain directions, respectively. Apparently, the variation in frequency along the ZZ strain (86-78 cm^{-1}) is almost half of that along the AC strain (91-73 cm^{-1}). Although, individual atoms vibrate along the ZZ direction, as the uniaxial strain is applied along AC direction the central Bi_A and Bi_B atoms separate along the AC direction. A similar behavior is predicted for the mode-III which has in-plane characteristic along the AC direction. The γ is calculated to be 0.10 and -0.41 for the ZZ and AC strain directions, respectively indicating that the AC strain has similar impact on both mode-II and mode-III. As compared to those for the mode-II, the frequency variation is smaller for the mode-III (96-91 cm^{-1}) along the ZZ strain and similar (105-87 cm^{-1}) along the AC strain. Finally, the mode-IV is found to display phonon softening (hardening) under compressive (tensile) strains both directions. Such anomalous behavior can be attributed to the change in the bond length under applied strains that the d^{out}_{A-B} gets smaller as the

lattice is stretched and it gets larger as the lattice is compressed. The corresponding γ value is found to be almost the same for the two strain directions (-0.17 and -0.18 for the ZZ and AC directions). In order to identify the direction of the uniaxial strain, the opposite behaviors of the modes II and III under ZZ and the AC strains can be used. In addition, the frequency difference between the two modes can also be considered that for the ZZ strain the difference gets larger (smaller) under tensile (compressive) strains. Similar anisotropic behavior in vibrational spectrum was observed for BP.[197] It was reported that three Raman active modes (A_g^1, B_{2g}, and A_g^2) of BP display red shift for A_g^1 mode and blue shift for B_{2g}, and A_g^2, in armchair direction under compressive strain. Conversely, A_g^1 shifts blue, and B_{2g}, and A_g^2 modes shift red in tension. In zigzag direction strained, B_{2g}, and A_g^2 modes exhibit red shift, and A_g^1 shows blue shift under tension. Under compression B_{2g}, and A_g^2 modes shift blue, while A_g^1 shifts red. Apparently, in anisotropic materials theoretical support of the experimental observations on the strain type and direction is quite important.

CHAPTER 6

EDGE- AND WIDTH-DEPENDENT ANISOTROPY IN ULTRA-NARROW 1D MAGNETIC MANGANESE PHOSPHORUS TRI-SULFIDE ($MNPS_3$) NANORIBBONS

Until now, we have explored 2D anisotropy. Now, we are shifting our focus to 1D anisotropy arising from edge and width variations in the magnetic $MnPS_3$as they undergo dimensional reduction. Despite numerous investigations on the bulk and 2D structures of $MnPS_3$, studies on one dimensional (1D) form of $MnPS_3$ crystal has not been reported up to date. In this chapter, 1D nanoribbon (NR) forms of ultra-thin $MnPS_3$ were investigated by means of the structural, magnetic, and electronic properties by using Density Functional Theory (DFT)-based ab-initio calculations. The edge type and width-dependent electronic and magnetic features were discussed in terms of the magnetic orders, electronic band structures, and STM images. The rest of paper is organized as follows; Structural, magnetic, and electronic properties of 2D single-layer $MnPS_3$ are presented in Sec. 6.1. In Sec. 6.2, the edge and width dependent properties of different type of $MnPS_3$ NRs along AC and ZZ directions are presented.

6.1. 2D Single-layer of $MnPS_3$

2D single-layer form of $MnPS_3$ consists of three different types of atoms (Mn, P, and S atoms) which are packed in a hexagonal lattice structure. Magnetic Mn^{+2} cations in the crystal structure are arranged in a honeycomb lattice, and are octahedrally coordinated to six sulfide atoms with P-P dimers located vertically in the middle of the hexagonal plane (see Fig. 6.1(a-d)). In addition, the P-P dimers are coordinated in a tetrahedral manner with three sulfur atoms to form a $[P_2S_6]^{4-}$ bi-pyramid. The magnetic ground state of single-layer $MnPS_3$ is determined through the total energy analysis for the considered four spin configurations shown in Fig. 6.1(a-d). Four different magnetic states are named as ferromagnetic (FM), Néel, zigzag, and stripy antiferromagnetic (AFM) states. In the Néel AFM state, Mn atoms arranged antiferromagneticly along both zigzag (ZZ) and armchair (AC) directions. The zigzag AFM state represents that Mn atoms are aligned ferromag-

netically along the ZZ direction and antiferromagnetically along the AC direction. In

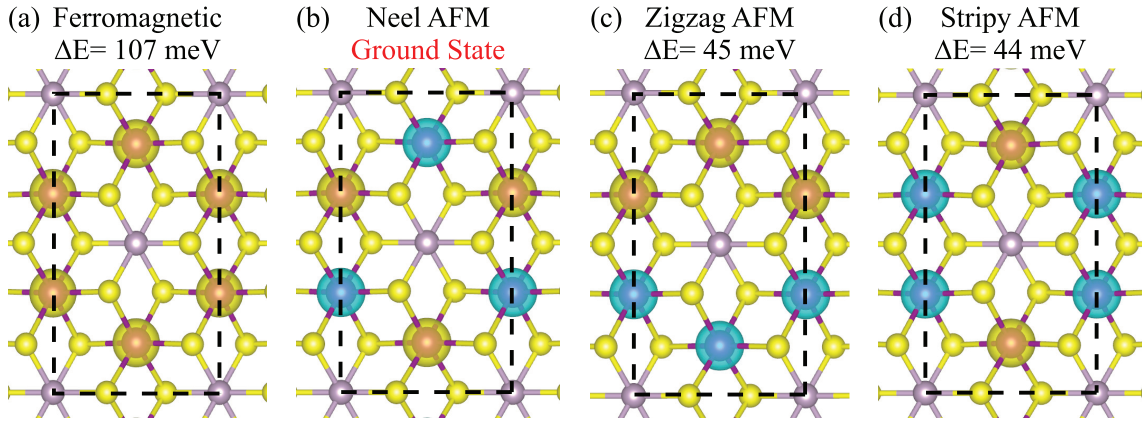

Figure 6.1. Spin arrangements of (a) FM, (b) Néel, (c) zigzag, and (d) stripy AFM. The yellow, and blue colors represent the spin-up and spin-down state Mn atoms, respectively.

the case of stripy AFM state, Mn atoms exhibit AFM alignment in the ZZ direction and FM alignment in the AC direction. The total energy calculations reveal that Néel type AFM aligned spins on Mn atoms, where each magnetic site is anti-aligned with its nearest neighbors, is energetically favorable over the other three magnetic states. The energy differences (ΔE) with respect to the FM, zigzag-, and stripy-AFM states are calculated to be 107, 45, and 44 meV per formula unit, respectively as shown in Fig. 6.1(a-d). The magnetic moment per Mn atom is found to be 5 μ_B due to the presence of unpaired electrons in the $3d$ orbitals. As listed in Table 6.1, the optimized in-plane lattice parameters of 2D $MnPS_3$ for the Néel AFM state are found to be a=b=6.07 Å, slightly larger than bulk form (6.06 Å). The bond lengths between the Mn-S and P-S atoms are found to be 2.63, and 2.03 Å, respectively, which is consistent for P-S found in bulk, while Mn-S is slightly smaller than that of bulk, and the Mn-Mn distance is calculated as 3.50 Å. In addition, the vertical distance between the outermost S atoms, which is defined as the thickness of single-layer $MnPS_3$, is found to be 3.31 Å. The Bader charge analysis indicates that when single-layer of $MnPS_3$ is formed, Mn and P atoms donate electrons to S atoms. Specifically, each Mn and P atom donates 1.2 and 1 e^-, respectively, and each S atom gains 0.7 e^- from the neighboring Mn and P atoms, which is also the case when the bulk structure is found, indicating partially covalent bonding character between the individual atoms. Using the local potential distribution along the out-of-plane direction, the work function is calculated to be 6.07 eV, which is slightly smaller than that of bulk $MnPS_3$ (6.13 eV), using the formula; $\phi = E_{vac} - E_F$, where ϕ represents the work function, E_{vac} denotes the vacuum energy, and E_F is the Fermi energy. The work func-

tion of $MnPS_3$ is slightly higher as compared to that of well-known 2D materials such as MoS_2 (5.10 eV), h-BN (4.70 eV),[198] CrI_3 (5.35 eV),[199] VSe_2 (5.52 eV),[200] implying high chemical stability of the surface of $MnPS_3$. Cohesive energy gives information

Table 6.1. For the single-layer 2D and bulk $MnPS_3$: the optimized in-plane lattice parameters (*a and b*), the atomic bond lengths between individual atoms (d_{Mn-S}, d_{P-S}), vertical distance between uppermost and lowermost S atoms (t), the amount of donated electron for manganese (ρ_{Mn}), and phosphor (ρ_P), the amount of received electron for sulfur (ρ_S), the cohesive energy per atom (E_{coh}), electronic band gap energy (E_g), and the work function, (ϕ).

	a (Å)	b (Å)	d_{Mn-S} (Å)	d_{P-S} (Å)	t (Å)	ρ_{Mn} e^-	ρ_P e^-	ρ_S e^-	E_{coh} (eV/atom)	E_g (eV)	ϕ (eV)
2D Néel-AFM	6.07	6.07	2.63	2.03	3.03	-1.2	-1	+0.7	4.40	2.50	6.07
Bulk Néel-AFM	6.06	6.06	2.62	2.03	-	-1.2	-1	+0.7	4.43	2.38	6.13

about structural stability and the energy needed to separate individual atoms in a structure and bring them into a vacuum as free atoms. The cohesive energy E_{coh} of the single-layer $MnPS_3$ structure is calculated as 4.40 eV/atom by using the following equation; $E_{coh} = \frac{1}{m+n+l}[mE_{Mn} + nE_P + lE_S - E_{structure}]$, where m, n and l stand for the total number of Mn, P, and S atoms, respectively. E_{Mn}, E_P, E_S are the total energy of each isolated atom Mn, P, and S atom and $E_{structure}$ is the total energy of the corresponding ultra-thin structure. The cohesive energy of 2D $MnPS_3$ is slightly smaller than that of the bulk structure (4.43 eV). The cohesive energy of CrI_3 (3.05 eV/atom), $Cr_2Ge_2Te_2$ (3.21 eV/atom), and CrSBr (4.11 eV/atom) are lower than that of $MnPS_3$, which indicates the stronger bond formations in $MnPS_3$.

It is crucial to investigate the magneto-crystalline anisotropy in magnetic materials for determining the stability of magnetization against thermal excitation. The non-collinear calculations are carried out for 2D Néel-AFM MnP_3 structure in order to investigate the easy-axis of single-layer $MnPS_3$. Magnetic anisotropy energy (MAE) per conventional cell is calculated by using the equation $E_{MAE} = E_{\parallel} - E_{\perp}$. Non-collinear spin calculations indicate that the easy magnetization axis of the Néel-AFM single-layer MnP_3 is oriented along the in-plane direction with small negative MAE.[159] The corresponding result reveals that single-layer MnP_3 exhibits antiferromagnetic properties, with the direction of magnetization can be altered with low energies.

The dynamical stability of single-layer $MnPS_3$ is determined by calculating its phonon band dispersions along the high-symmetry points of the hexagonal Brillouin Zone (BZ) and the results are presented in Fig. 6.2(a). The absence of any imaginary frequencies through the whole BZ indicates the dynamical stability of the free-standing

2D $MnPS_3$ layer. The crystal structure of $MnPS_3$ possesses 3 acoustical and 27 optical phonon branches. The frequency of the highest optical branch is found to be at 549 cm^{-1} at the Γ point of BZ. Low frequency phonon bands are dominated by Mn-S vibrations,

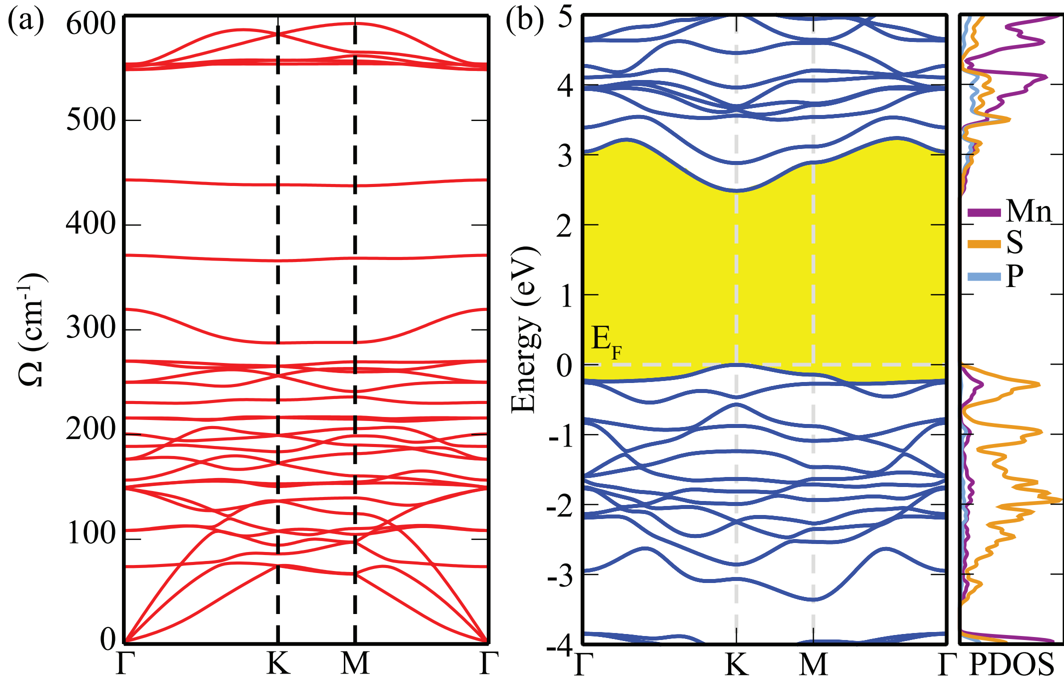

Figure 6.2. (a) The phonon band dispersions, and (b) electronic band structure and partial density of states (PDOS) of single-layer $MnPS_3$.

while the middle and high frequency modes mostly originate from the internal molecular-like vibrations of the $[P_2S_6]$ group. In addition, vibrations of two flat bands at 371 and 443 cm^{-1} and the high frequency bands are mostly independent of the Mn-vibrations. Mixed in-plane and out-of-plane vibrations characterize the first flat band, while the second branch is solely attributed to the in-plane vibrations. The presence of two flat bands is attributed to the vibration modes of the P_2S_6 clusters, in which the S atoms in the upper and lower layer exhibit either symmetrical or anti-symmetrical vibrations. Moreover, out-of-plane vibration of P atoms are dominant at the highest optical modes.

The electronic features of single-layer $MnPS_3$ are obtained through the electronic band structure and the corresponding partial density of states (PDOS) as shown in Fig. 6.2(b). In its ground state phase, single-layer $MnPS_3$ is found to be an AFM semiconductor with a direct band gap energy of 2.50 eV at the K point which is slightly lower than the bulk band gap energy (3.0 eV).[161] The valence band maximum (VBM) and the conduction band minimum (CBM) states are located at the K point of the BZ. Apparent from the PDOS, the VBM and CBM states are mainly dominated by the hybridization between Mn-S orbitals. Due to the D_{3d} symmetry of the trigonal anti-prismatic MnS_6 octahedron,

the Mn-*3d* orbitals can be separated into a single d_{z^2} orbital and two-fold degenerate d_{xz}, d_{yz}, d_{xy}, and $d_{x^2-y^2}$ orbitals. The VBM is primarily influenced by the hybridization of

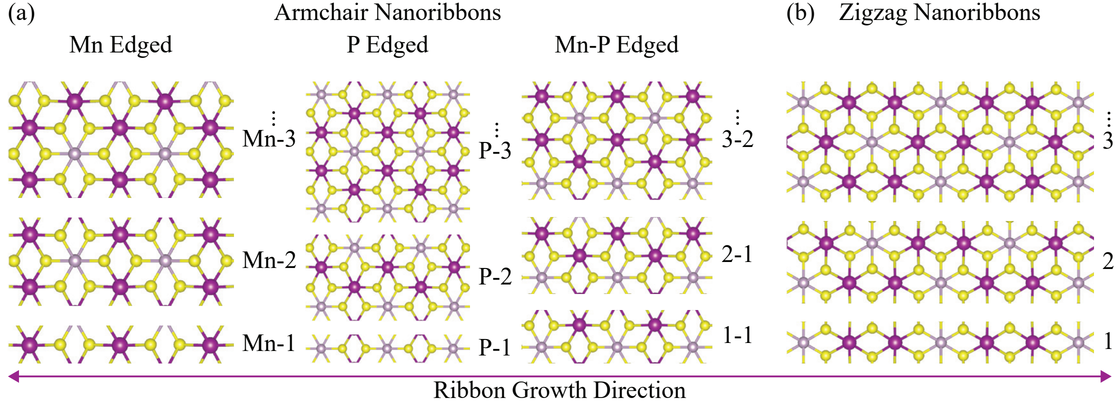

Figure 6.3. Structural illustrations of $MnPS_3$ nanoribbons (a) Mn-Mn, Mn-P, and P-P edged armchair nanoribbons, (b) Mn-P line zigzag nanoribbons. Numbers show the maximum width of the corresponding nanoribbons for this study.

Mn d_{xz}, d_{yz}, p_x, and p_y orbitals, which confirms the superexchange interactions between the Mn-*d* orbitals facilitated by the S-*p* orbitals. On the other hand, the CBM is formed by the d_{xz}, d_{yz}, d_{xy}, and $d_{x^2-y^2}$ orbitals of Mn, as well as the S p_x and S p_y orbitals, and the P-*p,s* orbitals.

6.2. Single-layer 1D Nanoribbons of $MnPS_3$

In this section, width-dependent structural, magnetic, and electronic properties of 1D nanoribbons of $MnPS_3$ are presented. The different structures of 1D forms of $MnPS_3$ are obtained by cutting the 2D structure along the two main orientations, namely armchair (AC) and zigzag (ZZ) orientations, as shown in Figs. 6.3(a) and (b). The constructed armchair nanoribbons (ANRs) are classified with respect to their edge-type formation as shown in Fig. 6.3(a). The three structures are formed such that both edges are ended up with Mn atoms (Mn-Mn) or with P atoms (P-P) or one edge is formed by Mn while the other edge is formed by P atoms (Mn-P). In the case of zigzag nanoribbons (ZNRs), both edges are formed by Mn-P lines independent of the width of the NR. Depending on the width, ANRs are labelled as Mn_N-ANR, Mn_N-P_N-ANR, and P_N-ANR, where Mn_N and P_N denote the number of Mn and P layers, respectively within the NR. In addition, ZNRs are labelled as N_z-ZNR, where N_z represents width of ZNRs. The representative illustration of each NR type is given in Figs. 6.3(a) and (b). For the widest ANR structure considered with Mn-edge consists of five Mn layers, the Mn-P edged NRs comprise six

Mn and three P layers, and P-edge NRs composed of five P layers. For the ZNRs, the widest structure considered in our study is constructed to have five Mn-P lines. In order to comprehend the impact of confining charge carriers in one dimension on magnetic characteristics, the FM and various AFM configurations are analyzed with for each width in the case of both ANRs and ZNRs. The energetic stability of the NRs are obtained

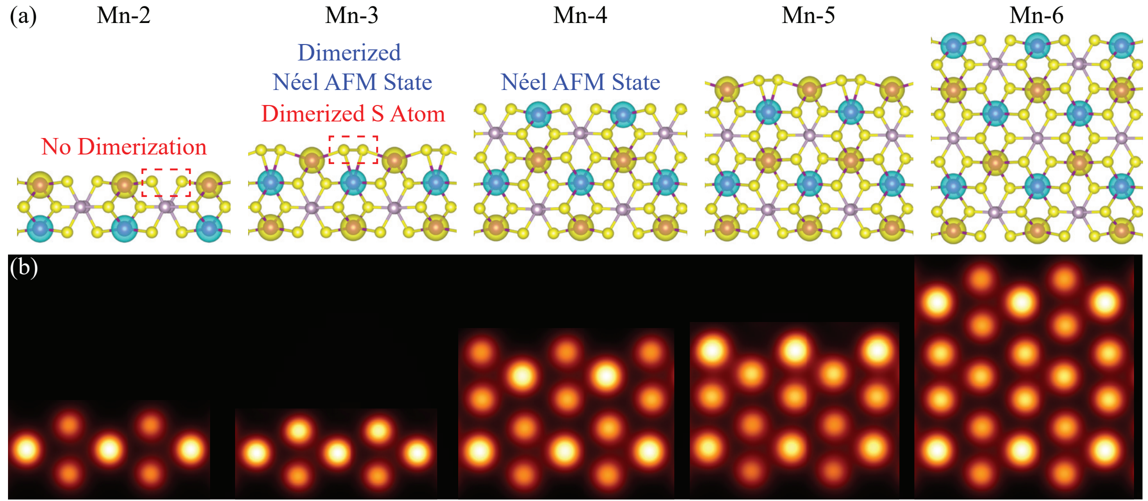

Figure 6.4. (a) Structural illustrations of Mn-Mn edged armchair nanoribbons with varying widths of two, three, four, five, and six layer, and (b) corresponding simulated STM images of Mn-Mn edged armchair nanoribbons.

by calculating the cohesive energy per atom for each structure. Moreover, chemical stability of NR surfaces is determined by computing the work functions (ϕ), which involves utilizing the local potential distribution along the out-of-plane direction.

6.2.1. Mn-Edged ANRs of $MnPS_3$

The optimized crystal structures of Mn_N-ANRs with varying widths are depicted in Fig. 6.4(a). In order to identify the ground state of each NR, various spin configurations are considered and the charge density differences for the ground state magnetic phases are presented. Total energy calculations reveal that Néel and dimerized Néel AFM configurations are energetically more favorable over the other spin configurations for Mn-2,4,6 and Mn-3,5,7 ANRs, respectively. Structurally, the P atoms, being the first nearest neighbors to S edges, weaken the bond between the S atoms and induce repulsion among them (S-S repulsion). In contrast, P atoms, being the second nearest neighbors to S atoms, have no significant effect on the interaction of the edge atoms. It is found that the interaction between P and S atoms is stronger when P is the first-nearest neighbor to S atoms. The

main reason is that P-P dimers are coordinated in tetrahedral manner with S atoms, and the presence of P atoms has no impact on the formation of dimerization of S atoms. On

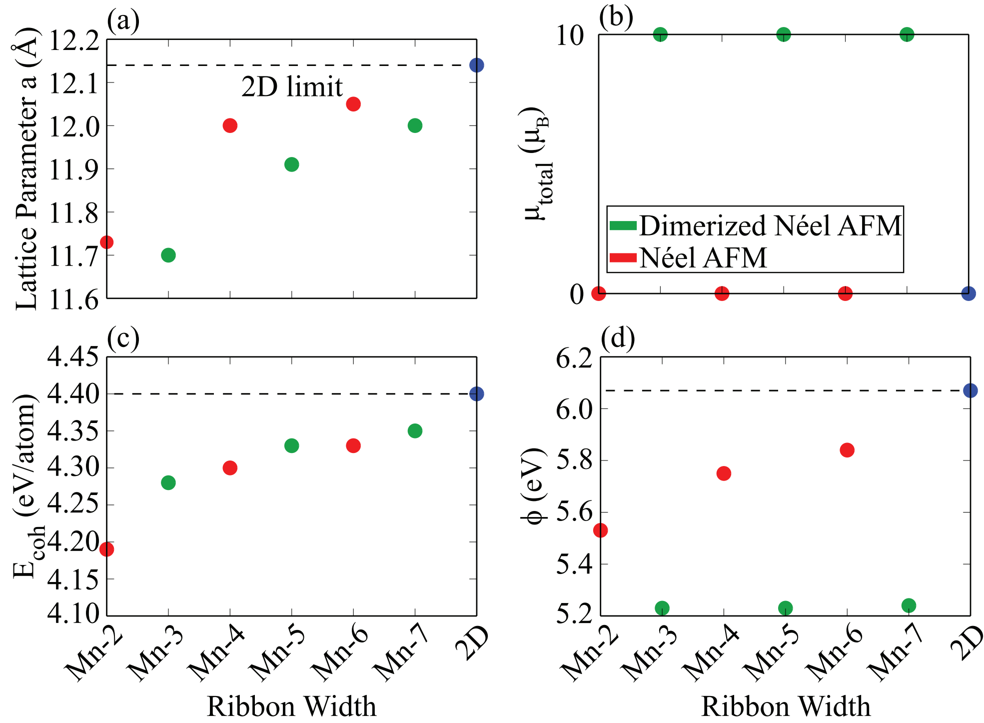

Figure 6.5. For Mn-edged armchair nanoribbons with varying widths, (a) lattice parameters, (b) total magnetizations, (c) cohesive energies, and (d) work functions.

the other hand, the presence of Mn atoms located at the sulfur edges induces the dimerization. The dimerization is caused by the strong affinity of Mn atoms that Mn atoms donate electrons to S atoms. The electron donation weakens the bonding between the S atoms, giving rise to the formation of S-dimerization. Furthermore, Mn atoms are octahedrally coordinated to six sulfide atoms in 2D structure. However, Mn atoms are unable to establish ideal six-fold coordination of octahedral symmetry at the edges in Mn_N-ANRs, and it leads to formed dimerization between S atoms. The reason of the non-dimerization and dimerization are particularly evident in Mn-4 and Mn-6 NRs, where two different structures facilitate a clear understanding of the mechanism. Consequently, edge reconstructions in Mn_N-ANRs exhibit variability based on the proximity of P and Mn atoms to the edges. Additionally, depending on whether the number of Mn layers is even or odd (Mn_2 structure), dimerization of S atoms occurs at the edges. Scanning Tunneling Microscopy (STM) is a highly effective technique for visualizing surfaces at the atomic limit. It enables the observation of individual atoms on a surface with high precision. In addition, it provides atomically precise information about the crystal structure. Here, we present our calculated STM images for Mn-Mn terminated ANRs with different widths

as seen in Figs. 6.4 (b). The bright spots belong to the top S atoms. In nanoribbons consisting of an even number of Mn layers, the edge S atoms that are non-dimerized look less bright. Conversely, in Mn-3,5 ANRs, sulfur atoms dimerize, making the edge atoms appear brighter. Therefore, dimerization and non-dimerization of S atoms at the edges can be distinguished via STM images for Mn-edged ANRs. In the case of an odd number of Mn layers, the additional Mn layer hinders the formation of a tetrahedral structure, leading to the formation of S dimers. The optimized lattice parameters may seem to fluctuate as shown in the Fig. 6.5(a), both Néel and dimerized Néel AFM structures consistently exhibit an overall increase until reaching the 2D limit. Despite the Mn-3,5,7 having a total magnetic moment of 10 μ_B as seen in the Fig. 6.5(b), both structures exhibit a preference for the dimerized Néel AFM phase as the magnetic ground state. In the odd case, the net magnetism arises from additional Mn layers. To quantify the energetic stability, we compute the cohesive energy, E_c in eV/atom, of different Mn-edged ANRs. Cohesive energies for Mn-edged ANRs are calculated to be 4.19, 4.28, 4.30, 4.33, 4.33, and 4.35 eV, respectively for the widths varying from 2-to-7 as seen in the Fig. 6.5(c). The cohesive energy

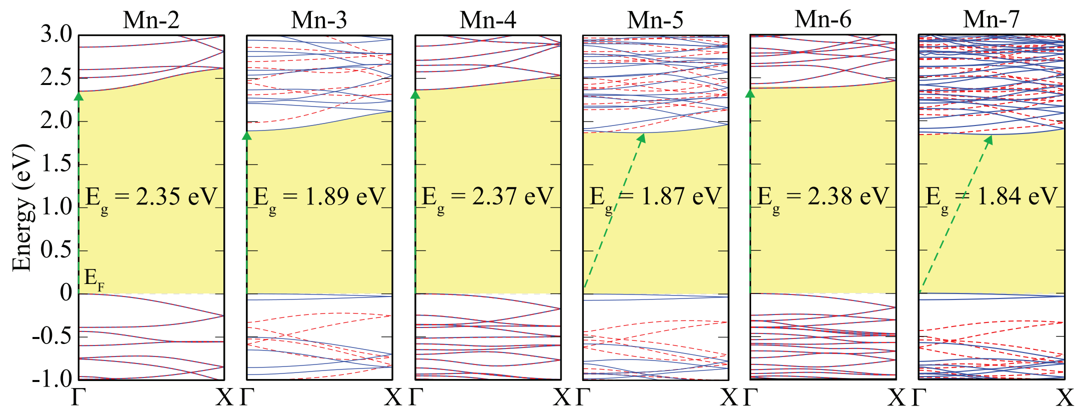

Figure 6.6. The calculated electronic band structures of Mn-edged armchair nanoribbons with varying widths of two, three, four, five, six, and seven layer.

values exhibit a continuous and consistent increase as the number of Mn layers increases, and at larger widths saturates to the 2D case. The cohesive energy results indicate that the S-S dimer formation results in higher cohesive energy. Moreover, using local potential distribution along the out-of-plane direction, the work functions of the Mn-edged ANRs are calculated to be 5.53, 5.23, 5.76, 5.23, 5.84, and 5.24 eV for the widths varying from 2-to-7 as shown in Fig. 6.5(d). When comparing the ϕ values of Néel and dimerized Néel AFM phases, it is evident that the values for Neel AFM structures display increasing trend and saturate towards the 2D limit. In the case of dimerized Néel AFM phase, the work function exhibits mostly a stable trend.

Electronic properties of Mn-edged ANRs are investigated in terms of the electronic band structures and the width-dependent electronic band gap energies. As seen in the Fig. 6.6, all of the considered Mn-edged ANRs display semiconducting behavior as in the case of 2D structure. Considering the even number edge Mn-edged ANRs, all structures are direct band gap semiconductors with increasing band gap energies from Mn-2 to Mn-6 ANR. Both the VBM and CBM states even number edge ANRs are shown to

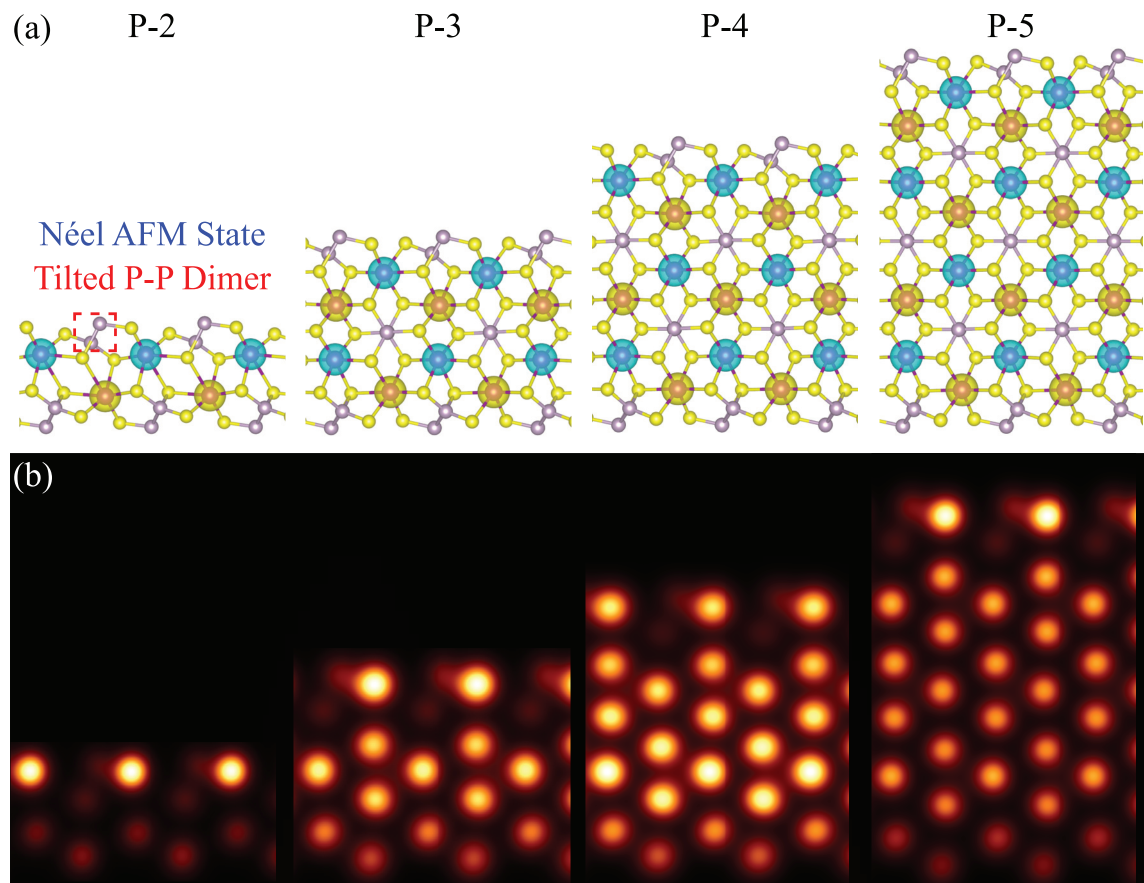

Figure 6.7. (a) Structural depictions of P-P edged armchair nanoribbons with varying widths of P-2, P-3, P-4, and P-5, and (b) corresponding simulated STM images of P-P edged armchair nanoribbons.

reside at the Γ point. The Mn-edged ANRs with odd number of widths display decreasing trend in terms of the band gap energy (1.89, 1.87, and 1.84 eV for the Mn-3, Mn-5, and Mn-7 ANRs, respectively). While the Mn-3 ANR is a direct band gap semiconductor, the CBM state shifts to between the Γ-X for the wider NRs that Mn-5 and Mn-7 ANRs are indirect gap semiconductors. The Mn-edged ANRs with odd number of Mn-layers have two common features that on one edge S-S dimerization occurs and dimerized Néel AFM phase leads to the formation of net magnetism. The band gap energy of Mn-edged ANRs having even number of Mn-layers increases with increasing NR width and is expected to

reach the 2D limit for wider structures. In contrast, the band gap energy of odd number edge ANRs decreases with increasing NR width, which is dominated by the presence of S-S dimers on the edges which are absent in perfect 2D layer.

6.2.2. P-Edged Armchair Nanoribbons of $MnPS_3$

The optimized atomic structures of P-edged ANRs with different widths and edge reconstructions are demonstrated in Fig. 6.7(a). The widths are named with respect to the number of phosphorus layers, ranging from the widest width comprised of seven phosphorus layers to the narrowest width formed by two phosphorus layers. Structural optimizations reveal that all of the P-edged ANRs display the same structural behavior on the edges. In single-layer 2D structure, the P-P dimers are formed in a tetrahedral arrangement and binded to three S atoms to create a $[P_2S_6]^{4-}$ bipyramid. In the case

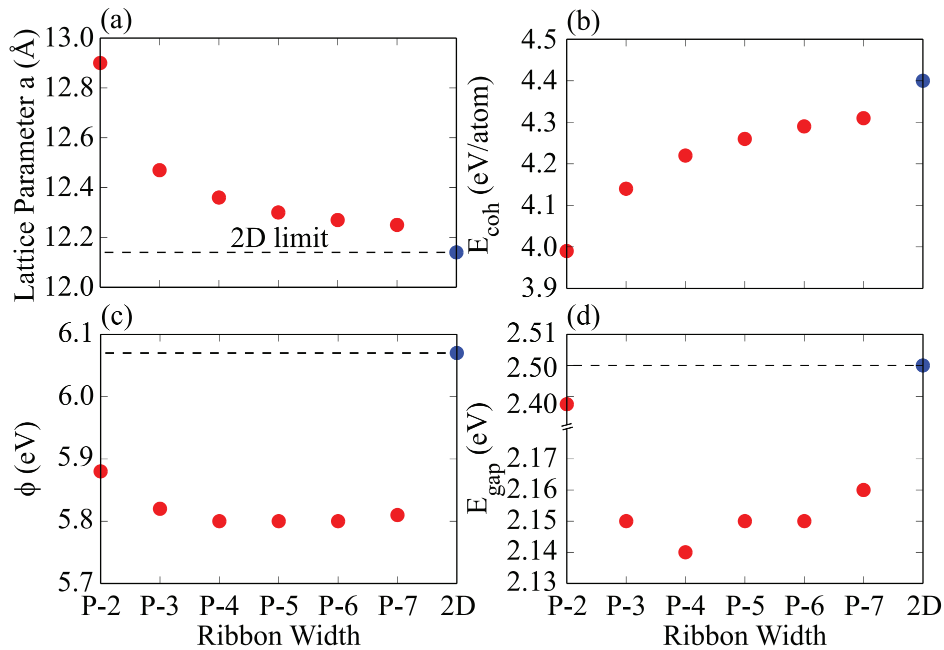

Figure 6.8. (a) The lattice parameters, (b) cohesive energies, (c) work functions and (d) band gap variations of P-edged armchair nanoribbons with different widths.

of P-edged ANRs, unoccupied atomic orbitals at the edges result in formation of tilted-dumbbell structure due to the absence of a S atom in the bipyramid as seen in Figs. 6.7(a). The P atom forming the P-P dimer is unable to establish a tetrahedral configuration with three S atoms. The upper P atom at the P-P dimer tilts in an upward and rightward direction to approach the tetrahedral structure, resulting in a tilted-dumbbell shape at the

edge. Such a configuration is found to occur regardless of the width of the NR. Magnetic phase calculations of P-edged ANRs indicate a tendency to be at the Néel AFM phase as a ground state interaction, and AFM ordering persists down to the thinnest P-edged ANRs. The predicted STM images for P-edged ANRs with varying widths are illustrated in Fig. 6.7(b). The S atoms binded to the upper P atom of tilted dimers are as bright spots in STM images. In addition, the tilted-dumbbell structure of P atoms can be identified near the S atoms at edges. The optimized lattice parameters of the P-edged ANRs is found to decrease and approaches to the 2D limit as the width increases, as shown in Fig. 6.8(a). The cohesive energies of various P-edged ANRs are calculated to be 3.99, 4.14, 4.22, 4.26, 4.29, and 4.31 eV/atom, for the P-2, P-3,P-4, P-5, P-6, and P-7 structures, respectively. As appear from the Fig. 6.8(b), the cohesive energies display a gradual and uniform increasing trend with increasing width. The formation of tilted dumbbell shaped P atoms at the edges causes the reduction of the cohesive energies as compared to those of Mn-edged ANRs. The work functions of P-edged ANRs are calculated to be 5.88, 5.82, 5.80, and 5.80, 5.80, and 5.81 eV by utilizing local potential distribution. For the narrowest P-edged ANR, the work function is determined by the edge structure and as the ribbon width increases, the work function values are found to reach almost a constant value due to the weak contribution of edge atoms to the work function.

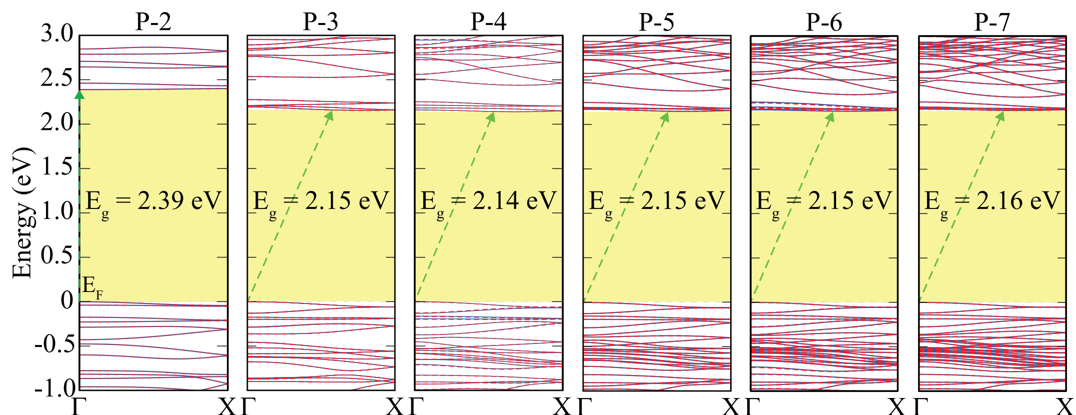

Figure 6.9. Electronic band structures of P-2, P-3, P-4, P-5, P-6 and P-7 armchair nanoribbons.

Electronic band structures reveal that P-edged ANRs are AFM semiconductors regardless of the ribbon width as shown in Fig. 6.9. For the narrowest P-edged ANR, the calculated band gap energy is larger than that of wider NRs due to the dominating confinement effects. As the width increases, the band gap energy suddenly decreases from P-2 to P-3 ANR and tends to saturate around 2.15 eV. For the P-7 ANR, there exists a 0.01 eV of increment in the band gap energy and it is expected to saturate to the 2D limit

for larger NRs (see Fig. 6.8(d)). Apparently, except for the narrowest P-edged ANR, the wider structures are found to exhibit indirect band gap semiconducting behavior. While

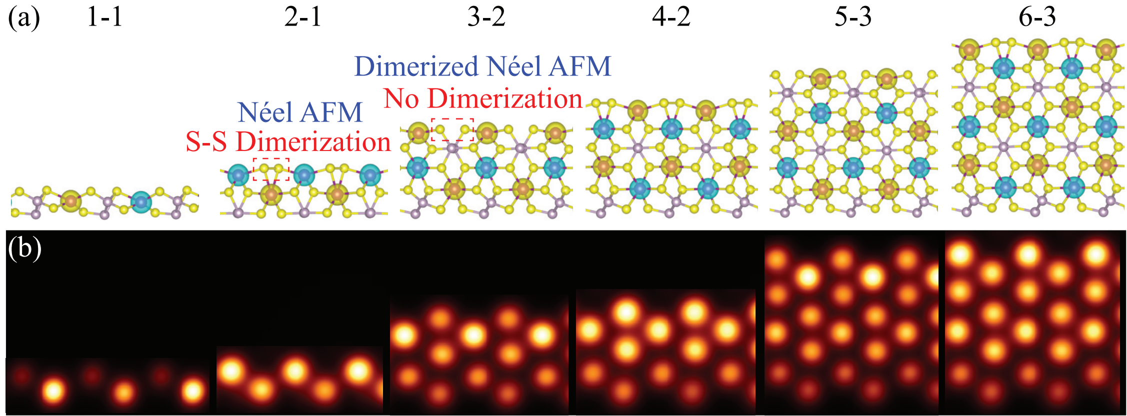

Figure 6.10. (a) Structural illustration of Mn-P edged ANRs with different widths of 1-1, 2-1, 3-2, 4-2, 5-3, and 6-3. The labels indicate the number of Mn, and P layers, respectively in each configuration. (b) Corresponding simulated STM images of Mn-P terminated armchair nanoribbons.

the VBM and CBM reside at the Γ point for P-2 ANR, the CBM state shifts towards the X high symmetry point resulting in the indirect behavior. The band gap energies are found to be 2.39, 2.15, 2.14, 2.15, 2.15, and 2.16 eV, respectively, for P-edged ANRs.

6.2.3. Mn-P Edged Armchair Nanoribbons of $MnPS_3$

The optimized crystal structures of Mn-P edged ANRs with various edge reconstructions are presented in Fig. 6.10(a). The two types of edge reconstructions, S-S dimerized and non-dimerized edges, are also shown on the figure. The widths of NRs are determined by the number of Mn and P layers and are denoted by Mn_N-P_M-ANR where N and M stand for the number of Mn and P layers, respectively. In the rest of the section, the different width ANRs are labelled as $_{N\text{-}M}$ ANR. The widest ANR considered in our study comprises eight Mn and four P layers, while the narrowest structure is formed by one layer of Mn and P. Structurally, 2-1 Mn-P edged ANR exhibits slightly different edge reconstructions as compared to the rest of the Mn-P edged ANRs. One edge of all Mn-P edged ANRs is formed by the tilted P-P dumbell structure, except for the 2-1 Mn-P edged ANR in which the P-P dumbells are not tilted. The S-S dimerization on one edge of 2-1 Mn-P edged ANR causes the P-P dumbells on the other edge to keep their untilted form. Note that for the 4-2 and 6-3 Mn-P edged ANRs, the formation of S-S dimerization does not affect the tilting of P-P dumbells on the other edge since there exist at least one P-layer

in the center of the ANR. Another signature of having either S-S dimer or non-dimerized edge is that if the last two atomic lines of the ribbon on the Mn edge are P and Mn layers, then S-S dimerization does not occur. In contrast, if such two atomic lines are formed by two Mn lines, then the edge S atoms tend to dimerize (see Fig. 6.10(a)). Apparently, if the existing number of Mn layers is even, then the Mn edge of ANR is formed by S-S dimerizations. However, in the case of odd numbered Mn layers, the S atoms on the Mn edge are not dimerized. As confirmed by the STM images shown in Fig. 6.10(b), as the S atoms on the edges are dimerized, the upper S atoms lying on the second Mn layer appear to be brighter than those in the non-dimerized structure. Note that in the S-S dimerized ANRs, the edge S atoms do not appear in the STM image since the dimerized S atoms get lower in height from the surface as they form S-S dimers. In contrast, as the edge S atoms do not form dimers, one of the edge S atoms reside on the surface and is observable in the STM image. The calculated lattice parameters of the Néel AFM structures are found

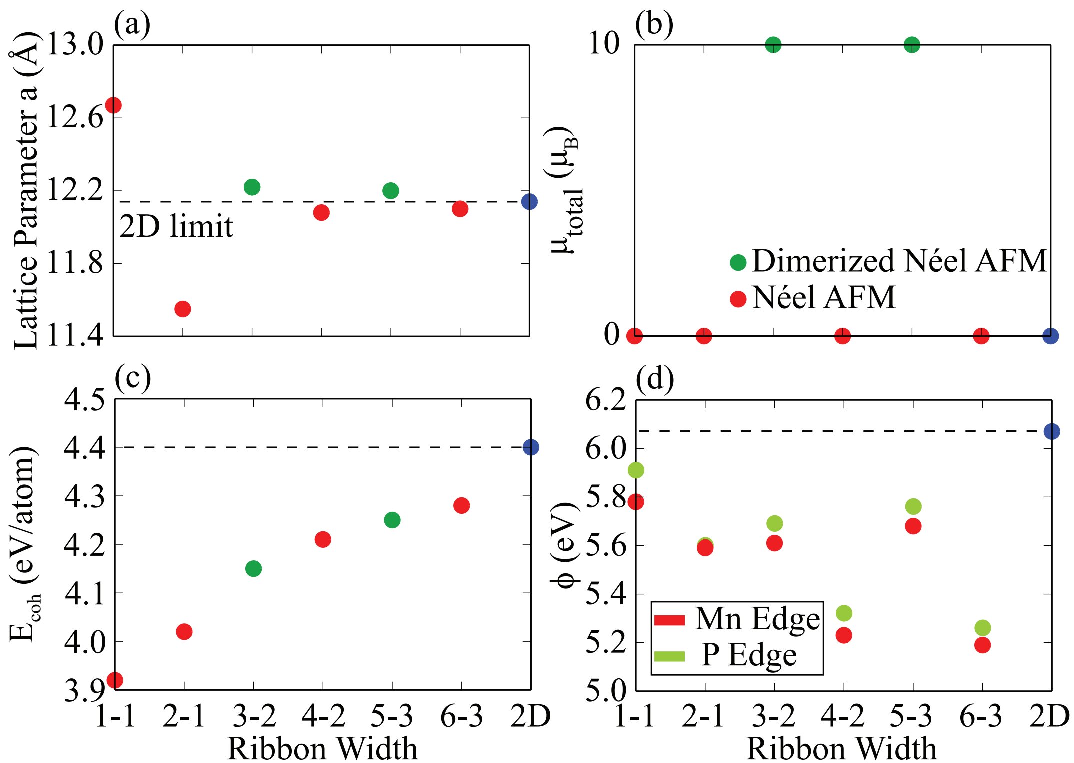

Figure 6.11. (a) The calculated lattice parameters, (b) total magnetizations, (c) cohesive energies, and (d) work functions of Mn-P edged armchair nanoribbons with different widths.

to display an increasing trend except for the narrowest ANR. In the case of ANRs having dimerized Néel AFM state, the optimized lattice parameters are found to be very close to that of 2D structure (Fig. 6.11(a)). The various spin configurations are examined for each Mn-P edged ANRs and the total energy analysis indicates that Mn-P edged ANRs exhibit

a preference for Néel AFM (1-1, 2-1, 6-3, and 8-4 ANRs) and dimerized Néel AFM configurations (3-2, 5-3, and 7-4 ANRs) with a total magnetic moment of 10 μ_B as seen in Fig. 6.11(b). It appears from the magnetic ground state analysis that for the odd number

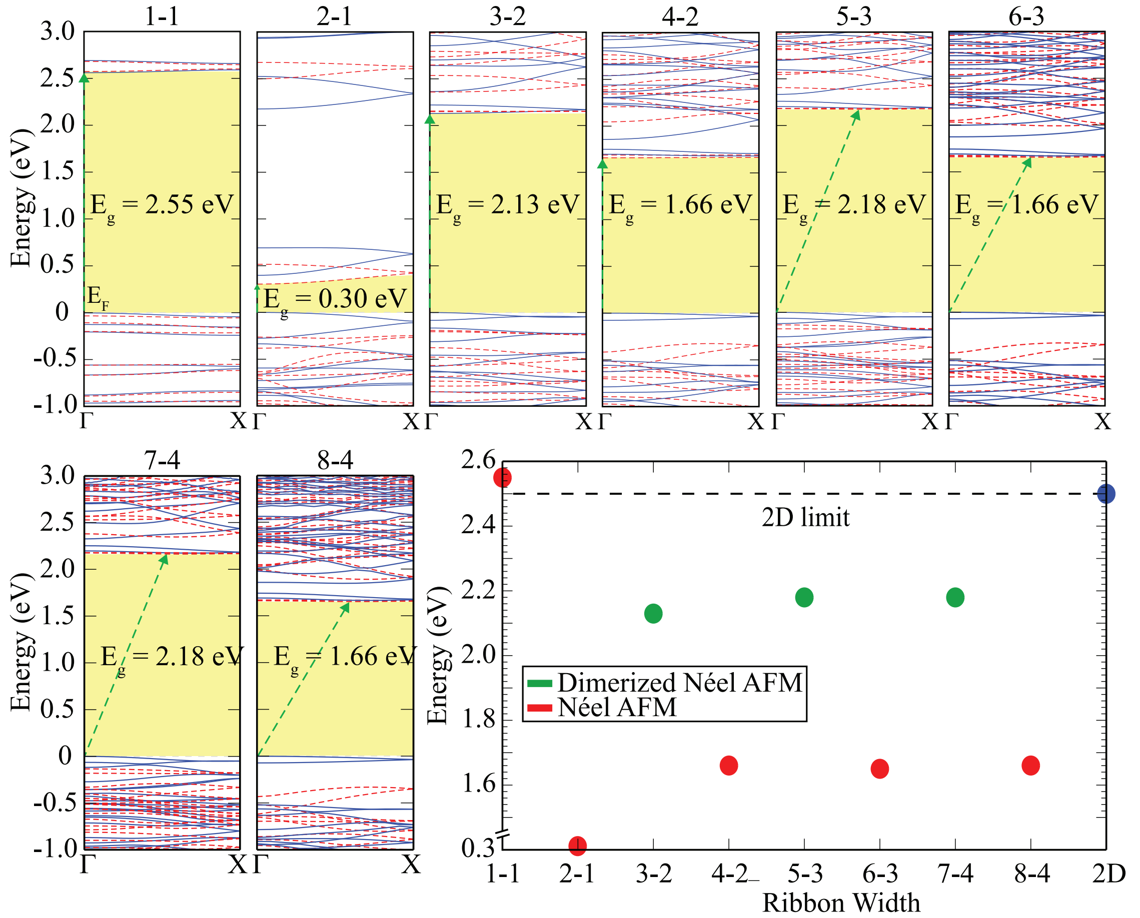

Figure 6.12. The calculated electronic band structure of Mn-P terminated armchair nanoribbons with varying widths of 1-1, 2-1, 3-2, 4-2, 5-3, 6-3, 7-4, and 8-4. The chart below the band structures present the relationship between the width of the ribbon and the variation in band gap values for Mn-P edged ANRs.

of layers of Mn the magnetic ground state is dimerized Néel AFM except for the narrowest ANR. In order to determine the chemical stability of Mn-P edged ANRs, the cohesive energies are calculated in eV/atom. Cohesive energies of Mn-P edged ANRs are calculated to be 3.92, 4.02, 4.15, 4.21, 4.25, and 4.28 eV respectively, as seen in Fig. 6.11(c). The cohesive energies possess a gradual increase with increasing ANR width. Moreover, work function values are calculated for the two surfaces since an internal out-of-plane dipole is created within the ANRs. Having P-P dumbells on one edge and Mn-layer on the other edge causes the formation of dipole due to different local potentials on each surface. Therefore, the work functions are calculated for both surfaces in the case of Mn-P edged ANRs. The work function values are calculated to be 5.78, 5.59, 5.61, 5.23, 5.68,

and 5.19 eV for one surface and 5.91, 5.60, 5.69, 5.32, 5.76, and 5.26 eV the other surface. The highest potential difference between the two surfaces occur for the narrowest ribbon (0.13 eV) due to the tilted P-P dumbells dominating the structural formation of the ribbon. The lowest potential difference is found in the case of 2-1 Mn-P edged ANR (0.01 eV) due to the untilted P-P dumbells on the edge of the ribbon. Although, there exist tilted P-P dumbells on one edge for the wider ribbons, the potential difference between the two surfaces decrease with increasing ribbon width since the averaged potential is dominated by the central atoms.

The width-dependent electronic band structures are calculated by also considering the 7-4 and 8-4 Mn-P edged ANRs in order to correctly analyze the width behavior of the electronic band gap energy. As shown in Fig. 6.12(a), all the Mn-P edged ANRs exhibit semiconducting behavior regardless of the ribbon width. The NRs of 1-1, 2-1, 3-2 and 4-2 Mn-P edged structures are found to be direct band gap semiconductors, whose VBM and CBM states reside at the Γ point of the BZ. For the wider ANRs, namely 5-3, 6-3, 7-4, and 8-4, all structures are shown to display indirect band gap behavior, whose CBM state shifts to between Γ-X points of the BZ. The narrowest Mn-P edged ANR has an band gap energy of 2.55 eV which is the highest among all considered ANRs and even larger than that of 2D structure.

6.2.4. Zigzag Nanoribbons of $MnPS_3$

The optimized structures of zigzag nanoribbons (ZNRs) with varying widths are shown in Fig. 6.13(a), for which the widths are identified by the number of zigzag layers. In order to determine the magnetic ground state, four different spin configurations (FM, Néel-, zigzag-, and stripy-AFM) are constructed. Total energy calculations reveal that the first and second narrowest ZNRs exhibit Néel-AFM coupling, while wider ZNRs, considered up to seventh width, demonstrate FM coupling between the Mn atoms with tiny opposite spin contributions of edge S atoms which are binded to two Mn atoms. The first and second ZNRs display distinctive structures as seen in Fig. 6.13(a). At the edge of the structures, Mn atoms bond with nearby S atoms, causing the intervening S atoms to move downward and elongating the bond length between them. However, the influence of the edge S atoms is insufficient to impact the magnetic interaction in the first and second ZNRs, leading to an AFM ground state. The transition from the AFM ground state in first and second ZNRs to the FM ground state in the third to seventh ZNRs is attributed to the influence of edge S atoms facilitating a superexchange interaction be-

tween the two Mn atoms. While located along the ZZ lines, Mn atoms contribute to the formation of FM arrangement. Additionally, edge S atoms between the two Mn atoms

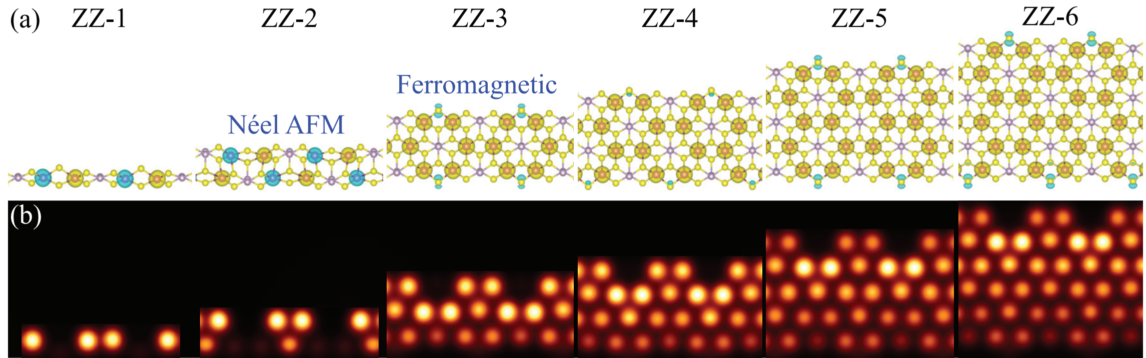

Figure 6.13. (a) Optimized structures of ZZ nanoribbons with varying widths of 1, 2, 3, 4, 5, and 6. The labels indicate the number of layer, and (b) corresponding simulated STM images of ZNRs.

disrupt the FM interactions between Mn atoms, leading to a decrease in the total magnetization. The interplay of edge effects, electron transfer between Mn and S atoms, and the interior structure influences the magnetic arrangement, resulting in the emergence of FM. In addition, we provide our calculated STM images of ZNRs for varying width as shown in Fig. 6.13(b). Firstly, in the case of ZNRs, the S atoms between the two Mn atoms are not observable by means of the brightness. For all widths of ZNRs, the lowest edge atoms are not visible in the STM images, and the surrounding S atoms appear to be less bright. Moreover, the brightest triangle-shaped spots appearing in the STM images are attributed to the bipyramid formed by the P-P dimers surrounded by the neighboring S atoms. Lastly, the less bright triangular-shaped spots are found to appear from the incomplete formation of the bipyramid structure due to the missing S atoms. The total energy difference between AFM and FM states are calculated for the 3-7 ZNRs in order to determine the critical width for which the Néel-AFM state becomes energetically favorable over the FM state. The energy difference gradually decreases as the width of the ribbon increases (see Fig. 6.14(a)). Upon plotting and quadratic fitting the energy difference between Néel-AFM and FM for widths ranging from three to seven, the Néel-AFM interaction is predicted to be favorable over the FM state at eighth width ZNR. Simultaneously, the lattice parameter shows a gradual increase from the third to seventh ZNR, excluding the first and second, and eventually approaches to that of 2D limit (see Fig. 6.14(b)). From third to seventh width ZNR, nanoribbons exhibit a progressively increasing net magnetic moment as shown in Fig. 6.14(c). In addition, the net magnetic moment can be calculated using the formula $20n - 8$, where $20n$ represents a total magnetization increase of 20 μ_B

per atom for FM and n stands for the width of the ZNRs. The term 8 corresponds to a net decrease in total magnetic moment due to the presence of S atoms between two Mn atoms at the edges. The decrease arises from the superexchange interaction, where each

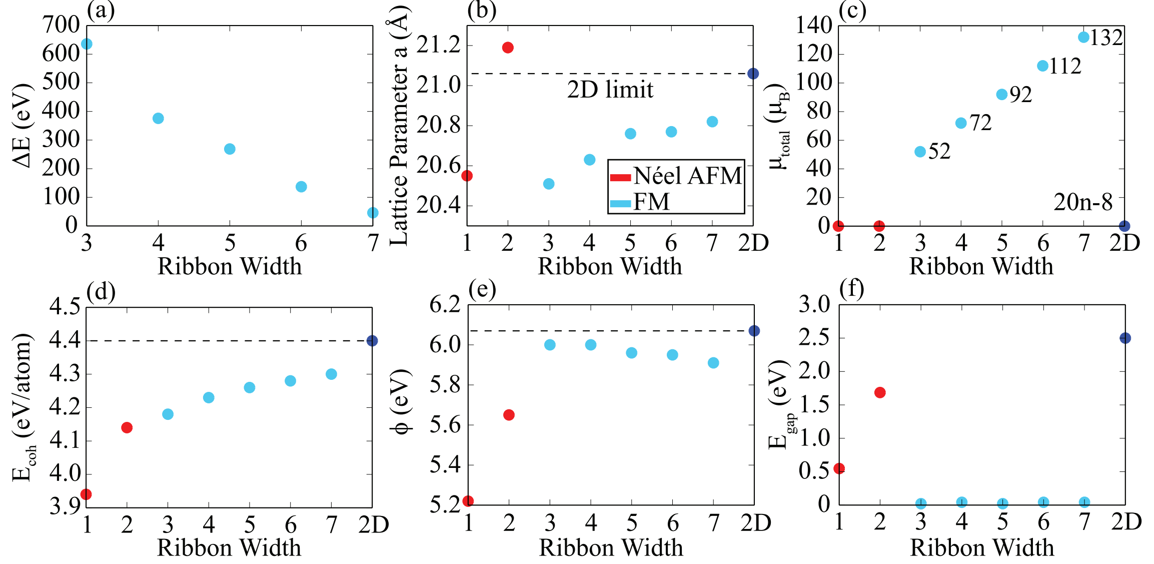

Figure 6.14. For the zigzag nanoribbons, (a) total energy difference between AFM and FM magnetic ground states, (b) the calculated lattice parameters, (c) total magnetizations, (d) cohesive energies, (e) work functions, and (f) band gap variations.

S atom weakens the interaction between the Mn atoms, leading to an magnetic moment reduction of $-2\mu_B$ per S atom. To determine the stability of the ZNRs, cohesive energies are calculated to be 3.94, 4.14, 4.18, 4.23, 4.26, 4.28, and 4.30 eV for the widths from 1 to 7, respectively. The cohesive energy consistently and progressively increases with the number of width, ultimately reaching a saturation point at the 2D limit (see Fig. 6.14(d)). Furthermore, as presented in (see Fig. 6.14(e)), the work function values of ZNRs are calculated to be 5.22, 5.65, 6, 5.99, 5.96, 5.95, and 5.91 eV by using local potential distribution along the out-of-plane direction. Except for the first and second ZNRs, work function gradually decreases.

The Fig. 6.15 presents the electronic band dispersions of ZNRs as a function of the ribbon width. The calculated electronic band structures show that ZNRs exhibit either AFM or FM semiconducting behavior, and even metallic character depending on the ribbon width. Band dispersions of the ZNRs are significantly influenced by the superexchange interaction between Mn and S atoms (Mn-S-Mn). The band gap energies of ZNRs are calculated to be 0.85, 1.95, 0, 0.04, 0, 0.04, and 0.04 eV from ZZ-1 to ZZ-7 NRs, respectively. The band gap of ZZ-1 and ZZ-2 widens as the width increases, exhibiting antiferromagnetic semiconducting behavior. However, after the second width, ZNRs un-

dergo a transition from an Néel AFM to a ferromagnetic magnetic ground state due to the superexchange interaction between Mn atoms, resulting in differences in their electronic properties. Nanoribbons consist of even number of zigzag layers exhibit semiconducting

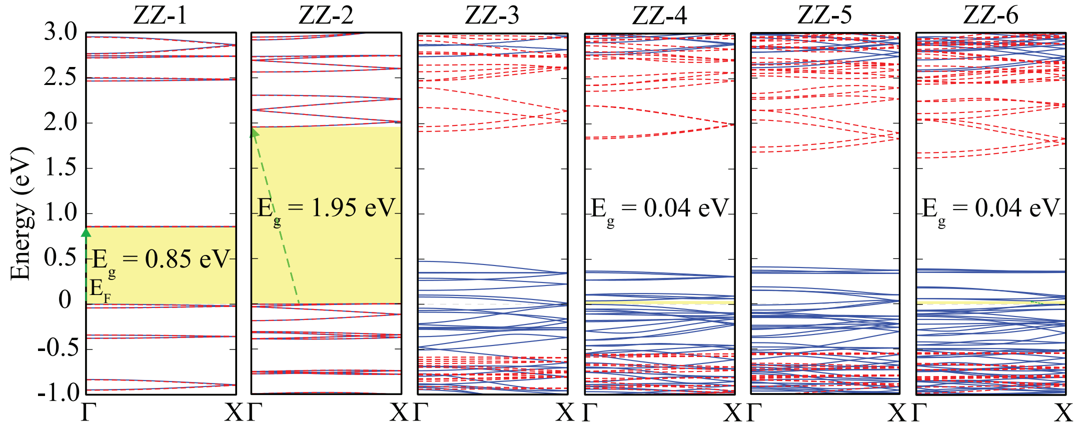

Figure 6.15. The calculated electronic band structures of zigzag nanoribbons with different widths ranging from 1 to 6.

behavior with 0.04 band gap energy, while those with an odd number of zigzag layers demonstrate metallic character with zero band gap energy, until the seventh layer for structures with FM ground state. In the seventh layer, metallic behavior ceases as the energy distinction between the FM and AFM ground states nearly converges to zero. The odd-even oscillations persist up to the sixth width; however, upon reaching the seventh width, they vanish as the energy difference between the AFM and FM states decreases and approaches the Néel AFM state. After the ZZ-7, when the ground state of ZNRs returns to Néel AFM, their band gaps will saturate towards the 2D limit with increasing width.

CHAPTER 7

CONCLUSION

The orientation-dependent behavior of ultra-thin two-dimensional (2D) and one-dimensional (1D) materials is of significant interest due to their anisotropic features, which enable various advanced applications. Polarization-dependent photodetectors, crucial in imaging, communications, and sensing, leverage these anisotropic properties to detect and respond to the polarization state of light. Nanomechanical devices exploit the orientation-dependent mechanical characteristics of materials to create innovative sensors and transducers. Additionally, anisotropic materials are essential for polarization-sensitive optical components such as waveguides, lenses, and filters, used in optical communication, displays, and imaging technologies. In nanoelectronics, these properties are employed to develop high-performance transistors, logic gates, and memory devices with enhanced functionality and efficiency. Similarly, the anisotropic features of materials in optoelectronic devices facilitate the creation of efficient LEDs, solar cells, and photonic integrated circuits, customized for specific applications by manipulating the crystal lattice orientation.

In the present thesis, a comprehensive exploration of the fundamental anisotropic properties in single-layer structures was conducted, with a focus on the confinement effects in two-dimensional (2D) and one dimensional (1D) crystal lattices. In addition, the basics of density functional theory (DFT) were elucidated. DFT serves as a cornerstone in understanding the structural, magnetic, vibrational, electronic, optical, and elastic properties of materials, providing a theoretical framework for the comprehensive analyses conducted in this study. Alongside the application of these theoretical methods, two studies recently published as original scientific papers within the scope of this thesis were provided.

First of all, the highly anisotropic structural, vibrational, thermal, electronic, optical, and elastic properties of single-layer $HfTe_5$ were investigated.[201] Total energy and geometry optimizations reveal that 2D single-layer form of $HfTe_5$ exibits in-plane anisotropy. Phonon band structure shows the dynamical stability of the free-standing layer and the predicted Raman spectrum displays seven characteristic Raman active phonon peaks. In addition to the dynamical stability, $HfTe_5$ is shown to exhibit thermal stability at room temperature as confirmed by Quantum Molecular Dynamics simulations. Moreover, the

obtained elastic-stiffness tensor elements indicate the mechanical stability of the $HfTe_5$ with its orientation-dependent soft nature. The electronic band structure calculations show the indirect-gap semiconducting behavior of $HfTe_5$ with a narrow electronic band gap energy. Optical properties of $HfTe_5$, in terms of its imaginary dielectric function, absorption coefficient, reflectance, and transmittance, are shown to exhibit strong in-plane anisotropy. Furthermore, structural analysis of several point defects and their oxidized structures are investigated by means of the simulated STM images. Among the considered vacancy defects, namely $V_{Te_{ch}}^{u}$, $V_{Te_{ch}}^{d}$, $V_{Te_{out}}$, $V_{Te_{in}}$, $V_{Te_{out}}^{dim}$, and V_{Hf}, the formation of $V_{Te_{out}}$ is the most favorable defect. While $V_{Te_{out}}^{dim}$, and V_{Hf} defects lead to local magnetism, only the oxygen substituted V_{Hf} structure possesses magnetism among the oxidized defects. Moreover, it was found that all the bare and oxidized vacant sites can be distinguished from each other through the STM images. Overall, our study indicates not only the fundamental anisotropic features of single-layer $HfTe_5$ but also shows the signatures of feasible point defects and their oxidized structures which may be useful for future experiments on 2D $HfTe_5$. Moreover, another highly anisotropic family, TiX_5, was investigated in terms of its structural, vibrational, electronic, and elastic properties. The analysis of geometry optimizations, phonon band dispersions, and linear-elastic coefficients of single-layer $TiSe_5$ and $TiTe_5$ provided insights into the structural, dynamical, and mechanical stability of these structures, respectively. On the other hand, although TiS_5 shares the same crystal phase as $TiSe_5$, $TiTe_5$, and $HfTe_5$, it is not dynamically stable due to the presence of imaginary frequencies in its phonon band dispersion, despite demonstrating mechanical stability. Electronically, TiS_5 and $TiSe_5$ are direct band gap semiconductor with electronic band gaps of 0.06 eV and 0.16 eV, respectively, while $TiTe_5$ is a metal. Orientation-dependent linear-elastic characteristics of TiX_5 demonstrate their structural anisotropy.

Secondly, the stability and fundamental properties of single-layer TaS_3, $TaSe_3$, and $TaTe_3$ were investigated by performing DFT-based ab initio calculations. The geometry optimization, phonon band dispersion, and linear-elastic properties of single-layer TaX_3 were found to possess the structural, dynamic, and mechanical stability of the free-standing layers. Additionally, our calculated STM images of TaX_3 layers revealed that structures with the same underlying framework but different chalcogen atoms can be distinguished from one another. Electronically, TaX_3 layers was found to show metallic character. The optical characteristics of individual TaX_3 structures were demonstrated by analyzing their imaginary dielectric function, absorption coefficient, reflectance, and transmittance. The findings indicated that each structure exhibited optical anisotropy. The

linear-elastic characteristics of each crystal structure exhibit direction-dependent mechanical responses, providing insight into their highly anisotropic and soft character.

Next, the anisotropic structural, vibrational, electronic, and elastic properties of single-layer α-Bi were investigated by performing DFT-based first-principles calculations.[202] Structural optimizations show that free-standing α-Bi possesses tilted black phosphorus-like anisotropic structure. The phonon band dispersions and the linear-elastic parameters reveal the dynamical and mechanical stability of the α-Bi structure, respectively. In addition, quantum molecular dynamics simulations indicate the thermal stability of the single-layer at room temperature. Electronically, it was found that α-Bi exhibits indirect band gap semiconducting behavior. Both the hole and electron effective masses were shown to be orientation-dependent with the latter being more anisotropic. Such anisotropic effective masses reveal the orientation-dependent transport properties in single-layer α-Bi. Moreover, the orientation-dependent elastic features of α-Bi show that at angle of 45 degrees with respect to the zigzag orientation, an auxetic behavior was predicted for the structure. Furthermore, the impact of uniaxial strains along the two main orientations (zigzag and armchair directions) were investigated on the vibrational properties of single-layer α-Bi. The phononic stability of the structure was first predicted at the strain limits (± 5) for both directions and the results reveal the preserved stability of the single-layer under both compressive and tensile strains. The calculated Raman spectra under uniaxial strains show that the type (compressive or tensile) and the direction of the applied strain can be deduced from the Raman spectra analysis. Overall, strain-induced modifications in the Raman spectrum of 2D α-Bi in terms of the peak positions may be a useful tool for the characterization of induced strain in experimental studies.

Lastly, we investigated the edge and width-dependent anisotropy in 1D manganese phosphorus tri-sulfide ($MnPS_3$) nanoribbons to analyze 1D anisotropy. 1D nanoribbon forms of manganese phosphorus tri-sulfide ($MnPS_3$) were investigated in terms of the structural, magnetic, and electronic properties. For the 2D free-standing stable structure of $MnPS_3$, Néel-antiferromagnetic (AFM) interaction was shown to emerge as the energetically most favorable phase. By cutting single-layer $MnPS_3$ along the two high-symmetry orientations, namely armchair (AC) and zigzag (ZZ) directions, leads to the formation of 1D nanoribbons (NRs) of $MnPS_3$. Depending on the edge atoms, it was found that three different armchair NRs (ANRs) of $MnPS_3$ can be formed, namely Mn-Mn, P-P, and Mn-P edged structures, while the formed zigzag NRs (ZNRs) were shown to be edge-independent. The optimized geometries of ANRs show structural variations at the edges such that S-S dimerization occurs for the Mn-Mn ANRs having odd layer

number of Mn atoms while even layer number of Mn atoms in Mn-P edged ANRs reveal the existence of S-S dimers at one edge. In addition, a tilted P-P dumbbell formation occurs regardless of the ribbon width in P-P edged ANRs. Magnetically, either Néel or dimerized Néel-AFM ground states were found to describe magnetic properties of $MnPS_3$ ANRs, where the latter exists as the number of Mn layers is odd. Moreover, the superexchange interaction between the edge Mn and S atoms leads to a ferromagnetic ground state in ZNRs except for the two narrowest structures. The Scanning Tunneling Microscopy (STM) image analysis reveal that either S-S dimerization or the formation of P-P dumbells can be identified via STM images. Electronically, Mn-Mn, P-P, and Mn-P edged ANRs were shown to exhibit semiconducting behavior similar to the 2D form of $MnPS_3$, which is an antiferromagnetic semiconductor. In contrast, ZNRs were shown to exhibit either antiferromagnetic semiconducting nature for the two narrowest ribbons and either ferromagnetic half-metallic or semiconducting behavior for the wider ribbons. Overall, our predictions on the 1D NR forms of $MnPS_3$ reveal that both ANRs and ZNRs of $MnPS_3$ provide opportunity to design nanostructures whose electronic and magnetic features were significantly edge reconstruction and ribbon width dependent.

REFERENCES

1. Tiwari, J. N.; Tiwari, R. N.; Kim, K. S. Zero-dimensional, one-dimensional, two-dimensional and three-dimensional nanostructured materials for advanced electrochemical energy devices. *Progress in Materials Science* **2012**, *57*, 724–803.
2. Mas-Balleste, R.; Gomez-Navarro, C.; Gomez-Herrero, J.; Zamora, F. 2D materials: to graphene and beyond. *Nanoscale* **2011**, *3*, 20–30.
3. Schwierz, F. Graphene transistors. *Nature nanotechnology* **2010**, *5*, 487–496.
4. Novoselov, K.; Mishchenko, A.; Carvalho, A.; Castro Neto, A. 2D materials and van der Waals heterostructures. *Science* **2016**, *353*, aac9439.
5. Ferrari, A. C.; Bonaccorso, F.; Fal'Ko, V.; Novoselov, K. S.; Roche, S.; Bøggild, P.; Borini, S.; Koppens, F. H.; Palermo, V.; Pugno, N., et al. Science and technology roadmap for graphene, related two-dimensional crystals, and hybrid systems. *Nanoscale* **2015**, *7*, 4598–4810.
6. Bhimanapati, G. R.; Lin, Z.; Meunier, V.; Jung, Y.; Cha, J.; Das, S.; Xiao, D.; Son, Y.; Strano, M. S.; Cooper, V. R., et al. Recent advances in two-dimensional materials beyond graphene. *ACS nano* **2015**, *9*, 11509–11539.
7. Wallace, P. R. The band theory of graphite. *Physical review* **1947**, *71*, 622.
8. Novoselov, K. S.; Geim, A. K.; Morozov, S. V.; Jiang, D.-e.; Zhang, Y.; Dubonos, S. V.; Grigorieva, I. V.; Firsov, A. A. Electric field effect in atomically thin carbon films. *science* **2004**, *306*, 666–669.
9. Bolotin, K. I.; Sikes, K.; Jiang, Z.; Klima, M.; Fudenberg, G.; Hone, J.; Kim, P.; Stormer, H. L. Ultrahigh electron mobility in suspended graphene. *Solid state communications* **2008**, *146*, 351–355.
10. Balandin, A. A.; Ghosh, S.; Bao, W.; Calizo, I.; Teweldebrhan, D.; Miao, F.; Lau, C. N. Superior thermal conductivity of single-layer graphene. *Nano letters* **2008**, *8*, 902–907.
11. Lee, C.; Wei, X.; Kysar, J. W.; Hone, J. Measurement of the elastic properties and intrinsic strength of monolayer graphene. *Science* **2008**, *321*, 385–388.
12. Zhu, Y.; Murali, S.; Stoller, M. D.; Ganesh, K. J.; Cai, W.; Ferreira, P. J.; Pirkle, A.; Wallace, R. M.; Cychosz, K. A.; Thommes, M., et al. Carbon-based supercapacitors

produced by activation of graphene. *Science* **2011**, *332*, 1537–1541.

13. Kucinskis, G.; Bajars, G.; Kleperis, J. Graphene in lithium ion battery cathode materials: A review. *Journal of Power Sources* **2013**, *240*, 66–79.
14. Huang, Y.; Liang, J.; Chen, Y. An overview of the applications of graphene-based materials in supercapacitors. *small* **2012**, *8*, 1805–1834.
15. Wang, Y.; Wang, L.; Yang, T.; Li, X.; Zang, X.; Zhu, M.; Wang, K.; Wu, D.; Zhu, H. Wearable and highly sensitive graphene strain sensors for human motion monitoring. *Advanced Functional Materials* **2014**, *24*, 4666–4670.
16. Kulkarni, G. S.; Reddy, K.; Zhong, Z.; Fan, X. Graphene nanoelectronic heterodyne sensor for rapid and sensitive vapour detection. *Nature communications* **2014**, *5*, 4376.
17. Xu, S.; Zhan, J.; Man, B.; Jiang, S.; Yue, W.; Gao, S.; Guo, C.; Liu, H.; Li, Z.; Wang, J., et al. Real-time reliable determination of binding kinetics of DNA hybridization using a multi-channel graphene biosensor. *Nature communications* **2017**, *8*, 14902.
18. Jiang, T.; Sun, W.; Zhu, Q.; Burns, N. A.; Khan, S. A.; Mo, R.; Gu, Z. Furin-mediated sequential delivery of anticancer cytokine and small-molecule drug shuttled by graphene. *Advanced materials* **2015**, *27*, 1021–1028.
19. Yang, K.; Feng, L.; Liu, Z. Stimuli responsive drug delivery systems based on nano-graphene for cancer therapy. *Advanced drug delivery reviews* **2016**, *105*, 228–241.
20. Mahmoudi, T.; Wang, Y.; Hahn, Y.-B. Graphene and its derivatives for solar cells application. *Nano Energy* **2018**, *47*, 51–65.
21. Xia, F.; Mueller, T.; Lin, Y.-m.; Valdes-Garcia, A.; Avouris, P. Ultrafast graphene photodetector. *Nature nanotechnology* **2009**, *4*, 839–843.
22. Bonaccorso, F.; Sun, Z.; Hasan, T.; Ferrari, A. Graphene photonics and optoelectronics. *Nature photonics* **2010**, *4*, 611–622.
23. Nair, R. R.; Blake, P.; Grigorenko, A. N.; Novoselov, K. S.; Booth, T. J.; Stauber, T.; Peres, N. M.; Geim, A. K. Fine structure constant defines visual transparency of graphene. *science* **2008**, *320*, 1308–1308.
24. Elias, D. C.; Nair, R. R.; Mohiuddin, T.; Morozov, S.; Blake, P.; Halsall, M.; Ferrari, A. C.; Boukhvalov, D.; Katsnelson, M.; Geim, A., et al. Control of graphene's

properties by reversible hydrogenation: evidence for graphane. *Science* **2009**, *323*, 610–613.

25. Loh, K. P.; Bao, Q.; Eda, G.; Chhowalla, M. Graphene oxide as a chemically tunable platform for optical applications. *Nature chemistry* **2010**, *2*, 1015–1024.

26. Novoselov, K. S.; Jiang, D.; Schedin, F.; Booth, T.; Khotkevich, V.; Morozov, S.; Geim, A. K. Two-dimensional atomic crystals. *Proceedings of the National Academy of Sciences* **2005**, *102*, 10451–10453.

27. Mak, K. F.; Lee, C.; Hone, J.; Shan, J.; Heinz, T. F. Atomically thin MoS_2: a new direct-gap semiconductor. *Physical review letters* **2010**, *105*, 136805.

28. Manzeli, S.; Ovchinnikov, D.; Pasquier, D.; Yazyev, O. V.; Kis, A. 2D transition metal dichalcogenides. *Nature Reviews Materials* **2017**, *2*, 1–15.

29. Wang, Q. H.; Kalantar-Zadeh, K.; Kis, A.; Coleman, J. N.; Strano, M. S. Electronics and optoelectronics of two-dimensional transition metal dichalcogenides. *Nature nanotechnology* **2012**, *7*, 699–712.

30. Demirci, S.; Avazlı, N.; Durgun, E.; Cahangirov, S. Structural and electronic properties of monolayer group III monochalcogenides. *Physical Review B* **2017**, *95*, 115409.

31. Naguib, M.; Unocic, R. R.; Armstrong, B. L.; Nanda, J. Large-scale delamination of multi-layers transition metal carbides and carbonitrides "MXenes". *Dalton transactions* **2015**, *44*, 9353–9358.

32. Huang, K.; Li, Z.; Lin, J.; Han, G.; Huang, P. Two-dimensional transition metal carbides and nitrides (MXenes) for biomedical applications. *Chemical Society Reviews* **2018**, *47*, 5109–5124.

33. Schnering, H.; Wöhrle, H. Aufbau der halogenide und oxydhalogenide von Nb und Mo. *Angewandte Chemie* **1963**, *75*, 684–684.

34. Hillebrecht, H.; Schmidt, P.; Rotter, H.; Thiele, G.; Zönnchen, P.; Bengel, H.; Cantow, H.-J.; Magonov, S.; Whangbo, M.-H. Structural and scanning microscopy studies of layered compounds MCl3 (M= Mo, Ru, Cr) and $MOCl_2$ (m= V, Nb, Mo, Ru, Os). *Journal of alloys and compounds* **1997**, *246*, 70–79.

35. Ma, R.; Sasaki, T. Nanosheets of oxides and hydroxides: ultimate 2D charge-bearing functional crystallites. *Advanced materials* **2010**, *22*, 5082–5104.

36. Cahangirov, S.; Topsakal, M.; Aktürk, E.; Şahin, H.; Ciraci, S. Two-and one-dimensional honeycomb structures of silicon and germanium. *Physical review letters* **2009**, *102*, 236804.

37. Liu, C.-C.; Feng, W.; Yao, Y. Quantum spin Hall effect in silicene and two-dimensional germanium. *Physical review letters* **2011**, *107*, 076802.

38. Bianco, E.; Butler, S.; Jiang, S.; Restrepo, O. D.; Windl, W.; Goldberger, J. E. Stability and exfoliation of germanane: a germanium graphane analogue. *ACS nano* **2013**, *7*, 4414–4421.

39. Russ, B.; Glaudell, A.; Urban, J. J.; Chabinyc, M. L.; Segalman, R. A. Organic thermoelectric materials for energy harvesting and temperature control. *Nature Reviews Materials* **2016**, *1*, 1–14.

40. Fiori, G.; Bonaccorso, F.; Iannaccone, G.; Palacios, T.; Neumaier, D.; Seabaugh, A.; Banerjee, S. K.; Colombo, L. Electronics based on two-dimensional materials. *Nature nanotechnology* **2014**, *9*, 768–779.

41. Osada, M.; Sasaki, T. Exfoliated oxide nanosheets: new solution to nanoelectronics. *Journal of Materials Chemistry* **2009**, *19*, 2503–2511.

42. Osada, M.; Sasaki, T. Two-dimensional dielectric nanosheets: novel nanoelectronics from nanocrystal building blocks. *Advanced Materials* **2012**, *24*, 210–228.

43. Qiu, H.; Pan, L.; Yao, Z.; Li, J.; Shi, Y.; Wang, X. Electrical characterization of back-gated bi-layer MoS2 field-effect transistors and the effect of ambient on their performances. *Applied Physics Letters* **2012**, *100*.

44. Wu, S.-C.; Shan, G.; Yan, B. Prediction of near-room-temperature quantum anomalous Hall effect on honeycomb materials. *Physical review letters* **2014**, *113*, 256401.

45. Ajayan, P.; Kim, P.; Banerjee, K. Two-dimensional van der Waals materials. *Physics Today* **2016**, *69*, 38–44.

46. Ponraj, J. S.; Xu, Z.-Q.; Dhanabalan, S. C.; Mu, H.; Wang, Y.; Yuan, J.; Li, P.; Thakur, S.; Ashrafi, M.; Mccoubrey, K., et al. Photonics and optoelectronics of two-dimensional materials beyond graphene. *Nanotechnology* **2016**, *27*, 462001.

47. Akinwande, D.; Petrone, N.; Hone, J. Two-dimensional flexible nanoelectronics. *Nature communications* **2014**, *5*, 5678.

48. Li, L.; Yu, Y.; Ye, G. J.; Ge, Q.; Ou, X.; Wu, H.; Feng, D.; Chen, X. H.; Zhang, Y.

Black phosphorus field-effect transistors. *Nature nanotechnology* **2014**, *9*, 372–377.

49. Bridgman, P. Two new modifications of phosphorus. *Journal of the American chemical society* **1914**, *36*, 1344–1363.

50. Liu, H.; Neal, A. T.; Zhu, Z.; Tomanek, D.; Ye, P. D. Phosphorene: a new 2D material with high carrier mobility. *arXiv preprint arXiv:1401.4133* **2014**,

51. Warschauer, D. Electrical and optical properties of crystalline black phosphorus. *Journal of Applied Physics* **1963**, *34*, 1853–1860.

52. Akahama, Y.; Endo, S.; Narita, S.-i. Electrical properties of black phosphorus single crystals. *Journal of the Physical Society of Japan* **1983**, *52*, 2148–2155.

53. Morita, A. Semiconducting black phosphorus. *Applied Physics A* **1986**, *39*, 227–242.

54. Xia, F.; Wang, H.; Jia, Y. Rediscovering black phosphorus as an anisotropic layered material for optoelectronics and electronics. *Nature communications* **2014**, *5*, 4458.

55. Fei, R.; Yang, L. Strain-engineering the anisotropic electrical conductance of few-layer black phosphorus. *Nano letters* **2014**, *14*, 2884–2889.

56. Jiang, J.-W.; Park, H. S. Negative poisson's ratio in single-layer black phosphorus. *Nature communications* **2014**, *5*, 4727.

57. Mogulkoc, A.; Mogulkoc, Y.; Rudenko, A.; Katsnelson, M. Polaronic effects in monolayer black phosphorus on polar substrates. *Physical Review B* **2016**, *93*, 085417.

58. Li, L.; Bacaksiz, C.; Nakhaee, M.; Pentcheva, R.; Peeters, F.; Yagmurcukardes, M. Single-layer Janus black arsenic-phosphorus (b-AsP): Optical dichroism, anisotropic vibrational, thermal, and elastic properties. *Physical Review B* **2020**, *101*, 134102.

59. Allain, A.; Kang, J.; Banerjee, K.; Kis, A. Electrical contacts to two-dimensional semiconductors. *Nature materials* **2015**, *14*, 1195–1205.

60. Vannucci, L.; Petralanda, U.; Rasmussen, A.; Olsen, T.; Thygesen, K. S. Anisotropic properties of monolayer 2D materials: An overview from the C2DB database. *Journal of Applied Physics* **2020**, *128*.

61. Amani, M.; Regan, E.; Bullock, J.; Ahn, G. H.; Javey, A. Mid-wave infrared photoconductors based on black phosphorus-arsenic alloys. *ACS nano* **2017**, *11*, 11724–11731.

62. Abudukelimu, A.; Kakushima, K.; Ahmet, P.; Geni, M.; Tsutsui, K.; Nishiyama, A.;

Sugii, N.; Natori, K.; Hattori, T.; Iwai, H. The effect of isotropic and anisotropic scattering in drain region of ballistic channel diode. 2010 10th IEEE International Conference on Solid-State and Integrated Circuit Technology. 2010; pp 1247–1249.

63. Liu, E.; Fu, Y.; Wang, Y.; Feng, Y.; Liu, H.; Wan, X.; Zhou, W.; Wang, B.; Shao, L.; Ho, C.-H., et al. Integrated digital inverters based on two-dimensional anisotropic ReS_2 field-effect transistors. *Nature communications* **2015**, *6*, 1–7.

64. Yuan, H.; Liu, X.; Afshinmanesh, F.; Li, W.; Xu, G.; Sun, J.; Lian, B.; Curto, A. G.; Ye, G.; Hikita, Y., et al. Polarization-sensitive broadband photodetector using a black phosphorus vertical p–n junction. *Nature nanotechnology* **2015**, *10*, 707–713.

65. Zhou, W.; Chen, J.; Bai, P.; Guo, S.; Zhang, S.; Song, X.; Tao, L.; Zeng, H. Two-dimensional pnictogen for field-effect transistors. *Research* **2019**,

66. Shahbazi, M.-A.; Faghfouri, L.; Ferreira, M. P.; Figueiredo, P.; Maleki, H.; Sefat, F.; Hirvonen, J.; Santos, H. A. The versatile biomedical applications of bismuth-based nanoparticles and composites: therapeutic, diagnostic, biosensing, and regenerative properties. *Chemical Society Reviews* **2020**, *49*, 1253–1321.

67. Ersan, F.; Keçik, D.; Özçelik, V.; Kadioglu, Y.; Aktürk, O. Ü.; Durgun, E.; Aktürk, E.; Ciraci, S. Two-dimensional pnictogens: A review of recent progresses and future research directions. *Applied Physics Reviews* **2019**, *6*.

68. Wu, M.; Xu, B.; Zhang, Y.; Qi, S.; Ni, W.; Hu, J.; Ma, J. Perspectives in emerging bismuth electrochemistry. *Chemical Engineering Journal* **2020**, *381*, 122558.

69. Liu, X.; Zhang, S.; Guo, S.; Cai, B.; Yang, S. A.; Shan, F.; Pumera, M.; Zeng, H. Advances of 2D bismuth in energy sciences. *Chemical Society Reviews* **2020**, *49*, 263–285.

70. Kim, J.; Shim, W.; Lee, W. Bismuth nanowire thermoelectrics. *Journal of Materials Chemistry C* **2015**, *3*, 11999–12013.

71. Singh, S.; Zanolli, Z.; Amsler, M.; Belhadji, B.; Sofo, J. O.; Verstraete, M. J.; Romero, A. H. Low-energy phases of bi monolayer predicted by structure search in two dimensions. *The Journal of Physical Chemistry Letters* **2019**, *10*, 7324–7332.

72. Gou, J.; Bai, H.; Zhang, X.; Huang, Y. L.; Duan, S.; Ariando, A.; Yang, S. A.; Chen, L.; Lu, Y.; Wee, A. T. S. Two-dimensional ferroelectricity in a single-element bismuth monolayer. *Nature* **2023**, *617*, 67–72.

73. Reis, F.; Li, G.; Dudy, L.; Bauernfeind, M.; Glass, S.; Hanke, W.; Thomale, R.;

Schäfer, J.; Claessen, R. Bismuthene on a SiC substrate: A candidate for a high-temperature quantum spin Hall material. *Science* **2017**, *357*, 287–290.

74. Lu, Y.; Xu, W.; Zeng, M.; Yao, G.; Shen, L.; Yang, M.; Luo, Z.; Pan, F.; Wu, K.; Das, T., et al. Topological properties determined by atomic buckling in self-assembled ultrathin Bi (110). *Nano letters* **2015**, *15*, 80–87.

75. Aguilera, I.; Friedrich, C.; Blügel, S. Electronic phase transitions of bismuth under strain from relativistic self-consistent G W calculations. *Physical Review B* **2015**, *91*, 125129.

76. Wang, X.; Xu, C.; Hu, H.; Wang, P.; Bian, G.; Tan, W.; Brown, S.; Chiang, T.-C. Topological phase stability and transformation of bismuthene. *Europhysics Letters* **2017**, *119*, 27002.

77. Kong, X.; Liu, Q.; Zhang, C.; Peng, Z.; Chen, Q. Elemental two-dimensional nanosheets beyond graphene. *Chemical Society Reviews* **2017**, *46*, 2127–2157.

78. Lu, L.; Wang, W.; Wu, L.; Jiang, X.; Xiang, Y.; Li, J.; Fan, D.; Zhang, H. All-optical switching of two continuous waves in few layer bismuthene based on spatial cross-phase modulation. *Acs Photonics* **2017**, *4*, 2852–2861.

79. Guo, Q.; Pospischil, A.; Bhuiyan, M.; Jiang, H.; Tian, H.; Farmer, D.; Deng, B.; Li, C.; Han, S.-J.; Wang, H., et al. Black phosphorus mid-infrared photodetectors with high gain. *Nano letters* **2016**, *16*, 4648–4655.

80. Wu, R.; Ma, J.-Z.; Nie, S.-M.; Zhao, L.-X.; Huang, X.; Yin, J.-X.; Fu, B.-B.; Richard, P.; Chen, G.-F.; Fang, Z., et al. Evidence for topological edge states in a large energy gap near the step edges on the surface of ZrTe 5. *Physical Review X* **2016**, *6*, 021017.

81. Jin, Y.; Li, X.; Yang, J. Single layer of MX_3 (M= Ti, Zr; X= S, Se, Te): A new platform for nano-electronics and optics. *Physical Chemistry Chemical Physics* **2015**, *17*, 18665–18669.

82. Zhao, Q.; Guo, Y.; Zhou, Y.; Yao, Z.; Ren, Z.; Bai, J.; Xu, X. Band alignments and heterostructures of monolayer transition metal trichalcogenides MX_3 (M= Zr, Hf; X= S, Se) and dichalcogenides MX_2 (M= Tc, Re; X= S, Se) for solar applications. *Nanoscale* **2018**, *10*, 3547–3555.

83. Dai, J.; Li, M.; Zeng, X. C. Group IVB transition metal trichalcogenides: a new class of 2D layered materials beyond graphene. *Wiley Interdisciplinary Reviews:*

Computational Molecular Science **2016**, *6*, 211–222.

84. Balandin, A. A.; Kargar, F.; Salguero, T. T.; Lake, R. K. One-dimensional van der Waals quantum materials. *Materials Today* **2022**, *55*, 74–91.

85. Island, J. O.; Biele, R.; Barawi, M.; Clamagirand, J. M.; Ares, J. R.; Sánchez, C.; Van Der Zant, H. S.; Ferrer, I. J.; D'Agosta, R.; Castellanos-Gomez, A. Titanium trisulfide (TiS_3): a 2D semiconductor with quasi-1D optical and electronic properties. *Scientific reports* **2016**, *6*, 22214.

86. Stolyarov, M. A.; Liu, G.; Bloodgood, M. A.; Aytan, E.; Jiang, C.; Samnakay, R.; Salguero, T. T.; Nika, D. L.; Rumyantsev, S. L.; Shur, M. S., et al. Breakdown current density in h-BN-capped quasi-1D $TaSe_3$ metallic nanowires: prospects of interconnect applications. *Nanoscale* **2016**, *8*, 15774–15782.

87. Geremew, A.; Bloodgood, M.; Aytan, E.; Woo, B.; Corber, S.; Liu, G.; Bozhilov, K.; Salguero, T.; Rumyantsev, S.; Rao, M., et al. Current carrying capacity of quasi-1D $ZrTe_3$ van der Waals nanoribbons. *IEEE Electron Device Letters* **2018**, *39*, 735–738.

88. Wu, W.; Wang, Y.; Niu, Y.; Wang, P.; Chen, M.; Sun, J.; Wang, N.; Wu, D.; Zhao, Z. Thermal localization enhanced fast photothermoelectric response in a quasi-one-dimensional flexible NbS_3 photodetector. *ACS applied materials & interfaces* **2020**, *12*, 14165–14173.

89. Valbuena, M. Á.; Chudzinski, P.; Pons, S.; Conejeros, S.; Alemany, P.; Canadell, E.; Berger, H.; Frantzeskakis, E.; Ávila, J.; Asensio, M. C., et al. Polarization dependence of angle-resolved photoemission with submicron spatial resolution reveals emerging one-dimensionality of electrons in $NbSe_3$. *Physical Review B* **2019**, *99*, 075118.

90. Island, J. O.; Molina-Mendoza, A. J.; Barawi, M.; Biele, R.; Flores, E.; Clamagirand, J. M.; Ares, J. R.; Sánchez, C.; Van Der Zant, H. S.; D'Agosta, R., et al. Electronics and optoelectronics of quasi-1D layered transition metal trichalcogenides. *2D Materials* **2017**, *4*, 022003.

91. Saeed, Y.; Kachmar, A.; Carignano, M. A. First-principles study of the transport properties in bulk and monolayer MX_3 (M= Ti, Zr, Hf and X= S, Se) compounds. *The Journal of Physical Chemistry C* **2017**, *121*, 1399–1403.

92. Lipatov, A.; Wilson, P. M.; Shekhirev, M.; Teeter, J. D.; Netusil, R.; Sinitskii, A. Few-layered titanium trisulfide (TiS_3) field-effect transistors. *Nanoscale* **2015**, *7*,

12291–12296.

93. Xie, J.; Wang, R.; Bao, J.; Zhang, X.; Zhang, H.; Li, S.; Xie, Y. Zirconium trisulfide ultrathin nanosheets as efficient catalysts for water oxidation in both alkaline and neutral solutions. *Inorganic Chemistry Frontiers* **2014**, *1*, 751–756.

94. Li, W.; Yang, L.; Wang, J.; Xiang, B.; Yu, Y. Three-dimensionally interconnected TaS_3 nanowire network as anode for high-performance flexible Li-ion battery. *ACS Applied Materials & Interfaces* **2015**, *7*, 5629–5633.

95. Golovnya, A.; Pokrovskii, V. Y.; Shadrin, P. Coupling of the Lattice and Superlattice Deformations and Hysteresis in Thermal Expansion for the Quasi-One-Dimensional Conductor TaS_3. *Physical review letters* **2002**, *88*, 246401.

96. Levy, F.; Berger, H. Single crystals of transition metal trichalcogenides. *Journal of Crystal Growth* **1983**, *61*, 61–68.

97. Miller Jr, J. H.; Suárez-Villagrán, M. Y.; Sanderson, J. O. Quantum transport of charge density wave electrons in layered materials. *Materials Today Physics* **2024**, *41*, 101326.

98. Roucau, C.; Ayroles, R.; Monceau, P.; Guemas, L.; Meerschaut, A.; Rouxel, J. Electron diffraction and resistivity measurements on the one-dimensional orthorhombic and monoclinic structures of TaS_3. comparison with $NbSe_3$. *physica status solidi (a)* **1980**, *62*, 483–493.

99. Sridhar, S.; Reagor, D.; Gruner, G. Inertial Dynamics of Charge-Density Waves in TaS_3 and $NbSe_3$. *Physical review letters* **1985**, *55*, 1196.

100. Wilson, J. Bands, bonds, and charge-density waves in the $NbSe_3$ family of compounds. *Physical Review B* **1979**, *19*, 6456.

101. Monteverde, M.; Lorenzana, J.; Monceau, P.; Nunez-Regueiro, M. Quantum critical point and superconducting dome in the pressure phase diagram of o-TaS_3. *Physical Review B* **2013**, *88*, 180504.

102. Preobrazhensky, V.; Taldenkov, A. Electronic structure and transport properties of uniaxially deformed m-TaS_3. *Le Journal de Physique IV* **1993**, *3*, C2–57.

103. Hasan, M. Z.; Kane, C. L. Colloquium: topological insulators. *Reviews of modern physics* **2010**, *82*, 3045.

104. Ando, Y. Topological insulator materials. *Journal of the Physical Society of Japan*

2013, *82*, 102001.

105. Kane, C. L.; Mele, E. J. Quantum spin Hall effect in graphene. *Physical review letters* **2005**, *95*, 226801.

106. Bernevig, B. A.; Zhang, S.-C. Quantum spin Hall effect. *Physical review letters* **2006**, *96*, 106802.

107. Weng, H.; Fang, C.; Fang, Z.; Bernevig, B. A.; Dai, X. Weyl semimetal phase in noncentrosymmetric transition-metal monophosphides. *Physical Review X* **2015**, *5*, 011029.

108. Okada, S.; Sambongi, T.; Ido, M. Giant resistivity anomaly in $ZrTe_5$. *journal of the physical society of japan* **1980**, *49*, 839–840.

109. DiSalvo, F.; Fleming, R.; Waszczak, J. Possible phase transition in the quasi-one-dimensional materials $ZrTe_5$ or $HfTe_5$. *Physical Review B* **1981**, *24*, 2935.

110. Tritt, T. M.; Lowhorn, N. D.; Littleton IV, R.; Pope, A.; Feger, C.; Kolis, J. Large enhancement of the resistive anomaly in the pentatelluride materials $HfTe_5$ and $ZrTe_5$ with applied magnetic field. *Physical Review B* **1999**, *60*, 7816.

111. Klitzing, K. v.; Dorda, G.; Pepper, M. New method for high-accuracy determination of the fine-structure constant based on quantized Hall resistance. *Physical review letters* **1980**, *45*, 494.

112. Konig, M.; Wiedmann, S.; Brune, C.; Roth, A.; Buhmann, H.; Molenkamp, L. W.; Qi, X.-L.; Zhang, S.-C. Quantum spin Hall insulator state in HgTe quantum wells. *Science* **2007**, *318*, 766–770.

113. Li, Q.; Kharzeev, D. E.; Zhang, C.; Huang, Y.; Pletikosić, I.; Fedorov, A.; Zhong, R.; Schneeloch, J.; Gu, G.; Valla, T. Chiral magnetic effect in $ZrTe_5$. *Nature Physics* **2016**, *12*, 550–554.

114. Liang, T.; Lin, J.; Gibson, Q.; Kushwaha, S.; Liu, M.; Wang, W.; Xiong, H.; Sobota, J. A.; Hashimoto, M.; Kirchmann, P. S., et al. Anomalous hall effect in $ZrTe_5$. *Nature Physics* **2018**, *14*, 451–455.

115. Zhou, Y.; Wu, J.; Ning, W.; Li, N.; Du, Y.; Chen, X.; Zhang, R.; Chi, Z.; Wang, X.; Zhu, X., et al. Pressure-induced superconductivity in a three-dimensional topological material ZrTe5. *Proceedings of the National Academy of Sciences* **2016**, *113*, 2904–2909.

116. Zhang, W.; Wang, P.; Skinner, B.; Bi, R.; Kozii, V.; Cho, C.-W.; Zhong, R.; Schneeloch, J.; Yu, D.; Gu, G., et al. Observation of a thermoelectric Hall plateau in the extreme quantum limit. *Nature communications* **2020**, *11*, 1046.

117. Whangbo, M.-H.; DiSalvo, F.; Fleming, R. Electronic structure of $ZrTe_5$. *Physical Review B* **1982**, *26*, 687.

118. McIlroy, D.; Moore, S.; Zhang, D.; Wharton, J.; Kempton, B.; Littleton, R.; Wilson, M.; Tritt, T.; Olson, C. Observation of a semimetal–semiconductor phase transition in the intermetallic $ZrTe_5$. *Journal of Physics: Condensed Matter* **2004**, *16*, L359.

119. Kamm, G.; Gillespie, D.; Ehrlich, A.; Wieting, T.; Levy, F. Fermi surface, effective masses, and Dingle temperatures of $ZrTe_5$ as derived from the Shubnikov–de Haas effect. *Physical Review B* **1985**, *31*, 7617.

120. Manzoni, G.; Gragnaniello, L.; Autès, G.; Kuhn, T.; Sterzi, A.; Cilento, F.; Zacchigna, M.; Enenkel, V.; Vobornik, I.; Barba, L., et al. Evidence for a strong topological insulator phase in $ZrTe_5$. *Physical review letters* **2016**, *117*, 237601.

121. Weng, H.; Dai, X.; Fang, Z. Transition-metal pentatelluride $ZrTe_5$ and $HfTe_5$: A paradigm for large-gap quantum spin Hall insulators. *Physical review X* **2014**, *4*, 011002.

122. Li, X.-B.; Huang, W.-K.; Lv, Y.-Y.; Zhang, K.-W.; Yang, C.-L.; Zhang, B.-B.; Chen, Y.; Yao, S.-H.; Zhou, J.; Lu, M.-H., et al. Experimental observation of topological edge states at the surface step edge of the topological insulator $ZrTe_5$. *Physical review letters* **2016**, *116*, 176803.

123. Shahi, P.; Singh, D.; Sun, J.; Zhao, L.; Chen, G.; Lv, Y.; Li, J.; Yan, J.-Q.; Mandrus, D.; Cheng, J.-G. Bipolar conduction as the possible origin of the electronic transition in pentatellurides: metallic vs semiconducting behavior. *Physical Review X* **2018**, *8*, 021055.

124. Tang, F.; Wang, P.; Wang, P.; Gan, Y.; Wang, L.; Zhang, W.; Zhang, L. Multi-carrier transport in $ZrTe_5$ film. *Chinese Physics B* **2018**, *27*, 087307.

125. Wang, W.; Zhang, X.; Xu, H.; Zhao, Y.; Zou, W.; He, L.; Xu, Y. Evidence for layered quantized transport in Dirac semimetal $ZrTe_5$. *Scientific Reports* **2018**, *8*, 5125.

126. Hu, J.; Caputo, M.; Guedes, E. B.; Tu, S.; Martino, E.; Magrez, A.; Berger, H.;

Dil, J. H.; Yu, H.; Ansermet, J.-P. Large magnetothermopower and anomalous Nernst effect in $HfTe_5$. *Physical Review B* **2019**, *100*, 115201.

127. Galeski, S.; Zhao, X.; Wawrzyńczak, R.; Meng, T.; Förster, T.; Lozano, P.; Honnali, S.; Lamba, N.; Ehmcke, T.; Markou, A., et al. Unconventional Hall response in the quantum limit of $HfTe_5$. *Nature communications* **2020**, *11*, 5926.
128. Jia, K.; Yang, C.-L.; Wang, M.-S.; Ma, X.-G. High thermoelectric figure of merit and thermopower of $HfTe_5$ at room temperature. *Journal of Physics: Condensed Matter* **2020**, *32*, 345501.
129. Zhao, L.-X.; Huang, X.-C.; Long, Y.-J.; Chen, D.; Liang, H.; Yang, Z.-H.; Xue, M.-Q.; Ren, Z.-A.; Weng, H.-M.; Fang, Z., et al. Anomalous magneto-transport behavior in transition metal Pentatelluride $HfTe_5$. *Chinese Physics Letters* **2017**, *34*, 037102.
130. Rubinstein, M. $HfTe_5$ and $ZrTe_5$: Possible polaronic conductors. *Physical Review B* **1999**, *60*, 1627.
131. Wang, C. Thermodynamically induced transport anomaly in dilute metals $ZrTe_5$ and $HfTe_5$. *Physical Review Letters* **2021**, *126*, 126601.
132. Yazyev, O. V.; Helm, L. Defect-induced magnetism in graphene. *Physical Review B* **2007**, *75*, 125408.
133. Santos, E. J.; Sánchez-Portal, D.; Ayuela, A. Magnetism of substitutional Co impurities in graphene: Realization of single π vacancies. *Physical Review B* **2010**, *81*, 125433.
134. Krasheninnikov, A.; Lehtinen, P.; Foster, A. S.; Pyykkö, P.; Nieminen, R. M. Embedding transition-metal atoms in graphene: structure, bonding, and magnetism. *Physical review letters* **2009**, *102*, 126807.
135. Lee, J. E.; Ahn, G.; Shim, J.; Lee, Y. S.; Ryu, S. Optical separation of mechanical strain from charge doping in graphene. *Nature communications* **2012**, *3*, 1024.
136. Şahin, H.; Ataca, C.; Ciraci, S. Electronic and magnetic properties of graphane nanoribbons. *Physical Review B* **2010**, *81*, 205417.
137. Magda, G. Z.; Jin, X.; Hagymási, I.; Vancsó, P.; Osváth, Z.; Nemes-Incze, P.; Hwang, C.; Biró, L. P.; Tapasztó, L. Room-temperature magnetic order on zigzag edges of narrow graphene nanoribbons. *Nature* **2014**, *514*, 608–611.

138. Ataca, C.; Sahin, H.; Akturk, E.; Ciraci, S. Mechanical and electronic properties of MoS_2 nanoribbons and their defects. *The Journal of Physical Chemistry C* **2011**, *115*, 3934–3941.

139. Huang, B.; Clark, G.; Navarro-Moratalla, E.; Klein, D. R.; Cheng, R.; Seyler, K. L.; Zhong, D.; Schmidgall, E.; McGuire, M. A.; Cobden, D. H., et al. Layer-dependent ferromagnetism in a van der Waals crystal down to the monolayer limit. *Nature* **2017**, *546*, 270–273.

140. Gong, C.; Li, L.; Li, Z.; Ji, H.; Stern, A.; Xia, Y.; Cao, T.; Bao, W.; Wang, C.; Wang, Y., et al. Discovery of intrinsic ferromagnetism in two-dimensional van der Waals crystals. *Nature* **2017**, *546*, 265–269.

141. Wang, X.; Tang, J.; Xia, X.; He, C.; Zhang, J.; Liu, Y.; Wan, C.; Fang, C.; Guo, C.; Yang, W., et al. Current-driven magnetization switching in a van der Waals ferromagnet Fe_3GeTe_2. *Science advances* **2019**, *5*, 8904.

142. Dieny, B.; Chshiev, M. Perpendicular magnetic anisotropy at transition metal/oxide interfaces and applications. *Reviews of Modern Physics* **2017**, *89*, 025008.

143. Ikeda, S.; Miura, K.; Yamamoto, H.; Mizunuma, K.; Gan, H.; Endo, M.; Kanai, S.; Hayakawa, J.; Matsukura, F.; Ohno, H. A perpendicular-anisotropy CoFeB–MgO magnetic tunnel junction. *Nature materials* **2010**, *9*, 721–724.

144. O'Hara, D. J.; Zhu, T.; Trout, A. H.; Ahmed, A. S.; Luo, Y. K.; Lee, C. H.; Brenner, M. R.; Rajan, S.; Gupta, J. A.; McComb, D. W., et al. Room temperature intrinsic ferromagnetism in epitaxial manganese selenide films in the monolayer limit. *Nano letters* **2018**, *18*, 3125–3131.

145. Yu, W.; Li, J.; Herng, T. S.; Wang, Z.; Zhao, X.; Chi, X.; Fu, W.; Abdelwahab, I.; Zhou, J.; Dan, J., et al. Chemically exfoliated VSe_2 monolayers with room-temperature ferromagnetism. *Advanced Materials* **2019**, *31*, 1903779.

146. Hu, X.; Zhao, Y.; Shen, X.; Krasheninnikov, A. V.; Chen, Z.; Sun, L. Enhanced ferromagnetism and tunable magnetism in Fe_3GeTe_2 monolayer by strain engineering. *ACS applied materials & interfaces* **2020**, *12*, 26367–26373.

147. Lee, K.; Dismukes, A. H.; Telford, E. J.; Wiscons, R. A.; Wang, J.; Xu, X.; Nuckolls, C.; Dean, C. R.; Roy, X.; Zhu, X. Magnetic order and symmetry in the 2D semiconductor CrSBr. *Nano Letters* **2021**, *21*, 3511–3517.

148. Baltz, V.; Manchon, A.; Tsoi, M.; Moriyama, T.; Ono, T.; Tserkovnyak, Y. Antifer-

romagnetic spintronics. *Reviews of Modern Physics* **2018**, *90*, 015005.

149. Bunkov, Y. M.; Alakshin, E.; Gazizulin, R.; Klochkov, A.; Kuzmin, V.; L'vov, V.; Tagirov, M. High-T_c spin superfluidity in antiferromagnets. *Physical review letters* **2012**, *108*, 177002.

150. Ivády, V.; Simon, T.; Maze, J. R.; Abrikosov, I.; Gali, A. Pressure and temperature dependence of the zero-field splitting in the ground state of NV centers in diamond: A first-principles study. *Physical Review B* **2014**, *90*, 235205.

151. Kašpar, Z.; Surỳnek, M.; Zubáč, J.; Krizek, F.; Novák, V.; Campion, R. P.; Wörnle, M. S.; Gambardella, P.; Marti, X.; Němec, P., et al. Quenching of an antiferromagnet into high resistivity states using electrical or ultrashort optical pulses. *Nature Electronics* **2021**, *4*, 30–37.

152. Dewhurst, J. K.; Elliott, P.; Shallcross, S.; Gross, E. K.; Sharma, S. Laser-induced intersite spin transfer. *Nano letters* **2018**, *18*, 1842–1848.

153. Tzschaschel, C.; Otani, K.; Iida, R.; Shimura, T.; Ueda, H.; Günther, S.; Fiebig, M.; Satoh, T. Ultrafast optical excitation of coherent magnons in antiferromagnetic NiO. *Physical Review B* **2017**, *95*, 174407.

154. Olejník, K.; Seifert, T.; Kašpar, Z.; Novák, V.; Wadley, P.; Campion, R. P.; Baumgartner, M.; Gambardella, P.; Němec, P.; Wunderlich, J., et al. Terahertz electrical writing speed in an antiferromagnetic memory. *Science advances* **2018**, *4*, eaar3566.

155. Pramoda, K.; Rao, C. 2D transition metal-based phospho-chalcogenides and their applications in photocatalytic and electrocatalytic hydrogen evolution reactions. *Journal of Materials Chemistry A* **2023**, *11*, 16933–16962.

156. Samal, R.; Sanyal, G.; Chakraborty, B.; Rout, C. S. Two-dimensional transition metal phosphorous trichalcogenides (MPX_3): a review on emerging trends, current state and future perspectives. *Journal of Materials Chemistry A* **2021**, *9*, 2560–2591.

157. Joy, P.; Vasudevan, S. Magnetism in the layered transition-metal thiophosphates MPS_3 (M= Mn, Fe, and Ni). *Physical Review B* **1992**, *46*, 5425.

158. Ressouche, E.; Loire, M.; Simonet, V.; Ballou, R.; Stunault, A.; Wildes, A. Magnetoelectric $MnPS_3$ as a candidate for ferrotoroidicity. *Physical Review B* **2010**, *82*, 100408.

159. Xue, M.; He, W.; Gong, Q.; Yi, M.; Guo, W. Nonlinear elasticity and strain-tunable magnetocalorics of antiferromagnetic monolayer $MnPS_3$. *Extreme Mechanics Let-*

ters **2022**, *57*, 101900.

160. Kurosawa, K.; Saito, S.; Yamaguchi, Y. Neutron diffraction study on $MnPS_3$ and $FePS_3$. *Journal of the Physical Society of Japan* **1983**, *52*, 3919–3926.

161. Long, G.; Zhang, T.; Cai, X.; Hu, J.; Cho, C.-w.; Xu, S.; Shen, J.; Wu, Z.; Han, T.; Lin, J., et al. Isolation and characterization of few-layer manganese thiophosphite. *ACS nano* **2017**, *11*, 11330–11336.

162. Du, K.-z.; Wang, X.-z.; Liu, Y.; Hu, P.; Utama, M. I. B.; Gan, C. K.; Xiong, Q.; Kloc, C. Weak van der Waals stacking, wide-range band gap, and Raman study on ultrathin layers of metal phosphorus trichalcogenides. *ACS nano* **2016**, *10*, 1738–1743.

163. Neal, S. N.; Kim, H.-S.; Smith, K. A.; Haglund, A. V.; Mandrus, D. G.; Bechtel, H. A.; Carr, G. L.; Haule, K.; Vanderbilt, D.; Musfeldt, J. L. Near-field infrared spectroscopy of monolayer $MnPS_3$. *Physical Review B* **2019**, *100*, 075428.

164. Shiomi, Y.; Takashima, R.; Saitoh, E. Experimental evidence consistent with a magnon Nernst effect in the antiferromagnetic insulator $MnPS_3$. *Physical Review B* **2017**, *96*, 134425.

165. Xiao, R.-C.; Shao, D.-F.; Li, Y.-H.; Jiang, H. Spin photogalvanic effect in two-dimensional collinear antiferromagnets. *npj Quantum Materials* **2021**, *6*, 35.

166. Li, X.; Cao, T.; Niu, Q.; Shi, J.; Feng, J. Coupling the valley degree of freedom to antiferromagnetic order. *Proceedings of the National Academy of Sciences* **2013**, *110*, 3738–3742.

167. Takashima, R.; Shiomi, Y.; Motome, Y. Nonreciprocal spin Seebeck effect in antiferromagnets. *Physical Review B* **2018**, *98*, 020401.

168. Kresse, G.; Furthmüller, J. Efficient iterative schemes for ab initio total-energy calculations using a plane-wave basis set. *Physical review B* **1996**, *54*, 11169.

169. Perdew, J. P.; Burke, K.; Ernzerhof, M. Generalized gradient approximation made simple. *Physical review letters* **1996**, *77*, 3865.

170. Heyd, J.; Scuseria, G. E.; Ernzerhof, M. Hybrid functionals based on a screened Coulomb potential. *The Journal of chemical physics* **2003**, *118*, 8207–8215.

171. Grimme, S.; Antony, J.; Ehrlich, S.; Krieg, H. A consistent and accurate ab initio parametrization of density functional dispersion correction (DFT-D) for the 94

elements H-Pu. *The Journal of chemical physics* **2010**, *132*.

172. Henkelman, G.; Arnaldsson, A.; Jónsson, H. A fast and robust algorithm for Bader decomposition of charge density. *Computational Materials Science* **2006**, *36*, 354–360.

173. Alfè, D. PHON: A program to calculate phonons using the small displacement method. *Computer Physics Communications* **2009**, *180*, 2622–2633.

174. Fjellvåg, H.; Kjekshus, A. Structural properties of $ZrTe_5$ and $HfTe_5$ as seen by powder diffraction. *Solid State Communications* **1986**, *60*, 91–93.

175. Liu, Y.; Chen, M.; Yang, S. Chemical functionalization of 2D black phosphorus. *InfoMat* **2021**, *3*, 231–251.

176. Frisk, A.; Duffy, L. B.; Zhang, S.; van der Laan, G.; Hesjedal, T. Magnetic X-ray spectroscopy of two-dimensional CrI_3 layers. *Materials Letters* **2018**, *232*, 5–7.

177. Manzoni, G.; Crepaldi, A.; Autès, G.; Sterzi, A.; Cilento, F.; Akrap, A.; Vobornik, I.; Gragnaniello, L.; Bugnon, P.; Fonin, M., et al. Temperature dependent non-monotonic bands shift in $ZrTe_5$. *Journal of Electron Spectroscopy and Related Phenomena* **2017**, *219*, 9–15.

178. Tobar, Á. H.; López, C. O.; Martínez, J. A. R., et al. Study of the structural and electronic properties of three-and two-dimensional transition-metal dioxides using first-principles calculations. *Computational Condensed Matter* **2020**, *25*, e00498.

179. Mortazavi, B.; Shojaei, F.; Yagmurcukardes, M.; Makaremi, M.; Zhuang, X. A theoretical investigation on the physical properties of zirconium trichalcogenides, ZrS_3, $ZrSe_3$ and $ZrTe_3$ monolayers. *Energies* **2022**, *15*, 5479.

180. Wang, L.; Kutana, A.; Zou, X.; Yakobson, B. I. Electro-mechanical anisotropy of phosphorene. *Nanoscale* **2015**, *7*, 9746–9751.

181. Qiu, G.; Du, Y.; Charnas, A.; Zhou, H.; Jin, S.; Luo, Z.; Zemlyanov, D. Y.; Xu, X.; Cheng, G. J.; Ye, P. D. Observation of optical and electrical in-plane anisotropy in high-mobility few-layer $ZrTe_5$. *Nano Letters* **2016**, *16*, 7364–7369.

182. Qiao, J.; Kong, X.; Hu, Z.-X.; Yang, F.; Ji, W. High-mobility transport anisotropy and linear dichroism in few-layer black phosphorus. *Nature communications* **2014**, *5*, 4475.

183. Born, M.; Huang, K.; Lax, M. Dynamical theory of crystal lattices. *American Jour-*

nal of Physics **1955**, *23*, 474–474.

184. Bhattacharya, D.; Jana, D. Worm-graphene: A two-dimensional orthorhombic carbon semimetal with massless Dirac fermion. *Applied Surface Science* **2022**, *585*, 152457.

185. Yagmurcukardes, M.; Senger, R. T.; Peeters, F. M.; Sahin, H. Mechanical properties of monolayer GaS and GaSe crystals. *Physical Review B* **2016**, *94*, 245407.

186. Lin, Z.; McCreary, A.; Briggs, N.; Subramanian, S.; Zhang, K.; Sun, Y.; Li, X.; Borys, N. J.; Yuan, H.; Fullerton-Shirey, S. K., et al. 2D materials advances: from large scale synthesis and controlled heterostructures to improved characterization techniques, defects and applications. *2D Materials* **2016**, *3*, 042001.

187. Rhodes, D.; Chae, S. H.; Ribeiro-Palau, R.; Hone, J. Disorder in van der Waals heterostructures of 2D materials. *Nature materials* **2019**, *18*, 541–549.

188. Wang, G.; Pandey, R.; Karna, S. P. Physics and chemistry of oxidation of two-dimensional nanomaterials by molecular oxygen. *Wiley Interdisciplinary Reviews: Computational Molecular Science* **2017**, *7*, e1280.

189. Abdulsalam, M.; Joubert, D. P. Structural and electronic properties of MX_3 (M= Ti, Zr and Hf; X= S, Se, Te) from first principles calculations. *The European Physical Journal B* **2015**, *88*, 1–11.

190. Xiao, W.-Z.; Xiao, G.; Rong, Q.-Y.; Wang, L.-L. New two-dimensional VV binary compounds with a honeycomb-like structure: a first-principles study. *Materials Research Express* **2018**, *5*, 035903.

191. Guo, Y.; Zhu, H.; Wang, Q. Large Second Harmonic Generation in Elemental α-Sb and α-Bi Monolayers. *The Journal of Physical Chemistry C* **2020**, *124*, 5506–5513.

192. Xiao, C.; Wang, F.; Yang, S. A.; Lu, Y.; Feng, Y.; Zhang, S. Elemental ferroelectricity and antiferroelectricity in Group-V monolayer. *Advanced Functional Materials* **2018**, *28*, 1707383.

193. Wu, Z.-j.; Zhao, E.-j.; Xiang, H.-p.; Hao, X.-f.; Liu, X.-j.; Meng, J. Crystal structures and elastic properties of superhard IrN_2 and IrN_3 from first principles. *Physical Review B* **2007**, *76*, 054115.

194. Şahin, H.; Cahangirov, S.; Topsakal, M.; Bekaroglu, E.; Akturk, E.; Senger, R. T.; Ciraci, S. Monolayer honeycomb structures of group-IV elements and III-V binary compounds: First-principles calculations. *Physical Review B* **2009**, *80*, 155453.

195. Han, J.; Xie, J.; Zhang, Z.; Yang, D.; Si, M.; Xue, D. Negative Poisson's ratios in few-layer orthorhombic arsenic: First-principles calculations. *Applied Physics Express* **2015**, *8*, 041801.

196. Sun, H.; Mukherjee, S.; Singh, C. V. Mechanical properties of monolayer penta-graphene and phagraphene: a first-principles study. *Physical Chemistry Chemical Physics* **2016**, *18*, 26736–26742.

197. Zhang, L.; Li, H.; Sun, C.; Ouyang, G. Strain engineering of the lattice vibration modes in monolayer black phosphorus. *Journal of Raman Spectroscopy* **2020**, *51*, 213–220.

198. Li, L. H.; Chen, Y. Atomically thin boron nitride: unique properties and applications. *Advanced Functional Materials* **2016**, *26*, 2594–2608.

199. Ren, L.; Liu, Q.; Xu, P.; Zhong, Z.; Yang, L.; Yuan, Z.; Xia, K. Noncollinearity-modulated Electronic Properties of Monolayer CrI_3. *Physical Review Applied* **2019**, *11*, 054042.

200. Liu, Z.-L.; Wu, X.; Shao, Y.; Qi, J.; Cao, Y.; Huang, L.; Liu, C.; Wang, J.-O.; Zheng, Q.; Zhu, Z.-L., et al. Epitaxially grown monolayer VSe_2: an air-stable magnetic two-dimensional material with low work function at edges. *Science bulletin* **2018**, *63*, 419–425.

201. Doğan, K. C.; Çetin, Z.; Yagmurcukardes, M. Anisotropic Structural, Vibrational, Electronic, Optical, and Elastic Properties of Single-layer Hafnium Pentatelluride: An Ab-initio Study. *Nanoscale* **2024**, *16*, 11262–11273.

202. Dogan, K. C.; Yagmurcukardes, M. Anisotropic Single-Layer Tilted α-Bi: Identification of Uniaxial Strain via Raman Spectrum. *The Journal of Physical Chemistry C* **2024**, *128*, 8490–8497.